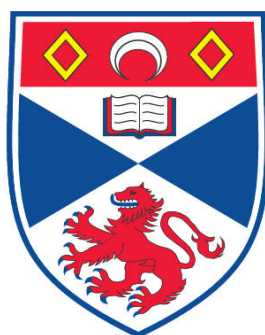


**EFFECTS OF SPIN-ORBIT COUPLING AND MANY-BODY
INTERACTIONS ON THE ELECTRONIC STRUCTURE OF Sr_2RuO_4**

Emil J Rozbicki

**A Thesis Submitted for the Degree of PhD
at the
University of St. Andrews**



2012

**Full metadata for this item is available in
Research@StAndrews:FullText
at:**

<http://research-repository.st-andrews.ac.uk/>

Please use this identifier to cite or link to this item:

<http://hdl.handle.net/10023/3217>

This item is protected by original copyright

University of St Andrews
School of Physics and Astronomy

Doctoral dissertation

**Effects of spin-orbit coupling and
many-body interactions on the
electronic structure of Sr_2RuO_4 .**

Emil J Rozbicki

Supervisor: Dr Felix Baumberger

St Andrews, 2011

1. Candidates declarations:

I, Emil J Rozbicki, hereby certify that this thesis, which is approximately words in length, has been written by me, that it is the record of work carried out by me and that it has not been submitted in any previous application for a higher degree.

I was admitted as a research student in September 2007 and as a candidate for the degree of Philosophy Doctor in June 2011; the higher study for which this is a record was carried out in the University of St Andrews between 2007 and 2011.

Date Signature of candidate

2. Supervisors declaration:

I hereby certify that the candidate has fulfilled the conditions of the Resolution and Regulations appropriate for the degree of in the University of St Andrews and that the candidate is qualified to submit this thesis in application for that degree.

Date Signature of supervisor

3. Permission for electronic publication:

In submitting this thesis to the University of St Andrews I understand that I am giving permission for it to be made available for use in accordance with the regulations of the University Library for the time being in force, subject to any copyright vested in the work not being affected thereby. I also understand that the title and the abstract will be published, and that a copy of the work may be made and supplied to any bona fide library or research worker, that my thesis will be electronically accessible for personal or research use unless exempt by award of an embargo as requested below, and that the library has the right to migrate my thesis into new electronic forms as required to ensure continued access to the thesis. I have obtained any third-party copyright permissions that may be required in order to allow such access and migration, or have requested the appropriate embargo below.

The following is an agreed request by candidate and supervisor regarding the electronic publication of this thesis:

Access to printed copy and electronic publication of thesis through
the University of St Andrews.

Date Signature of candidate Signature of supervisor

Contents

Abstract	7
1 Scientific Background	8
1.1 Introduction	8
1.1.1 Strongly Correlated Electron Systems	8
1.1.2 Fermi liquid theory	9
1.2 Properties of Sr_2RuO_4	11
1.2.1 Crystal Structure	12
1.2.2 Electronic Structure and surface reconstruction	12
2 Experimental Method	15
2.1 History of Photoemission	15
2.2 Kinematic description of the photoemission process	16
2.3 Theoretical Principles of Photoemission	19
2.3.1 Many body interactions in ARPES	24
2.3.2 Matrix elements, final state effects and finite resolution effects	33
2.4 Experimental Setup	35
2.4.1 Getter Pumps	37
2.4.2 Radiation Shield	39
3 Band structure of Sr_2RuO_4	41
3.1 Introduction	41
3.2 The Tight Binding Model	43
3.3 Density Functional Theory	44
3.4 Spin-Orbit Coupling in Solids	47
3.5 DFT Results	48
3.5.1 DFT + SOC	50
3.6 TB Results	51
3.6.1 Tight binding with SOC	56
3.6.2 Momentum dependent Zeeman splitting	57
4 Results and Discussion	61
4.1 Surface layer band structure	61
4.2 Momentum dependent mass renormalization	69
4.3 Orbital selective kink in the bulk bands	83

Abstract

The aim of the project is to investigate the effects of spin-orbit coupling and many-body interactions on the band structure of the single-layered strontium ruthenate Sr_2RuO_4 . This material belongs to the large family of strongly correlated electron systems in which electron-electron interaction plays a crucial role in determining the macroscopic properties. The experimental method used for this purpose is Angular Resolved Photoemission Spectroscopy (ARPES), which probes the single-particle spectral function and allows direct measurements of the quasi-particle band structure. The analysis is based on comparison of experimental data with electronic structure calculations. Typical methods for the band structure calculations including density functional theory (DFT) in the local density approximation (LDA) and tight-binding calculations (TB) are one-electron approximations and do not give insight into many-body interactions. However, comparing the measured band structures with calculated ones allows estimating the strength of the interactions in the considered system.

In Chapter 1 the earlier work on Sr_2RuO_4 , which is relevant to this project is presented. This chapter is an introduction to the data analysis and discussion of the results.

In Chapter 2 we describe the experimental setup, theoretical principles of the measurement and summarize important improvements made during this project.

In Chapter 3 we give a brief introduction into density functional theory and describe methods used within DFT to calculate the band structure. We further give a brief description of a tight binding model for Sr_2RuO_4 . The bulk of this chapter is devoted to present the effects of spin-orbit coupling on the band structure of Sr_2RuO_4 . In particular, we use a tight binding model to simulate the anisotropy of the Zeeman splitting found experimentally.

In Chapter 4 we present the ARPES results, their analysis and discussion. A particular focus is placed on the discussion of the surface layer Fermi surface topology and on the discovery of strong momentum dependence of the mass renormalization factors of the bulk β and γ bands.

Chapter 1

Scientific Background

1.1 Introduction

The main subject of this thesis are many-body interactions in Sr_2RuO_4 probed by Angular Resolved Photoemission Spectroscopy (ARPES). This single layered strontium ruthenate belongs to the family of Strongly Correlated Electron Systems (SCES) whose macroscopic properties are dominated by the consequences of strong interactions between electrons. The layered crystal structure and two-dimensional electronic properties make Sr_2RuO_4 ideally suited for ARPES experiments.

According to Fermi liquid theory many-body interactions renormalize the single electron bands making quasi-particles, electrons dressed by virtual excitations, heavier than bare electrons. ARPES directly measures the quasi-particle band structure - the binding energy of the many-electron states as a function of momentum. This makes ARPES a unique method to study many-body correlations as it not only provides information about the strength of the interactions but also about their momentum dependence.

1.1.1 Strongly Correlated Electron Systems

Strongly correlated electron systems continue to attract attention because of their unusual properties and extremely rich physics. Some of the intriguing states and properties of SCES are Mott insulators, heavy fermion states, colossal magnetoresistance and high temperature superconductivity. The discovery of all these effects came as a surprise and their microscopic origin is still a subject of intense debate.

Conventional band theory treats electrons as a gas of non-interacting particles moving in the fixed lattice of ions. This model works well for *sp*-metals such as Cu, Mg, Al, Au but breaks down for transition and rare earth elements with partially filled *d* and *f* shells. One of the most intriguing effects of electron correlations was first found in transition metal oxides. In 1937 J.H. de Boer and E.J.W. Verwey [1] reported that some of the materials predicted by the band theory to be metals are in fact insulators. As explained later by N. Mott [2] strong electron-electron interaction can induce a phase transition from the metallic to the insulating state by opening a gap at the Fermi level if the Coulomb repulsion becomes higher than the kinetic energy of the electrons.

In the 1970s a new class of metals was found called the heavy fermion systems. Measurements of the specific heat revealed that the quasi-particle effective mass in these

materials is more than hundred times larger than in normal metals. As in the case of Mott insulators the effect is driven by strong electron-electron interaction. Interactions between electrons can also influence the magnetic properties of a material. A particularly distinctive example is colossal magnetoresistance. Some manganites change their resistivity by several orders of magnitude in a relatively weak magnetic fields because they effectively undergo a field induced metal-insulator transition. Possibly the most striking and exciting discovery related to strong correlations was high temperature superconductivity in transition metal oxides. Research stimulated by this discovery led to the synthesis of a large number of new materials which revealed novel exotic phases and charge, orbital or spin ordering driven by strong correlations.

At present there is no microscopic theory that could account for all these effects. As the field of SCES is now very broad, systematic work to characterize the properties and details of many-body interactions for these materials is necessary in order to find a common denominator and lay down a basis for new theoretical treatments.

1.1.2 Fermi liquid theory

In the Sommerfeld theory of metals where interactions between electrons are neglected the ground state resulting from Pauli's principle is a filled Fermi sea of occupied states in momentum space up to limiting wave vector $k_F = (3\pi N)^{\frac{1}{3}}$ (N - density of particles in the Fermi gas). The highest occupied state with energy $\epsilon_F = \frac{\hbar^2 k_F^2}{2m_e}$ and momentum $p_F = \hbar k_F$ is called the Fermi level. ϵ_F and p_F define the Fermi surface (FS) that separates occupied from unoccupied states. Excited states of the Fermi sea are generated by moving up electrons from states just below the FS to just above it. All excited states are uniquely labelled by the momentum quantum numbers of empty (hole) states below the FS and occupied (electron) states above it. If the interactions between the electrons are now turned on the momentum does not have to be a good quantum number anymore, rendering a description of such a system more involved. In the 1950s Landau has proposed a way around this problem. He postulated that there exists a continuous and one-to-one correspondence between the eigenvalues of the non-interacting and the interacting systems. This idea of adiabatic continuity plays a crucial role in Fermi liquid theory because it permits labeling the low energy states of the interacting system by the same quantum numbers as those of the non-interacting system as the interactions are turned on. The interactions do not change the labeling of the states, they do, however, change their energy and wavefunctions, so the particles of the interacting systems are no longer electrons but quasi-particles. The total energy of the interacting system can then be written as:

$$E = \sum_{\mathbf{k}} \frac{\hbar \mathbf{k}_F}{m^*} (\hbar \mathbf{k} - \hbar \mathbf{k}_F) \delta n_{\mathbf{k}} + \frac{1}{2} \sum_{\mathbf{k}\mathbf{k}'} f_{\mathbf{k},\mathbf{k}'} \delta n_{\mathbf{k}} \delta n_{\mathbf{k}'}, \quad (1.1)$$

where the first term represents the energy of a single quasi-particle and the second the interaction between the quasi-particles. The above equation introduces two new quantities, m^* called the effective mass and $f_{\mathbf{k},\mathbf{k}'}$, Landau's f -function related to the scattering amplitude of two quasi-particles. The difference between m and m^* comes from the interaction; electrons strongly repel each other, so as the quasi-particle moves, it creates a back-flow in the Fermi sea and this effect modifies its effective mass. Using equation 1.1,

one can evaluate the equilibrium properties of the interacting system such as specific heat c_v , magnetic susceptibility χ and resistivity ρ_{el-el} [3, 4]:

$$c_v = \frac{1}{3} \frac{m^* p_F}{\hbar^3} k_B^2 T, \quad (1.2)$$

$$\chi = \frac{m^* p_F}{\pi^2 \hbar} \frac{1}{1 + F_0^a} \mu_B^2, \quad (1.3)$$

$$\rho_{el-el} = A_0 \frac{m^{*2} k_B^2}{n \hbar^3 e^2 k_F^2} T^2. \quad (1.4)$$

The specific heat and magnetic susceptibility are very similar to their non-interacting analogs. The main difference is that they depend on the effective quasi-particle mass m^* instead of the bare electron mass. The susceptibility has an additional term F_0^a which is related to the Landau f -function and is known as Landau parameter. The effective mass is a parameter in Landau's theory and as such has to be determined experimentally by specific heat, de Hass van Alphen or ARPES measurements. The resistivity ρ_{el-el} is proportional to T^2 in Fermi liquid theory (A_0 is a dimensionless parameter and n is the electron density).

Interactions also cause a finite lifetime of the quasi-particles given by:

$$\frac{1}{\tau} \sim \frac{\pi}{\hbar} |V|^2 g_F^3 \epsilon^2 \quad (1.5)$$

where $|V|^2$ is the scattering amplitude of quasi-particles, g_F is the density of states and ϵ is the quasi-particle energy. When ϵ is small (close to ϵ_F) quasi-particles are well defined - their lifetime is very long because the decay rate is much smaller than their energy. This no longer holds for high energies, but as long as we are concerned only with low temperatures and excitations close to the Fermi surface the quasi-particle picture is valid.

Following Pauli's principle the ground state of the non-interacting system consists of occupied states below \mathbf{k}_F and empty states above \mathbf{k}_F , so the probability of finding an electron with $\mathbf{k} < \mathbf{k}_F$ is equal 1 and with $\mathbf{k} > \mathbf{k}_F$ is equal 0. Thus the electron distribution function of non-interacting particles is a step function with a discontinuity at $\mathbf{k} = \mathbf{k}_F$ (see figure 1.1 (a)).

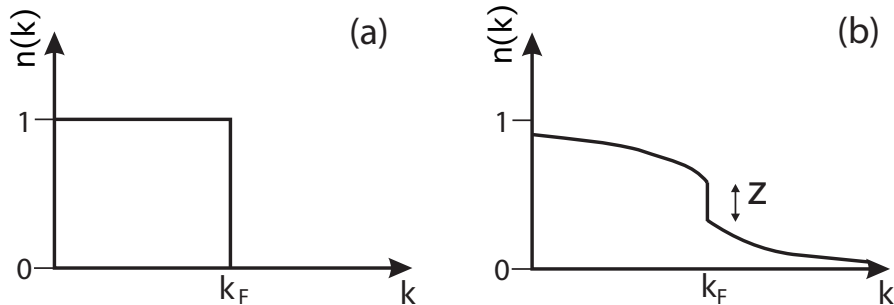


Figure 1.1: Probability that a state of a given crystal momentum \mathbf{k} is occupied for (a) a non-interacting system and (b) a Fermi liquid, at $T=0$.

The adiabatic continuity guarantees that the quasi-particle wavefunction will remain a fraction Z of the original non-interacting excited state wavefunction [4]:

$$|\psi_{qp}(\mathbf{k})\rangle = \sqrt{Z}|\phi_{el}\rangle + \text{particle} - \text{hole excitations}, \quad (1.6)$$

where Z is the overlap of an electron and q quasi-particle wavefunction and thus measures the probability of finding an electron in the quasi-particle eigenstate with momentum \mathbf{k} . Because the quasi-particles in the interacting system contain contribution from many electrons their energy and momentum will be spread out. This translates into a step of reduced, though finite height $Z < 1$ at \mathbf{k}_F and some spectral weight for $\mathbf{k} > \mathbf{k}_F$, i.e. outside the non-interacting Fermi surface (see figure 1.1 (b)).

1.2 Properties of Sr_2RuO_4

Sr_2RuO_4 is the single layered member of the Ruddlesden-Popper series $\text{Sr}_{n+1}\text{Ru}_n\text{O}_{3n+1}$ (where n is the number of layers). The entire series exhibits intriguing properties generally attributed to many-body interactions. SrRuO_3 ($n = \infty$) is a ferromagnetic metal with $T_{Curie} = 160$ K, $\text{Sr}_4\text{Ru}_3\text{O}_{10}$ is a ferromagnet with $T_{Curie} = 105$ K that shows a metamagnetic transition induced by magnetic field in the ab plane below 50 K. Double layered $\text{Sr}_3\text{Ru}_2\text{O}_7$ is a paramagnetic Fermi liquid and shows a metamagnetic transition with a quantum critical endpoint [5, 6].

From transport measurements it is clear that Sr_2RuO_4 ($n=1$) is a paramagnetic Fermi liquid [7–10]. Figure 1.2 shows resistivity and specific heat as a function of temperature [9, 10]. The resistivity is highly anisotropic with a low temperature ratio $\frac{\rho_c}{\rho_{ab}}$ varying

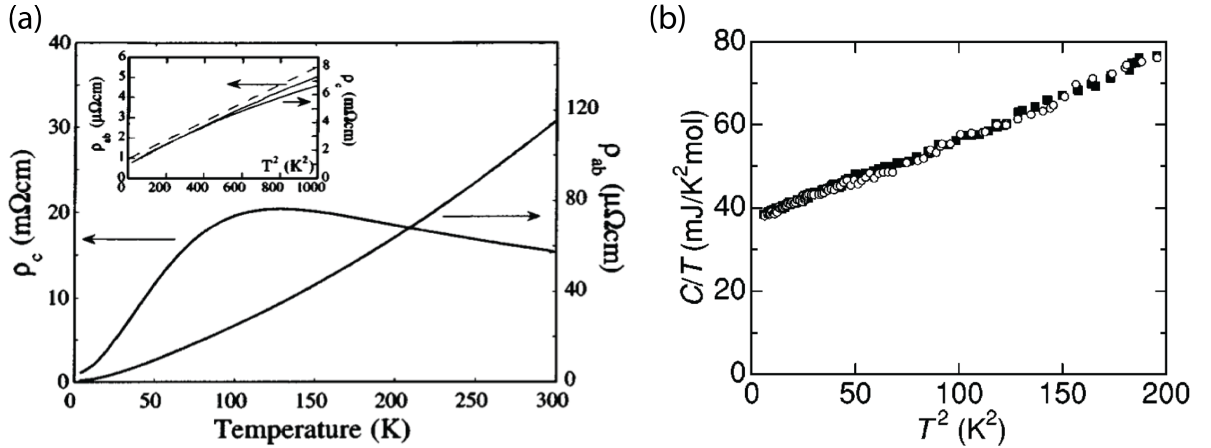


Figure 1.2: Transport properties of Sr_2RuO_4 . (a) anisotropic resistivity as a function of temperature reproduced from [9], (b) specific heat divided by temperature, filled squares in zero field open circles in 14T, reproduced from [10].

between 400 and 4000 depending on sample quality. Below 20 K the in-plane (ρ_{ab}) and interlayer resistivity (ρ_c) have a T^2 dependence as expected within Fermi liquid theory. Figure 1.2(b) shows the specific heat measured by Mackenzie et al. [10]. As reported by these authors the total specific heat can be modelled by $\gamma_{el}T + \beta_{ph}T^3$ with $\gamma_{el} =$

38 mJ/molK². The electronic contribution is constant below 15 K, consistent with eq. 1.2. At 1.5 K Sr₂RuO₄ becomes superconducting with an unusual *p*-wave symmetry of the order parameter and spin-triplet pairing [11].

1.2.1 Crystal Structure

Sr₂RuO₄ crystallizes in the K₂NiF₄ structure with *I4/mmm* body-centered tetragonal space group symmetry and is isostructural with the high temperature superconductor LaSr_{2-x}Cu_xO₄. In contrast to many to high temperature superconductors, Sr₂RuO₄ does not show any lattice distortion such as a rotation or a tilting of RuO₆ octahedra or a structural phase transitions down to the lowest measurable temperatures.

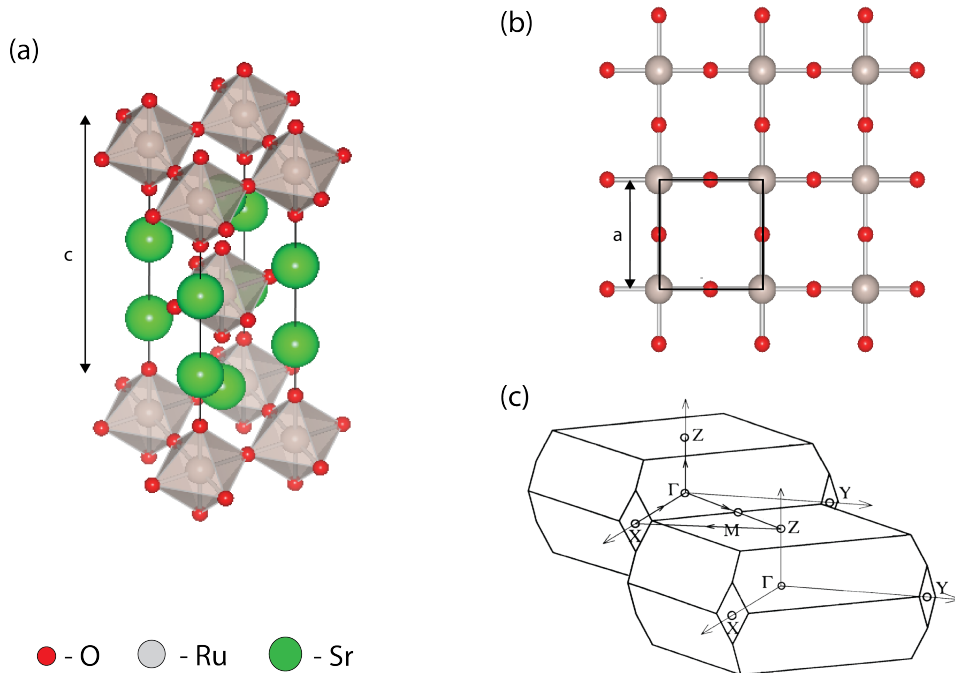


Figure 1.3: Crystal structure of Sr₂RuO₄. (a) conventional unit cell, (b) square lattice of the RuO₂ plane, (c) 3D Brillouin zone for the *I4/mmm* space group.

The lattice parameters measured by low temperature powder neutron diffraction are $a = 3.86 \text{ \AA}$, $c = 12.72 \text{ \AA}$ [12]. Figure 1.3 shows the crystal structure and 3D Brillouin zone of Sr₂RuO₄. The crystal structure is composed of alternating RuO₂ and SrO₂ layers.

Strontium ruthenate crystals can be grown using the floating zone technique. Crystals used in this project were produced in the group of A. Mackenzie at the University of St Andrews independently by A. Gibbs and D. Slobinsky. The purity of the crystals can be characterized by the critical temperature of the superconducting state [13] which in this case was 1.52K, the highest achieved so far, indicating an outstanding quality of samples.

1.2.2 Electronic Structure and surface reconstruction

This section briefly summarizes the historical evolution of the understanding of the electronic structure of Sr₂RuO₄. A detailed theoretical study of the band structure and our

new ARPES data will be presented in Chapter 3 and Chapter 4, respectively.

The discovery of superconductivity in 1994 has moved Sr_2RuO_4 into the spot-light as it is the only superconducting layered perovskite without copper. Shortly after Maeno *et al.* [11] have reported a superconducting transition around 1 K Oguchi [14] performed band structure calculations within density functional theory. He found three highly two-dimensional bands at the Fermi surface. The α sheet centered at the X-point is hole-like, while the β and γ sheets are electron-like. Because of the strongly two-dimensional character of the bands, it is common to use a simplified two-dimensional Brillouin zone as shown in figure 1.4 (a). The band structure calculations were later confirmed in de Hass van Alphen (dHvA) measurements performed by Mackenzie *et al.* [15, 16]. These experiments further revealed a strong quasi-particle mass enhancement for all three bands as summarized in Table 1.1.

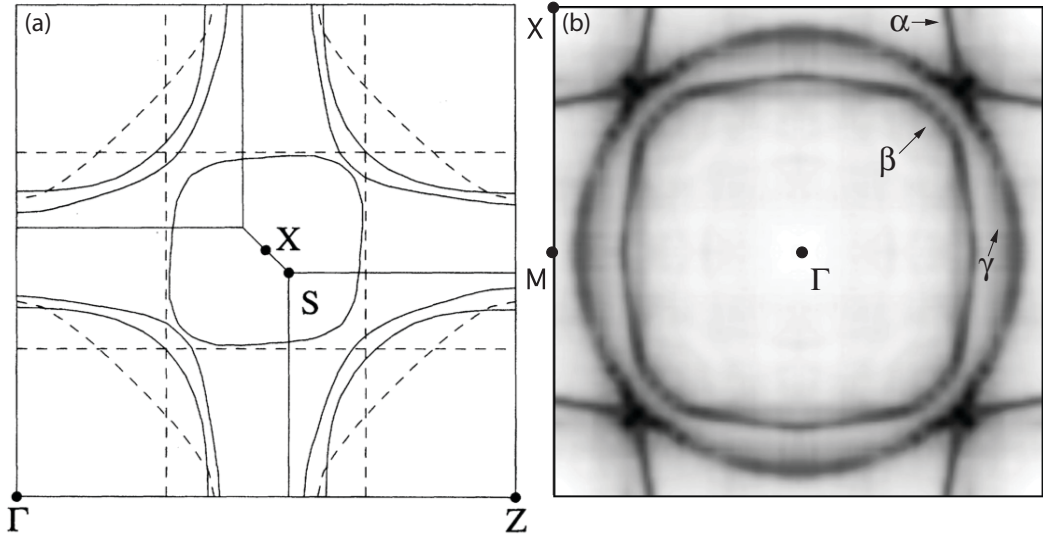


Figure 1.4: Fermi surface of Sr_2RuO_4 from: (a) LDA calculations by Oguchi [14], (b) ARPES measurements by Damascelli *et al.* [17].

At the time of the discovery of superconductivity in Sr_2RuO_4 ARPES was extensively used to study many-body effects on the band structure of the high temperature superconductors. Since this time there is an ongoing controversy as to whether ARPES can probe bulk properties given that photoelectrons escape only from the first few atomic layers of a material. Sr_2RuO_4 provide a unique opportunity to compare ARPES from correlated electron systems with bulk probes. Contrary to LDA and dHvA studies early photoemission work by Lu [18] and Yokoya [19] predicted that the γ band is holelike. This inconsistency could only be overcome with an analysis of the surface structure using scanning-tunneling microscopy (STM) and low energy electron diffraction (LEED) by Matzdorf *et al.* [21, 22] and by new ARPES data from Damascelli *et al.* [17]. The study of Matzdorf *et al.* showed that the surface layer forms a $(\sqrt{2} \times \sqrt{2})R45^\circ$ reconstruction upon cleaving because the octahedra in the top-layer rotate by 6–11°. This is illustrated in figure 1.5 together with the in-plane unit cells for the bulk and surface layer. As the crystal structure of the surface differs from the bulk so does the electronic structure. ARPES measurements thus contain information about both electronic systems and early work could not resolve the

Fermi Surface Sheet Character	α holelike	β electronlike	γ electronlike
k_F (\AA^{-1})	0.304	0.622	0.753
$m^*(m_e)$	3.3	7.0	16.0
m^*/m_{band}	3.0	3.5	5.5
ν_F (ms^{-1})	1×10^5	1×10^5	5.5×10^4

Table 1.1: Summary of quasi-particle Fermi surface parameters of Sr_2RuO_4 from dHvA measurements [20].

individual contributions. Damascelli *et al.* [17] showed that if the sample is cleaved at ~ 160 K the intensity of surface layer bands is substantially diminished allowing for a clearer observation of the bulk band structure. The Fermi surface from this work with all the bulk bands clearly resolved and in agreement with dHvA and LDA studies is shown in figure 1.4 (b).

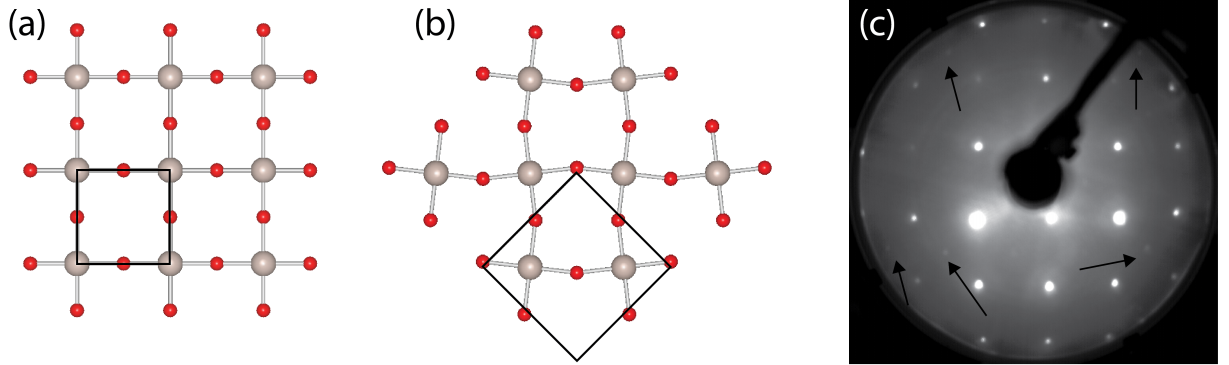


Figure 1.5: Surface reconstruction in Sr_2RuO_4 . (a) square lattice of the bulk layers, (b) rotation of the octahedra double the unit cell at the surface, (c) LEED taken at 300eV, arrows indicate additional spots coming from the rotation of the surface octahedra.

Chapter 2

Experimental Method

2.1 History of Photoemission

Photoemission spectroscopy is based on the photoelectric effect discovered by Hertz in 1887 [23]. In the 1880s Hertz was working on the generation and properties of electrical oscillations. His experiments proved the existence of electromagnetic waves, predicted by Maxwell, but also revealed a new phenomenon, the photoelectric effect. Hertz noticed that metal contacts exhibit enhanced ability to spark when exposed to light. Shortly after Hertz published his results, Hallwachs observed that negatively charged plates are losing their charge when exposed to UV light while positively charged ones do not [24]. The interpretation of these findings was far from trivial as the electron was only discovered a decade after Hallwachs' experiments. In 1899 J. J. Thomson [25] reported the discovery of new tiny sub-particles with negative charge, later called electrons. Following work of Hertz and Hallwachs in 1902 Lenard [26] performed a series of breakthrough experiments. He measured the energy distribution of photoelectrons by applying a variable retarding potential. From the results he concluded that the number of emitted electrons depends on the intensity of the light and, surprisingly, that their velocity depends only on the light frequency. On the basis of current knowledge at the time Lenard could not explain the relationship between the maximum kinetic energy of electrons and the wavelength of the incident radiation.

In 1905 Einstein [27] proposed a phenomenological explanation of this effect. Based on Lenard's results and formalisms derived by Planck, Wien and Boltzmann (entropy of radiation of certain frequency) he proposed that light has a particle-like nature. Its energy is distributed discontinuously in space and electrons can absorb this quanta of energy resulting in photoemission. Einstein formulated his prediction in the now famous equation for the maximum kinetic energy of the photoemitted electron

$$E_{kin} = \frac{R}{N}\beta\nu - P \quad (2.1)$$

where $\beta = \frac{h}{k}$, $k = \frac{R}{N}$ is the Boltzmann constant and N is Avogadro's number, P is a potential step or some work done near the surface (today called the workfunction Φ).

The experimental confirmation of Einstein's formula came from Millikan in 1916 [28]. Millikan built a state of the art vacuum chamber in which he could prepare clean metal surfaces by cutting off layers from a large piece of material. He used a retarding-potential

Faraday-cup technique to measure a photoelectric current as a function of wavelengths. For each frequency he observed a high-energy cutoff and, most importantly, from the fit to the experimental data got a linear dependence (figure 2.1) confirming equation 2.1.

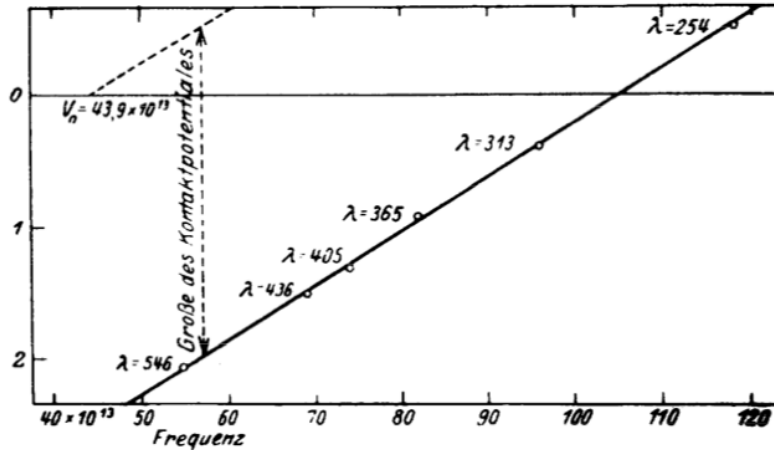


Figure 2.1: Determination of Planck's constant h by Millikan from the slope of electron energy versus light frequency and Einstein's equation. Figure reproduced from [29].

Later theoretical advances came from G. Beck [30], G. Wentzel [31] and R. Oppenheimer [32] who investigated the photoeffect and the angular distribution of electrons using formalisms from quantum mechanics.

The first use of photoemission as an analytical tool, although accidentally, was by Innes in 1907 [33]. The author investigated Pb, Zn, Ag, Pt and Au irradiated by an x-ray source. Photoelectrons of different velocity were dispersed by a magnetic field and particles were detected by photographic plates. The author emphasized the fact that the electron velocity is independent from the intensity of x-rays. However, he ascribed emitted electrons to the disintegration of atoms rather than to photoemission because of the large kinetic energy of the electrons. The first intentional x-ray photoemission study was performed by de Broglie in 1921 [34], who verified Einstein's relation at high photon energies.

After 1950 there were two great instrumental improvements made that helped to establish photoemission as an analytical tool for the study of atoms, molecules and solids. In the early 1950s Siegbahn and coworkers built a high resolution XPS spectrometer [35, 36] and collected photoemission data for many of solids and gases [37, 38]. In 1960s D. Turner and coworkers developed the first differentially pumped helium discharge lamp, which helped to improve the resolution of UPS experiments down to ~ 20 meV [39–41].

2.2 Kinematic description of the photoemission process

Angle-resolved photoemission spectroscopy (ARPES) provides direct information about the electronic band structure of solids. The main application of ARPES in recent years

has been the study of complex systems whose macroscopic properties are a consequence of strong correlations between electrons.

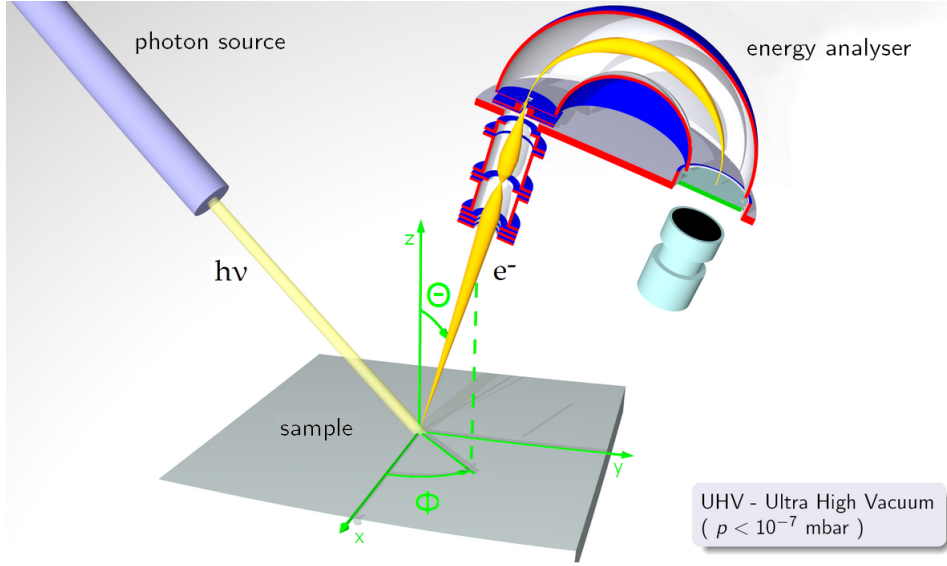


Figure 2.2: Principle of the photoemission process. A sample exposed to a radiation source (UV, x-ray) emits electrons. The emitted electrons are collected, energy resolved and counted by an energy analyser. Figure reproduced from [42].

Photoemission spectroscopy is based on the photoelectric effect, which was observed by Hertz in 1887 [23] and explained later by Einstein [27]. In the photoelectric effect an electron can be liberated from the solid by the incident photon if its energy exceeds the binding energy of the electron (E_B) and the potential barrier between sample surface and vacuum, the so called work function (Φ). Because the energy is conserved during the photoemission process one can obtain the electron's binding energy by measuring its kinetic energy:

$$E_{kin} = h\nu - \Phi - E_B, \quad (2.2)$$

where ν is frequency of the absorbed photon. Figure 2.3 presents the relation between the measured spectrum and the electron energy levels in the solid.

In order for the electron to be emitted into vacuum, the momentum conservation law must be also obeyed

$$\mathbf{k}_f - \mathbf{k}_i = \mathbf{k}_{h\nu} \quad (2.3)$$

where \mathbf{k}_f is the momentum of the photoelectron in vacuum, \mathbf{k}_i is the initial momentum and $\mathbf{k}_{h\nu}$ is the momentum of absorbed photon. For low photon energies its momentum can be neglected as it is much smaller than the Brillouin zone size of typical solids. This means that the optical transition between the initial and the final bulk states can be described by a vertical transition ($\mathbf{k}_f - \mathbf{k}_i = 0$) or by transition between momentum-space points connected by a reciprocal lattice vector \mathbf{G} ($\mathbf{k}_f - \mathbf{k}_i = \mathbf{G}$). Figure 2.4 illustrates the kinematics of the photoemission process.

Because of the broken translational invariance perpendicular to the surface only the

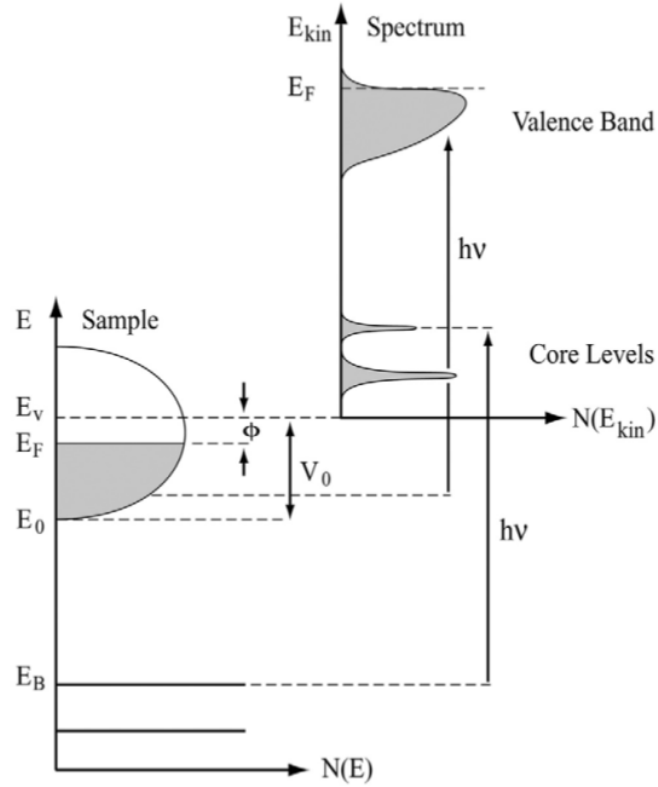


Figure 2.3: Relation between the electron energy levels in the solid and the measured spectrum in the single-particle picture. Electrons with binding energy E_B can be excited into vacuum E_v by photons with energy higher than $E_B + \Phi$. V_0 is called the inner potential and it measures the energy between bottom of the valence band and the vacuum level E_v , as explained in text, it can be used to determine the normal component of the momentum wave vector. Figure reproduced from [43].

component of the wave vector parallel to surface is conserved:

$$k_{i,\parallel} = k_{f,\parallel} = k_{\parallel} = \frac{1}{\hbar} \sqrt{2m_e E_{kin}} \sin \theta, \quad (2.4)$$

where θ is the emission angle. Determination of k_{\perp} which is not conserved requires additional assumptions about the photoelectron final state. The simplest models use either band-like or free-electron final states, then, by using equations 2.2 and 2.4 the component of the wave vector perpendicular to the surface is given by

$$k_{\perp} = \frac{1}{\hbar} \sqrt{2m_e (E_{kin} \cos^2 \theta + V_0)}, \quad (2.5)$$

where V_0 is the inner potential of the crystal, which can be determined experimentally.

Equations 2.2, 2.4 and 2.5 relate the measured kinetic energy as a function of emission angle of the photoelectron $E_{kin}(\theta)$ to the binding energy as function of momentum of the electron in the solid $E(\mathbf{k})$ – the band structure.

The description of the photoemission as a single coherent quantum mechanical process is rather involved and beyond the scope of this thesis. Instead we will focus on a simplified

description within the so-called *three-step model* in which the process is decomposed to three independent events: photo-excitation of the electron, travel of the photoelectron to the surface and escape into the vacuum.

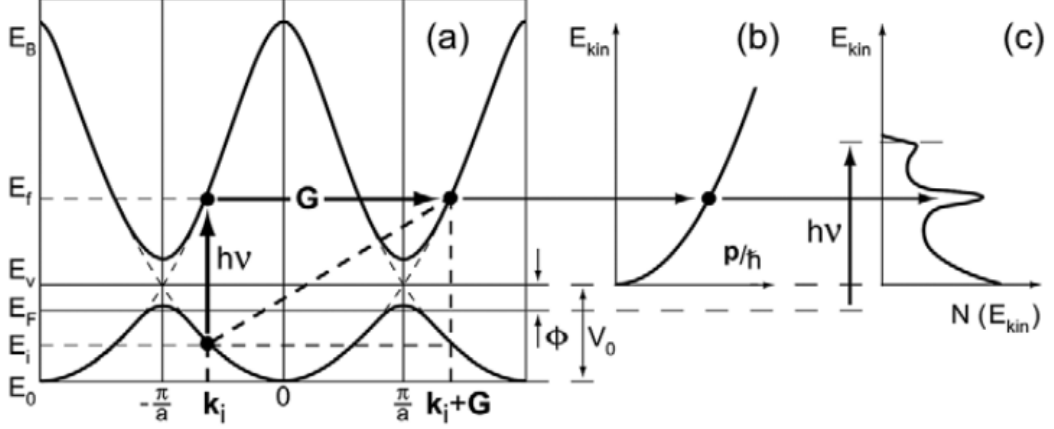


Figure 2.4: Photoemission within the three-step model: (a) optical transition in the solid, (b) free–electron final state in vacuum, (c) probed photoelectron spectrum (from [44]).

2.3 Theoretical Principles of Photoemission

From a theoretical point of view, the photoemission process is an optical transition between initial and final states described by many-body wave functions. The initial state is an N -electron eigenstates and the final state is an $(N - 1)$ -electron system plus the photoelectron. Fermi's Golden Rule is a convenient and starting point to describe the photoemission process

$$w_{if} = \frac{2\pi}{\hbar} |\langle \Psi_f | H' | \Psi_i \rangle|^2 \rho_f, \quad (2.6)$$

where w_{if} is the probability of a transition between initial and final states of the system described by the wave functions $|\Psi_{i/f}\rangle$, H' is the perturbation that caused the transition and ρ_f is the density of final states. The above formula can be rewritten in the following way to calculate the probability of photoexcitation of the N -electron groundstate $|\Psi_i\rangle$ to one of the possible excited final states $|\Psi_f\rangle$ consisting of a photoelectron with momentum \mathbf{k} and energy $E_{kin} = \frac{\hbar k^2}{2m_e}$ and the remaining $(N - 1)$ -electron system

$$w_{if} = \frac{2\pi}{\hbar} |\langle \Psi_f | H_{PE} | \Psi_i \rangle|^2 \delta(\epsilon_f - \epsilon_i - h\nu), \quad (2.7)$$

where $\epsilon_{i/f}$ denotes the energy of the initial and final states and H_{PE} describes the interaction with the photon. The latter can be obtained by the transformation of the momentum operator to include the electron's interaction with an electromagnetic field $\mathbf{p} \rightarrow \mathbf{p} - \frac{e}{c}\mathbf{A}$.

Starting from an unperturbed Hamiltonian $H_0 = \frac{p^2}{2m_e} + eV(\mathbf{r})$ one gets

$$\begin{aligned}
H &= \frac{1}{2m_e} \left(\mathbf{p} - \frac{e}{c} \mathbf{A} \right)^2 + eV(\mathbf{r}) \\
&= \frac{p^2}{2m_e} - \frac{e}{2m_e c} (\mathbf{A} \cdot \mathbf{p} + \mathbf{p} \cdot \mathbf{A}) + \frac{e^2}{2m_e c^2} A^2 + eV(\mathbf{r}) \\
&= H_0 + H_{PE},
\end{aligned} \tag{2.8}$$

where

$$H_{PE} = -\frac{e}{2m_e c} (\mathbf{A} \cdot \mathbf{p} + \mathbf{p} \cdot \mathbf{A}) + \frac{e^2}{2m_e c^2} A^2. \tag{2.9}$$

Here, \mathbf{p} is the momentum operator and \mathbf{A} is the electromagnetic vector potential. By choosing an appropriate gauge, the scalar potential Φ can be set to zero. The quadratic term can be omitted as it is relevant only for very high intensities of the exciting radiation. Using the commutation relation $[\mathbf{p}, \mathbf{A}] = -i\hbar \nabla \cdot \mathbf{A}$ and the dipole approximation $\nabla \cdot \mathbf{A} = 0$ one gets

$$H_{PE} = -\frac{e}{m_e c} \mathbf{A} \cdot \mathbf{p}. \tag{2.10}$$

The dipole approximation assumes that \mathbf{A} does not change over atomic distances. This is true for the bulk. However, at the surface the electromagnetic field may vary over short length scales. This can result in asymmetric lineshapes for direct transitions. However, the effect is generally small and will be neglected here.

In spite of these simplifications the problem is still far from trivial as photoemission is a single coherent process of absorption, electron removal and detection. The Hamiltonian describing photoemission in a *one-step model* would have to contain bulk, surface and vacuum states. Due to the complexity of such a description the photoemission event is usually split in to three independent steps. In the so-called *three-step model*: i) photo-excitation of the electron, ii) travel of the photoelectron to the surface, and iii) escape into vacuum. Within this model the measured intensity is a product of the optical transition probability (photo-excitation), the scattering probability during transport to the surface and the transmission probability through the surface potential barrier. This model was introduced by Berglund and Spicer in 1964 [45] and even-though it is purely phenomenological gives deep insight in the photoemission process.

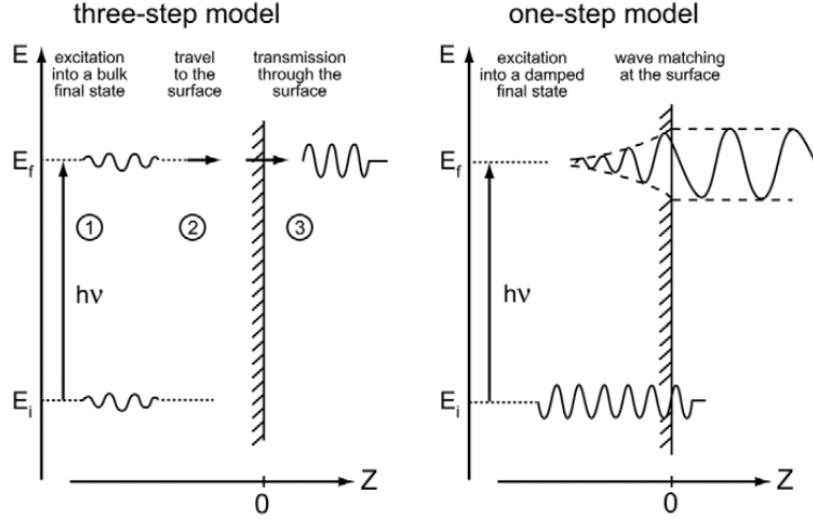


Figure 2.5: One-step model vs three-step model. The three-step model consists of (1) photoexcitation of an electron, (2) travel to the surface and (3) transmission through the surface into vacuum. In the one-step model an initial state electron is excited into a wave that propagates freely in vacuum but decays away from the surface into the solid (from [46]).

Step one - Photoionization

This process contains all the information about the electronic structure of the solid and it is described within the so called *sudden approximation*, where the interaction between the photoelectron and the remaining $(N - 1)$ -particle system is neglected. This allows to write the final state wave function as a product of the wave functions of the photoelectron $|\phi_{\mathbf{k},f}\rangle$ and an excited state s of the $(N - 1)$ -electron system $|\Psi_s^{N-1}\rangle$

$$|\Psi_f\rangle = a|\phi_{\mathbf{k},f}\Psi_s^{N-1}\rangle, \quad (2.11)$$

where a is an antisymmetric operator. The total transition probability is simply a sum over all excited states s . The *sudden approximation* holds only for electrons with high kinetic energy for which the escape time is much shorter than the system response time. In the opposite *adiabatic limit* of slow electrons, the wave functions cannot be factorized and one has to include the screening between photoelectron and photohole. Using factorized forms for the wave functions the matrix elements between initial and final state can be written as

$$\langle\Psi_f|H_{PE}|\Phi_i\rangle = \langle\phi_{\mathbf{k},f}|H_{PE}|\phi_{\mathbf{k},i}\rangle\langle\Psi_s^{N-1}|c_{\mathbf{k}}|\Psi_i^N\rangle \quad (2.12)$$

where $c_{\mathbf{k}}$ is the annihilation operator for an electron with momentum \mathbf{k} . The total photoemission intensity measured as a function of the kinetic energy E_{kin} at a momentum \mathbf{k} is equal to

$$I(\mathbf{k}, E_{kin}) = \frac{2\pi}{\hbar} \sum_{fi} |M_{\mathbf{k},f,i}|^2 \sum_s |c_{s,i}|^2 \delta(E_{kin} + \epsilon_s^{N-1} - \epsilon_i^N - h\nu), \quad (2.13)$$

where ϵ_s^{N-1} is the energy of the eigenstate s of the $(N - 1)$ -electron system, $|M_{\mathbf{k},f,i}|^2 = |\langle \phi_{\mathbf{k},f} | H_{PE} | \phi_{\mathbf{k},i} \rangle|^2$ is the photoemission matrix element describing the transition probability of a single electron from state $|\phi_{\mathbf{k},i}\rangle$ to the final state $|\phi_{\mathbf{k},f}\rangle$ and $|c_{s,i}|^2 = |\langle \Psi_s^{N-1} | c_k | \Psi_i^N \rangle|^2$ is a probability that the removal of the electron from state i will leave the $(N - 1)$ -electron system in the excited state s .

Step two - Transport

During the transport to the surface electrons undergo elastic and inelastic scattering. Elastic scattering is important only at high electron energies and the high incident photon energies. The inelastic processes give rise to a continuous background in the measured spectra which is usually subtracted or simply ignored. As a result of inelastic scattering electrons lose kinetic energy by exciting secondary electrons, plasmons and phonons. This limits the escape depth of photoelectrons, described by λ , the so-called inelastic-mean-free path (IMFP). The number of emitted electrons depends on the distance d they have to travel in the solid to reach the surface. The intensity of the emitted electrons is given by

$$I(d) = I_0 e^{-\frac{d}{\lambda}}, \quad (2.14)$$

where I_0 is proportional to the number of the excited electrons. The energy dependence of λ is described by the so-called "universal curve".

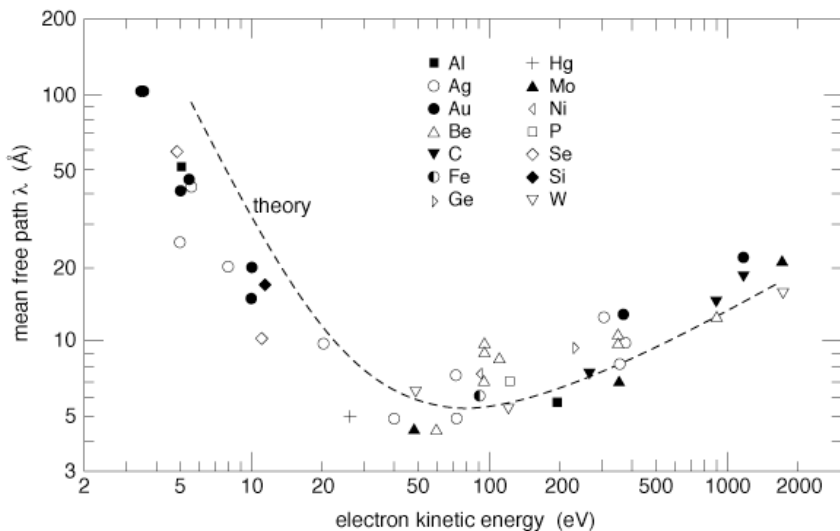


Figure 2.6: The inelastic electron mean-free path in solids - "universal curve". Figure reproduced from [46].

In a typical ARPES experiment, photoexcited electrons have kinetic energies in the range of 20-100 eV, so their mean free path is approximately 5 Å. This means that the technique is extremely surface sensitive and that the topmost layer has a large contribution to the total intensity. Therefore samples for ARPES measurements need atomically flat, clean and well-ordered surfaces.

Step three - Escape

The only electrons that can escape from the sample are those with a component of the kinetic energy normal to the surface sufficient to overcome the surface potential barrier. Inside the crystal electrons travel in the inner potential of depth $V_0 = E_v - E_0$ (see figure 2.3), where E_v is the work function, and E_0 is the bottom of the valence band. In order to escape the electron must fulfill the condition:

$$\frac{\hbar^2}{2m_e} k_{\perp}^2 \geq V_0. \quad (2.15)$$

where k_{\perp} is the component of the wave vector normal to the surface.

During the escape of electrons to the vacuum, only the parallel component of the wave vector is conserved modulo a reciprocal lattice vector (due to the periodicity of the lattice potential parallel to the surface). Therefore, one can connect the measured k_{\parallel}^{vac} with k_{\parallel}^{cryst}

$$k_{\parallel}^{vac} = k_{\parallel}^{cryst} - G_{\parallel}, \quad (2.16)$$

where G_{\parallel} is a reciprocal lattice vector. Figure 2.7 shows the relation between vacuum

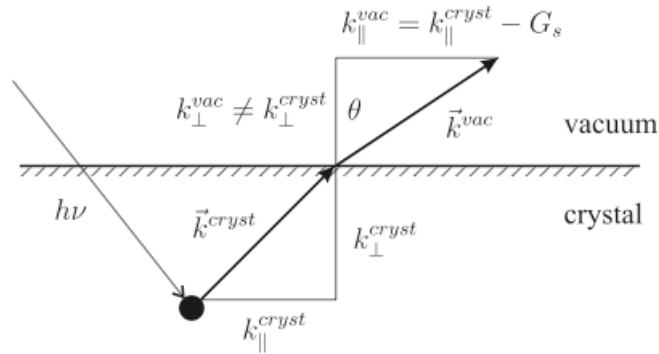


Figure 2.7: Momentum relation at the solid-vacuum interface in angle-resolved photoemission. In the transmission across the crystal-vacuum interface only the parallel component of momentum is conserved, modulo a reciprocal surface lattice vector, but the normal component is altered by the surface potential.

and solid momenta. One can express k_{\parallel}^{cryst} via the kinetic energy and the emission angle θ with respect to the surface normal by

$$k_{\parallel}^{cryst} = \sqrt{\frac{2m_e}{\hbar^2} E_{kin}} \sin \theta. \quad (2.17)$$

The Bloch eigenstates inside the sample have to match the free-electron plane waves in vacuum in order for the transmission to take place. The wavefunction of the final state within the solid with energy $E_f(\mathbf{k})$ is given by

$$\phi_f(\mathbf{k}) = \sum_{\mathbf{G}} u_f(\mathbf{k}, \mathbf{G}) e^{i(\mathbf{k}+\mathbf{G})\cdot\mathbf{r}} \quad (2.18)$$

Photoelectrons can escape from the crystal in a number of possible directions given by eq. 2.17. All planewave components of the Bloch state with the same value of $k_{\parallel} + G_{\parallel}$ will leave the crystal in the same direction giving rise to the coherent beam. The total transmission factor $|T(E_f, \mathbf{k}_{\parallel})|^2$ for a given value of $k_{\parallel} + G_{\parallel}$ at a particular final state E_f is given by

$$|T(E_f, \mathbf{k}_{\parallel})|^2 = |t(E_f, \mathbf{k}_{\parallel} + \mathbf{G}_{\parallel})|^2 \left| \sum_{(k+G)_{\perp} > 0} u_f(\mathbf{G}, \mathbf{k}) \right|^2 \quad (2.19)$$

where the sum goes over all components propagating towards surface. The reduced transmission factor $|t(E_f, \mathbf{k}_{\parallel} + \mathbf{G}_{\parallel})|^2$ which neglects surface scattering is given by

$$|t(E_f, \mathbf{k}_{\parallel} + \mathbf{G}_{\parallel})|^2 = \begin{cases} 1 & \text{if } E_{kin} > \frac{\hbar^2}{2m_e}(\mathbf{k}_{\parallel} + \mathbf{G}_{\parallel})^2 \\ 0 & \text{if } E_{kin} \leq \frac{\hbar^2}{2m_e}(\mathbf{k}_{\parallel} + \mathbf{G}_{\parallel})^2 \end{cases} \quad (2.20)$$

where E_{kin} is electron kinetic energy in the vacuum.

As it was already mentioned, the wavevector component perpendicular to the surface is not conserved during the escape. One way around this problem is to study two dimensional systems where k_{\perp} does not matter. If, however, one is interested in solids with three dimensional electronic structure there is an experimental approach that allows one to estimate k_{\perp} . By measuring photoelectrons emitted along the surface normal as a function of photon energy one can deduct V_0 in equation 2.5 from the periodicity of the measured $E(k_{\perp})$.

2.3.1 Many body interactions in ARPES

ARPES spectra can also be described within the Green's function formalism. The propagation of a particle through a many-body system is described by the time ordered Green's function. In the spectral representation the removal of an electron from the N -particle system at $T = 0$ is given by the following Green's function

$$G^-(\mathbf{k}, \epsilon) = \sum_s \frac{|\langle \Psi_s^{N-1} | c_k | \Psi_i^N \rangle|^2}{\epsilon - \epsilon_s^{N-1} + \epsilon_i^N - i\eta} \quad (2.21)$$

where η is small and positive. In the limit of $\eta \rightarrow 0^+$ the one-electron removal spectra which can be measured by photoemission is given by a one-particle spectral function

$$A^-(\mathbf{k}, \epsilon) = -\frac{1}{\pi} \Im m (G^-(\mathbf{k}, \epsilon - i\eta^+)) = \sum_s \langle \Psi_s^{N-1} | c_k | \Psi_i^N \rangle \delta(\epsilon - \epsilon_s^{N-1} - \epsilon_i^N) \quad (2.22)$$

For finite temperatures and within the sudden approximation the intensity of the ARPES spectrum is given by

$$I(\mathbf{k}, \epsilon) = I_0(\mathbf{k}, h\nu, \mathbf{A}) A(\mathbf{k}, \epsilon) f(\epsilon), \quad (2.23)$$

where $f(\epsilon)$ is a Fermi-Dirac distribution, ϵ is the electron energy with respect to the Fermi level, and $I_0(\mathbf{k}, h\nu, \mathbf{A})$ is proportional to the squared one-electron matrix element $|M_{\mathbf{k},f,i}|^2$.

The effect on the Green's function from many-body interactions can be described by the complex self-energy:

$$\Sigma(\mathbf{k}, \epsilon) = \Re \Sigma(\mathbf{k}, \epsilon) + i \Im \Sigma(\mathbf{k}, \epsilon), \quad (2.24)$$

which contains contribution from all many-body processes (electron-electron, electron-phonon, electron-impurity, etc.)

$$\Sigma(\mathbf{k}, E) = \Sigma^{el-el}(\mathbf{k}, \epsilon) + \Sigma^{el-ph}(\mathbf{k}, \epsilon) + \Sigma^{el-im}(\mathbf{k}, \epsilon) + \dots \quad (2.25)$$

The Green's and spectral functions in terms of self energy are given by

$$G(\mathbf{k}, \epsilon) = \frac{1}{\epsilon - \epsilon^0(\mathbf{k}) - \Sigma(\mathbf{k}, \epsilon)} \quad (2.26)$$

and

$$A(\mathbf{k}, \epsilon) = \frac{1}{\pi} \frac{\Im \Sigma(\mathbf{k}, \epsilon)}{(\epsilon - \epsilon^0(\mathbf{k}) - \Re \Sigma(\mathbf{k}, \epsilon))^2 + (\Im \Sigma(\mathbf{k}, \epsilon))^2}, \quad (2.27)$$

where $\epsilon^0(\mathbf{k})$ is the single-particle dispersion which can be approximated by band structure calculations.

For paramagnetic metals the contribution to the self energy comes mainly from the electron-electron, electron-phonon and electron-impurity interaction. In the following sections we will present model self-energies used later in the analysis of the data. In general any many-body process will have two effects on the observed spectrum. First, the position of the peak will be shifted by $\Re \Sigma(\mathbf{k}, \epsilon)$ (mass renormalization) and second, peaks will gain a finite width given by $2\Im \Sigma(\mathbf{k}, \epsilon)$ (quasi-particle lifetime).

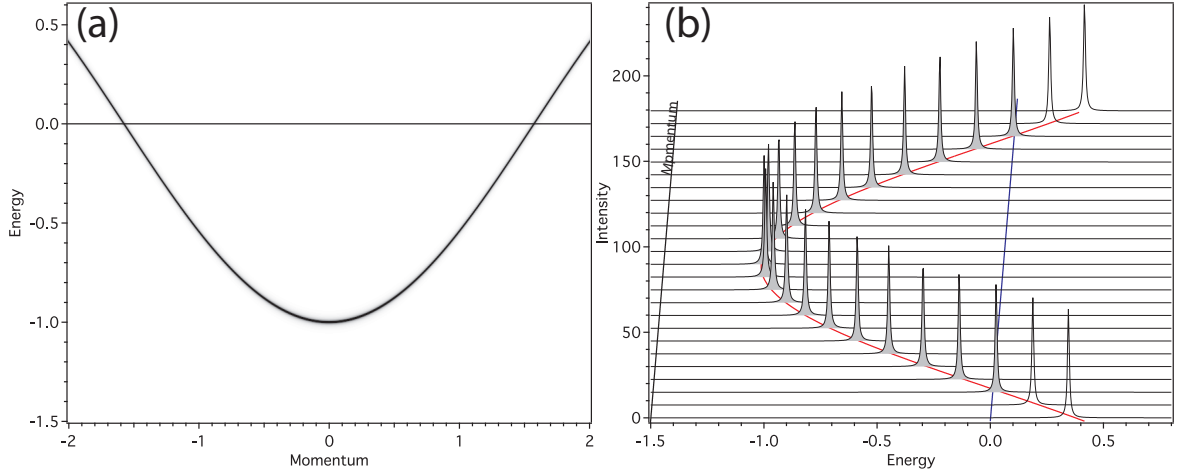


Figure 2.8: (a) Spectral function for a simple cosine band, (b) corresponding energy distribution curves.

If the electrons do not experience any interactions, i.e. $\Sigma(\mathbf{k}, \epsilon) = 0$, the Green's function

$$G^0(\mathbf{k}, \epsilon) = \frac{1}{\epsilon - \epsilon^0(\mathbf{k}) \pm i\eta} \quad (2.28)$$

has one pole for each \mathbf{k} and the spectral function

$$A^0(\mathbf{k}, \epsilon) = \frac{1}{\pi} \delta(\epsilon - \epsilon^0(\mathbf{k})), \quad (2.29)$$

consists of a delta peak centered at the single-electron energy $\epsilon^0(\mathbf{k})$. Figure 2.8 shows the spectral function for a simple band with cosine dispersion $\epsilon^0(\mathbf{k}) \propto \cos(\mathbf{k})$ in the absence of interactions. The left panel is a probability map of the energy as a function of momentum and the right panel shows energy distribution curves (EDCs) for different \mathbf{k} .

Electron-electron interaction

The spectral function for the general interacting system is given by equation 2.27. If $\Im m \Sigma(\mathbf{k}, \epsilon) \ll (\epsilon - \epsilon_0(\mathbf{k}) - \Re e \Sigma(\mathbf{k}, \epsilon))$ the spectral function $A(\mathbf{k}, \epsilon)$ is a Lorentzian peak of width $2\Im m \Sigma(\mathbf{k}, \epsilon)$ centered at $\epsilon'(\mathbf{k}) = \epsilon^0(\mathbf{k}) + \Re e \Sigma(\mathbf{k}, \epsilon)$ sitting on the background created by the continuum of the particle–hole excitations, as illustrated in figure 2.9. Because the spectral function describes the probability of adding or removing an electron with momentum \mathbf{k} and energy ϵ it has to fulfill the sum rule:

$$\int_{-\infty}^{+\infty} d\epsilon A(\mathbf{k}, \epsilon) = 1. \quad (2.30)$$

Using the above sum rule one can split the spectral function (and Green's function) into a part that describes the coherent quasi-particle peak A_c and the incoherent background A_{inc}

$$A(\mathbf{k}, \epsilon) = Z(\mathbf{k})A_c(\mathbf{k}, \epsilon) + (1 - Z(\mathbf{k}))A_{inc}(\mathbf{k}, \epsilon). \quad (2.31)$$

$Z(\mathbf{k})$ is called the quasi-particle weight and measures the overlap between electron and quasi-particle wavefunction. From the sum rule 2.30 $Z(\mathbf{k}) < 1$, which reflects the fact that the quasi-particle state is not an isolated state but an integral part of the coupled system.

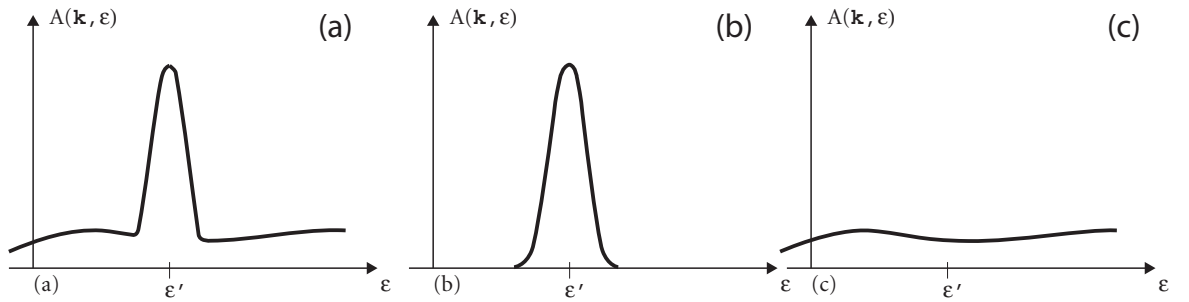


Figure 2.9: Separation of the spectral function (a) into quasi-particle peak centered at ϵ' (b) and particle–hole background (c).

Expanding the self-energy and leaving only first order terms the Green's function is given by

$$\begin{aligned}
G(\mathbf{k}, \epsilon) &= \frac{1}{\epsilon - \epsilon^0(\mathbf{k}) - \epsilon \frac{\partial \Re \epsilon \Sigma(\mathbf{k})}{\partial \epsilon} \Big|_{\epsilon=\epsilon(\mathbf{k})} - i \Im m \Sigma(\mathbf{k})} + \text{background} \\
&= \frac{Z(\mathbf{k})}{\epsilon - \epsilon'(\mathbf{k}) - i\Gamma(\mathbf{k})} + (1 - Z(\mathbf{k}))G_{inch}(\mathbf{k}, \epsilon)
\end{aligned} \tag{2.32}$$

from the definition of the spectral function 2.22:

$$A(\mathbf{k}, \epsilon) = \frac{1}{\pi} \frac{Z(\mathbf{k})\Gamma(\mathbf{k})}{(\epsilon - \epsilon'(\mathbf{k}))^2 + (\Gamma(\mathbf{k}))^2} + (1 - Z(\mathbf{k}))A_{inch}(\mathbf{k}, \epsilon), \tag{2.33}$$

where

$$Z(\mathbf{k}) = \left(1 - \frac{\partial \Re \epsilon \Sigma(\mathbf{k})}{\partial \epsilon} \Big|_{\epsilon=\epsilon(\mathbf{k})}\right)^{-1}, \quad \epsilon'(\mathbf{k}) = Z(\mathbf{k})\epsilon^0(\mathbf{k}), \quad \Gamma(\mathbf{k}) = Z(\mathbf{k})\Im m \Sigma(\mathbf{k}). \tag{2.34}$$

The poles of the Green's function for the interacting electron system have the energy (mass) renormalized by the factor $Z(\mathbf{k})$ and a finite width (lifetime). The quasi-particles can then be viewed as electrons dressed in the virtual excitations that move with them coherently. The incoherent part of the quasi-particle is hard to define rigorously as the coherent part already contains some of the low-lying excitations.

In the Fermi liquid regime $Z(\mathbf{k}) > 0$ the quasi-particle peak at the Fermi level is infinitely sharp, and its spectral weight $Z(\mathbf{k}_F)$ is proportional to the mass renormalization $\frac{m_0}{m^*}$, where m^* is the effective mass and m_0 is the single-electron band mass. If the band dispersion is linear in the vicinity of ϵ_F the renormalization constant is given by the ratio of the single-electron to the quasi-particle Fermi velocity (band slope at the Fermi level)

$$Z(\mathbf{k}_F) = \frac{v_F^0}{v_F^*}. \tag{2.35}$$

The self-energy for the 3D Fermi liquid system is

$$\Sigma^{el-el}(\epsilon, T) = \alpha\epsilon + i\beta [\epsilon^2 + (\pi k_B T)^2]. \tag{2.36}$$

The coherent part of the spectral function is then given by

$$A(\mathbf{k}, \epsilon) = \frac{1}{\pi} \frac{\beta' \epsilon^2}{(\epsilon - \epsilon'(\mathbf{k}))^2 + \beta'^2 \epsilon^4}, \tag{2.37}$$

where

$$Z(\mathbf{k}_F) = \frac{1}{1-\alpha}, \quad \epsilon'(\mathbf{k}) = Z(\mathbf{k}_F)\epsilon^0(\mathbf{k}), \quad \beta' = Z(\mathbf{k}_F)\beta. \tag{2.38}$$

Figure 2.10 presents the spectral function for the three dimensional Fermi liquid. Comparing to the non-interacting system (red line) the peaks are shifted to lower binding energies (band renormalization) meaning that quasi-particles are getting heavier. The quasi-particle peak has a finite width (lifetime) and sharpens up when approaching the Fermi level where it gets infinitely sharp (well defined quasi-particle).

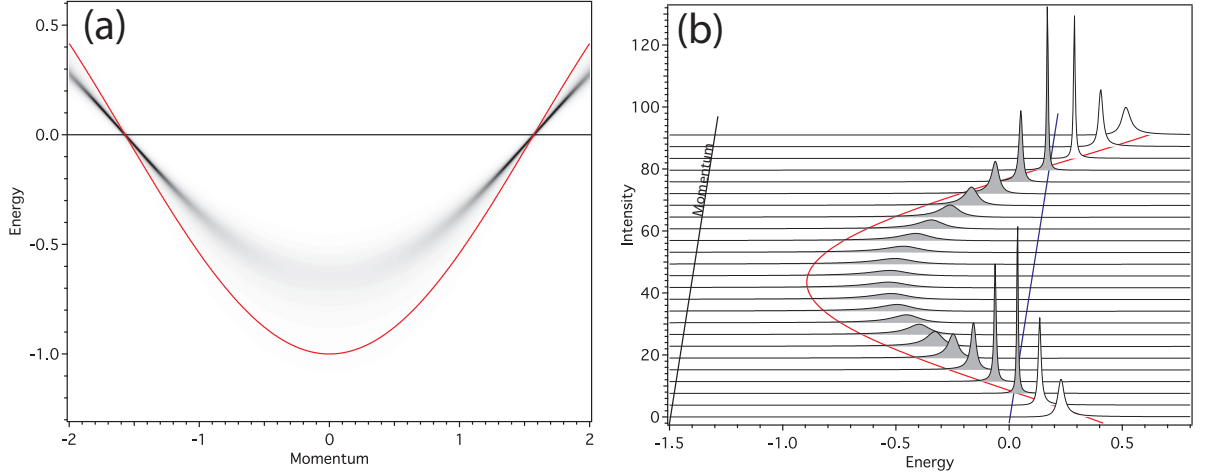


Figure 2.10: (a) Spectral function of the three dimensional Fermi liquid, (b) EDC's from panel (a). The red line is the non-interacting band.

Electron-phonon interaction

The interaction between electrons and lattice vibrations can strongly affect quasi-particle energies close to the Fermi level. In general the interaction of an electron with bosonic modes (phonons, magnons, plasmons, etc.) leads to two effects: an enhancement of the quasi-particle mass and a so called "kink" - a sudden change of the slope of the band at an energy characteristic for the given interaction (e.g. the Debye temperature for phonons).

The spectral function for the electron-phonon system is given by

$$A(\mathbf{k}, \epsilon) = \frac{1}{\pi} \frac{Z^{el-ph}(\mathbf{k}) \Gamma^{el-ph}(\mathbf{k})}{(\epsilon - \epsilon'(\mathbf{k}))^2 + (\Gamma^{el-ph}(\mathbf{k}))^2}, \quad (2.39)$$

where $\Gamma^{el-ph}(\mathbf{k}) = Z^{el-ph}(\mathbf{k}) \Im m \Sigma^{el-ph}(\mathbf{k}, \epsilon)$ and $Z^{el-ph}(\mathbf{k})$ is the electron-phonon renormalization constant given by

$$Z^{el-ph}(\mathbf{k}) = \left(1 - \frac{\partial \Re \Sigma^{el-ph}(\mathbf{k})}{\partial \epsilon} \Big|_{\epsilon=\epsilon(\mathbf{k})} \right)^{-1}. \quad (2.40)$$

The electron-phonon interaction can be described by the Eliashberg function $\alpha^2 F(\hbar\omega)$, where $F(\hbar\omega)$ is the phonon density of states and α is the electron-phonon coupling parameter. The self-energy for the electron-phonon interaction is given by [47]

$$\begin{aligned} \Sigma^{el-ph}(\mathbf{k}, \epsilon, T) &= \int d\epsilon' \int_0^{\hbar\omega_{max}} d(\hbar\omega) \alpha^2 F(\hbar\omega) \\ &\times \left[\frac{1-f(\epsilon', T)+n(\hbar\omega, T)}{\epsilon-\epsilon'-\hbar\omega} + \frac{f(\epsilon', T)+n(\hbar\omega, T)}{\epsilon-\epsilon'+\hbar\omega} \right], \end{aligned} \quad (2.41)$$

where $n(\hbar\omega, T)$ is the Bose-Einstein distribution, $f(\epsilon, T)$ is the Fermi-Dirac distribution, and $\hbar\omega_{max}$ is the maximum phonon energy.

For the imaginary part of Σ^{el-ph} one gets

$$\begin{aligned} \Im m \Sigma^{el-ph}(\mathbf{k}, \epsilon, T) &= \pi \int_0^{\hbar\omega_m} \alpha^2 F(\epsilon') \\ &\times [1 + 2n(\epsilon') + \dots + f(\epsilon + \epsilon') - f(\epsilon - \epsilon')] d\epsilon'. \end{aligned} \quad (2.42)$$

Debye model

In the Debye model the maximum phonon energy is given by the Debye energy $\hbar\omega_D$. The dispersion of phonon modes in three dimensions is linear, $\hbar\omega \propto \mathbf{k}$, and only the longitudinal modes interact with the electrons with $\alpha(\omega) = const..$ Hence, the Eliashberg function is proportional to the density of phonon levels and is given by

$$\alpha^2 F(\epsilon) = \begin{cases} \lambda \left(\frac{\epsilon}{\hbar\omega_D} \right)^2, & \epsilon \leq \hbar\omega_D, \\ 0, & \epsilon > \hbar\omega_D, \end{cases} \quad (2.43)$$

where λ is the mass-enhancement factor, and is defined by the change of the electronic group velocity $v_{\mathbf{k}} = \frac{1}{\hbar} \frac{\delta \epsilon}{\delta \mathbf{k}}$ which changes by a factor of $Z^{el-ph}(\mathbf{k}) = \frac{1}{1+\lambda}$ close to the Fermi level (the electronic density of states and the band mass increase by a factor of $(1 + \lambda)$). From eq. 2.40 we get the connection between λ and the real part of the electron-phonon self-energy

$$\lambda = - \left. \frac{\delta \Re e \Sigma^{el-ph}(\epsilon)}{\delta \epsilon} \right|_{\epsilon=\epsilon_F}, \quad (2.44)$$

The mass-enhancement factor is anisotropic and temperature dependent. It decreases with T and vanishes at high temperatures. The effect of mass renormalisation by electron-phonon coupling can be observed for various physical properties such as the electronic heat capacity at low temperatures, the cyclotron effective mass m_c in the de Hass-van Alphen effect, or the Fermi velocity. However, the shape of the Fermi surface remains unchanged. λ is given by the first moment of the Eliashberg coupling function at $T = 0$:

$$\lambda = \int_0^{\hbar\omega_{max}} \frac{\alpha^2 F(\hbar\omega)}{\hbar\omega} d(\hbar\omega). \quad (2.45)$$

In the limit of high temperatures, one gets a linear dependence of the imaginary part and the photoemission linewidth on the temperature

$$\Im m \Sigma^{el-ph}(T) = \frac{\Gamma^{el-ph}(T)}{2} = \pi \lambda k_B T, \quad k_B T \gg \hbar\omega_D. \quad (2.46)$$

In the limit of $T = 0$ one gets an analytical description for the energy dependence of the real and imaginary part of the self-energy

$$\Im m \Sigma^{el-ph}(\epsilon) = \frac{\Gamma^{el-ph}(\epsilon)}{2} = \begin{cases} \frac{\pi}{3} \lambda \frac{\epsilon^3}{(\hbar\omega_D)^2}, & \epsilon \leq \hbar\omega_D, \\ \frac{\pi}{3} \lambda \hbar\omega_D, & \epsilon > \hbar\omega_D. \end{cases} \quad (2.47)$$

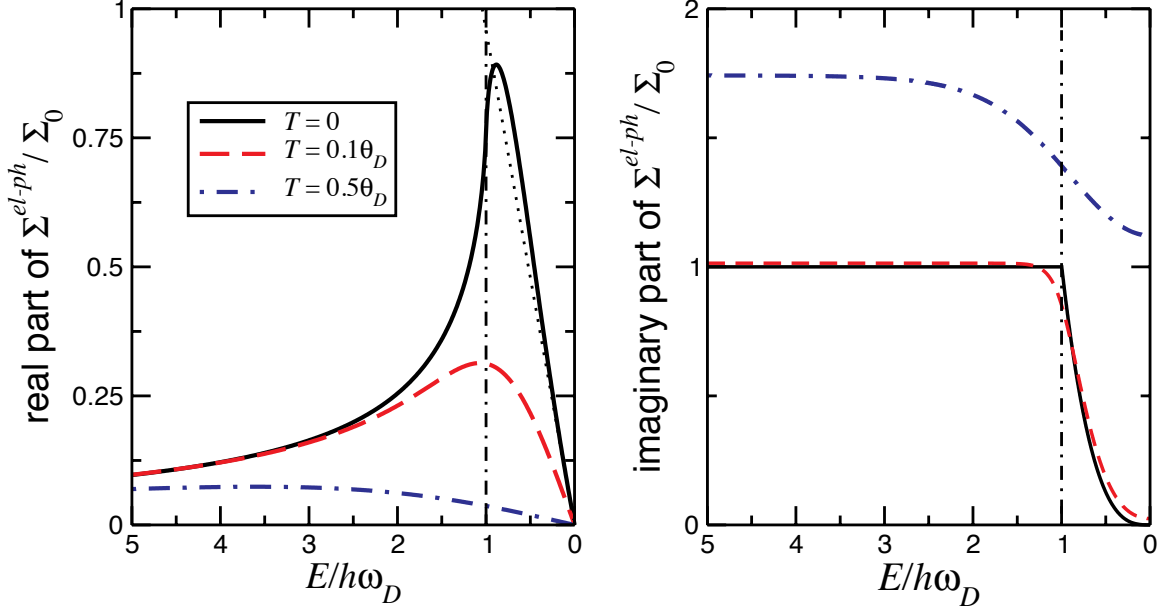


Figure 2.11: Plots of the energy dependence of the self-energy in the Debye model for $\lambda = 1$. Panel (a) gives the real part of the self-energy and panel (b) shows the imaginary part of the self-energy. θ_D is the Debye temperature, $\hbar\omega_D$ is the Debye energy and $\Sigma_0 = \frac{\pi}{3}\lambda\hbar\omega_D$ is the normalization constant. Figure reproduced from [46].

and

$$\Re\Sigma^{el-ph}(\epsilon) = -\lambda\frac{\hbar\omega_D}{3} \left[\left(\frac{\epsilon}{\hbar\omega_D}\right) + \left(\frac{\epsilon}{\hbar\omega_D}\right)^3 \ln \left| 1 - \left(\frac{\hbar\omega_D}{\epsilon}\right)^2 \right| + \ln \left| \frac{1 + \left(\frac{\epsilon}{\hbar\omega_D}\right)}{1 - \left(\frac{\epsilon}{\hbar\omega_D}\right)} \right| \right]. \quad (2.48)$$

The real part $\Re\Sigma^{el-ph}$ and imaginary part $\Im\Sigma^{el-ph}$ of the self energy are presented in figure 2.11. The real part increases linearly from ϵ_F and shows a maximum at the Debye temperature $\frac{\hbar\omega_D}{k_B}$. Increasing the temperature shifts the maximum to higher binding energies and decreases the value of $\Re\Sigma^{el-ph}$. The imaginary part at $T = 0$ has a sharp edge at $\hbar\omega_D$ that smears out with increasing temperature.

Figure 2.12 shows the spectral function of a simple cosine band $\epsilon^0(\mathbf{k}) \propto \cos(\mathbf{k})$ with electron-photon interaction. Panel (a) and (b) presents a gray scale plot and stack of EDCs, respectively. As one can see, below the Debye temperature $|\epsilon| > \hbar\omega_D$, the band has the original single-electron dispersion while above it, $|\epsilon| < \hbar\omega_D$, the electron dispersion is renormalized by $Z^{el-ph}(\mathbf{k}) = \frac{1}{1+\lambda}$.

In figure 2.13 (b) we show three EDCs from the electron-phonon spectral function. One intersecting the band at its bottom (black line), one at the Fermi level (blue line) and one at the Debye energy (red line). These EDCs reveal that the spectra are actually composed of two different branches. For binding energies above the Debye temperature $|\epsilon| \gg \hbar\omega_D$ the *electron mode* follows the original single-electron dispersion and the quasi-particle peak has a constant width and intensity. For $|\epsilon| \ll \hbar\omega_D$ the *phonon mode* has reduced dispersion, the quasi-particle peak width decreases and intensity increases when

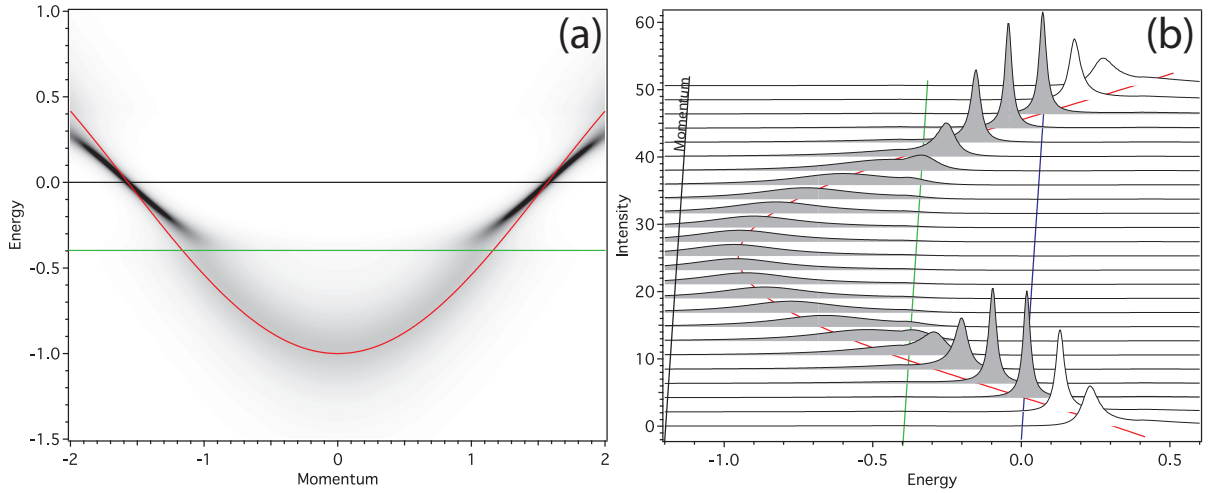


Figure 2.12: (a) Spectral function and (b) EDC stack for a cosine band coupled to phonons described by a Debye model. The red line denotes the non-interacting band.

approaching the Fermi level. Exactly at the Fermi level (for $T = 0$) the quasi-particle peak reaches its maximum height and is infinitely sharp. In the cross-over region for $|\epsilon| \sim \hbar\omega_D$, there is a transition from an *electron* mode to a *phonon* mode, the spectral weight of these two features gets comparable in this region and the quasi-particle peak is not well defined anymore. All spectra exhibit a characteristic three peak structure. In particular the cross-over region has rather complex structure due to the fact that both branches approach each other with similar spectral weight. For the states far away from the cross-over region (black and blue EDCs), the two incoherent features, located at $|\epsilon| = \hbar\omega_D$ have low spectral weight compared to the coherent part, however, they do not vanish.

Due to the complex shape of the spectral function, the peak positions from EDCs and MDCs for the electron-phonon coupled system differ substantially, as shown in figure 2.13 by red and green lines. While EDCs show three peak structure, and hence existence of two different branches, the MDCs are always composed of a single Lorentzian peak. This means that the MDC dispersion can be described by a single line (red line in figure 2.13 (a)) that shows a kink at $|\epsilon| = \hbar\omega_D$, where the dispersion changes from the unrenormalized to the renormalized band.

Momentum Distribution

The incoherent part of the spectrum has a marked influence on the momentum distribution. Its existence is simply a consequence of the interactions. The removal of an electron leaves the system in an excited state. For the non-interacting case, this excited state is an eigenstate of the system so the spectral function is a delta peak at the electron binding energy. In the interacting case, however, the excited state in general is not an eigenstate of the $(N - 1)$ -electron system and the spectral weight is spread over all states that have finite overlap with the groundstate. This means that the spectrum consist of the main peak (quasi-particle) and several satellites (incoherent part) – the exact number of which depends on the number of excited states created in the photoemission process. The fact

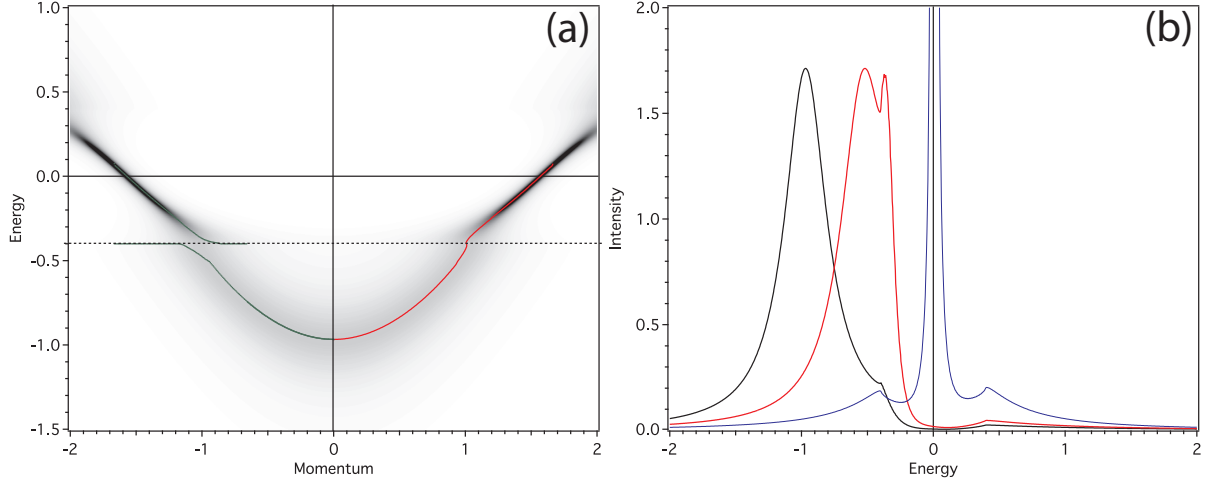


Figure 2.13: (a) Spectral function for an electron-phonon coupled system reproduced from figure 2.12 (a). The green line gives the peak position of the EDCs. Interaction splits the band into two branches, an *electron mode* below Debye temperature and a *phonon mode* above it. The red line shows the peak position fitted from MDCs and the *kink* in the dispersion visible at the Debye temperature. Panel (b) shows three representative EDCs. Black – band bottom, Blue – Fermi level, Red – cross-over region.

that the spectral weight is smeared over many states results in a reduced discontinuity at the Fermi level in the momentum distribution function $n(\mathbf{k})$ even at $T = 0$. The momentum distribution is given by

$$\int_{-\infty}^{+\infty} d\epsilon f(\epsilon) A(\mathbf{k}, \epsilon) = n(\mathbf{k}). \quad (2.49)$$

where $f(\epsilon)$ is the Fermi distribution function. The size of the discontinuity is given by the total renormalization resulting from electron-electron and electron-phonon interaction. For a Fermi liquid coupled to a Debye spectrum of phonons:

$$Z^{tot}(\mathbf{k}_F) = \frac{1}{1 - \left. \frac{\partial \Re \Sigma^{el-el}}{\partial \epsilon} \right|_{\epsilon=\epsilon_F} - \left. \frac{\partial \Re \Sigma^{el-ph}}{\partial \epsilon} \right|_{\epsilon=\epsilon_F}} = \frac{1}{1 - \alpha + \lambda}. \quad (2.50)$$

In the non-interacting system the discontinuity at the Fermi wave vector \mathbf{k}_F defines the Fermi surface – there are no states outside the Fermi surface. In the case of the interacting system there is a finite occupation probability even for states with $\mathbf{k} > \mathbf{k}_F$. However, for a Fermi liquid the discontinuity is always finite ($Z > 0$) so one can still identify the Fermi surface by locating the maxima of $|\nabla_{\mathbf{k}} n(\mathbf{k})|$.

The fact that the self-energy for the Fermi liquid and the Debye model is momentum independent means that the renormalized (quasiparticle) band crosses the Fermi level at exactly the same Fermi wave vector as the non-interacting band. This means that the Fermi surface shape and volume calculated within one-particle theory (like density functional theory or tight binding model) should be exactly the same as the one measured by ARPES. Deviations from the single-particle Fermi surface indicate more exotic many-body correlations exceeding the framework of these two standard models describing many-particle systems.

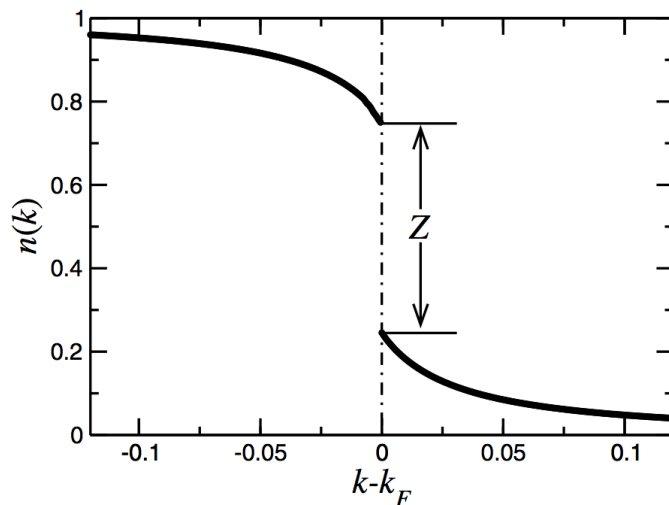


Figure 2.14: Momentum distribution for the interacting system. The step size is given by the total renormalization resulting from electron–electron and electron–phonon interaction [46].

2.3.2 Matrix elements, final state effects and finite resolution effects

In a real experiment the extraction of quantitative information from ARPES data is further complicated by effects of matrix elements, finite experimental resolution and due to the background of secondaries. The total measured intensity can be then written as

$$I(\mathbf{k}, \epsilon) = [I_0(\mathbf{k}, h\nu, \mathbf{A})f(\epsilon)A(\mathbf{k}, \epsilon) + B] \otimes [R(\Delta\epsilon)Q(\Delta\mathbf{k})], \quad (2.51)$$

where B is the background, $R(\Delta\epsilon)$ is the energy and $Q(\Delta\mathbf{k})$ is the momentum resolution function and \otimes denotes the convolution. The convolution leads to mixing of momentum and energy space. Momentum resolution affects not only MDCs but also EDCs and vice versa. There is no easy way around this problem. Standard deconvolution techniques do not work for ARPES data and full 2D fitting demands a large number of parameters. So usually there are some simplification applied to the fitting procedure.

$I_0(\mathbf{k}, h\nu, \mathbf{A}) \propto |M_{f,i}(\mathbf{k})|^2$ for simplicity of the data analysis is usually assumed to be unity, however, this term may have a strong effect on the measured photocurrent and can even lead to the complete suppression of the intensity. It depends on the photon energy, polarization and experimental geometry.

The matrix elements are proportional to the overlap between initial and final state wavefunction

$$|M_{\mathbf{k},f,i}|^2 \propto |\langle \phi_{\mathbf{k},f} | \mathbf{A} \cdot \mathbf{p} | \phi_{\mathbf{k},i} \rangle|^2 \quad (2.52)$$

The matrix element will be nonzero only if the product of terms in the overlap integral is even function with respect to the mirror plane. The final state wavefunction $\phi_{\mathbf{k},f}$ must be even which means that in order to get non vanishing intensity the other two terms have to be simultaneously even or odd. This means that by choosing the polarization of the light one can choose which atomic orbital to probe. Figure 3.8 presents the situation for

the $d_{x^2-y^2}$ orbital which is even. Hence, the photoemission process is symmetry allowed only for \mathbf{A} even (p - polarization).

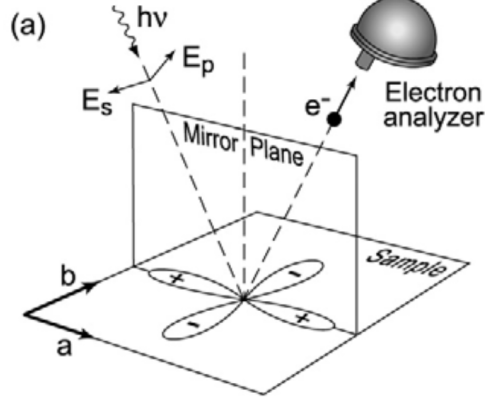


Figure 2.15: Mirror plane emission from a $d_{x^2-y^2}$ orbital. Figure reproduced from [44].

Another complication that may arise in the interpretation of ARPES data is that the experimental linewidth contains contributions from the photohole (initial state) and photoelectron (final state). The spectral function derived in the previous section describes only the initial state of the system. However, the contribution to the spectra from the final states can be quite large and complex. In general it can be described by a convolution of the spectral function of the photohole with the spectral function of the photoelectron. In the case of a weakly interacting system, the contributions from photohole and photoelectron can be described by Lorentzians with linewidths Γ_i (photohole) and Γ_f (photoelectron). The resulting linewidth Γ_m is a linear combination of these two, given by

$$\Gamma_m = \frac{\frac{\Gamma_i}{|v_{i\perp}|} + \frac{\Gamma_f}{|v_{f\perp}|}}{\left| \frac{1}{v_{i\perp}} \left(1 - \frac{mv_{i\parallel} \sin^2 \theta}{\hbar k_{\parallel}} \right) - \frac{1}{v_{f\perp}} \left(1 - \frac{mv_{f\parallel} \sin^2 \theta}{\hbar k_{\parallel}} \right) \right|}, \quad (2.53)$$

where $\hbar v_{(i,f)\perp} = \delta\epsilon/\delta k_{\perp}$. For normal emission ($\theta = 0^\circ$) and with $|v_{i\perp}| \ll |v_{f\perp}|$

$$\Gamma_m \approx \Gamma_i + \left| \frac{v_{i\perp}}{v_{f\perp}} \right| \Gamma_f. \quad (2.54)$$

In two dimensional systems the group velocity of the photohole perpendicular to the surface vanishes and measured linewidths are given by

$$\Gamma_m = \frac{\Gamma_i}{1 - \frac{mv_{i\parallel} \sin^2 \theta}{\hbar k_{\parallel}}} = C\Gamma_i. \quad (2.55)$$

This means that in quasi two dimensional systems the spectra at or close to normal emission represent the initial state properties of the photohole. However, at angles far from normal emission - $v_{i\parallel} < 0$ and small k_{\parallel} , the measured linewidth can be narrower than Γ_i which is a direct consequence of the kinematic constraints of the photoemission process (kinematic compression).

2.4 Experimental Setup

The ARPES system at the University of St Andrews has been built and commissioned during this project in collaboration with SPECS GmbH. It is part of the Scottish Centre for Interdisciplinary Surface Spectroscopy (SCISS) founded by the Scottish Funding Council (SFC). Figure 2.16 shows a photograph and a CAD model drawing of the system. The most important parts of every ARPES system are the electron spectrometer (Analyzer) and the light source. Typical laboratory light sources include UV discharge lamps, lasers and various X-ray sources. Due to the very short photoelectron mean free path, ARPES measurements are extremely surface sensitive and thus require ultra high vacuum (UHV) pressures $p < 1 \times 10^{-10}$ mbar. Any impurities on the sample surface cause strong scattering in the initial state resulting in broader and less intense quasi-particle peaks.

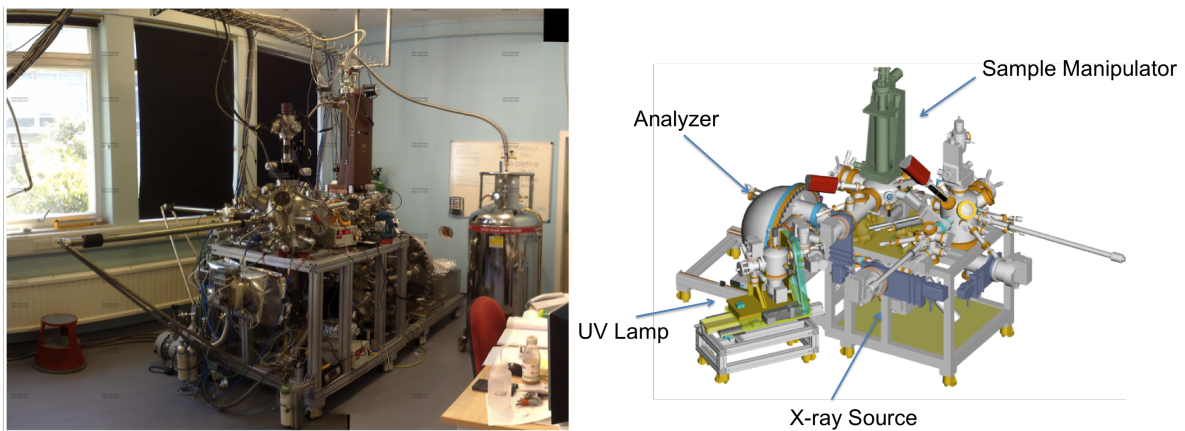


Figure 2.16: UHV ARPES system built up at the University of St Andrews during this PhD project.

Often 10% of a monolayer of contamination is enough for the detailed information about many-body processes to be lost. This means that the sample lifetime can be specified by the time needed to obtain a coverage of one monolayer on a surface. At a pressure of 10^{-9} mbar and a sticking coefficient near 1, it takes only 20 minutes to form a monolayer whereas at 10^{-11} mbar this time increases to two days. It is therefore very important to work at as low pressures as possible. For this reason part of this work was devoted to improvements of the sample lifetime by lowering the residual pressure of the system. In order to keep the pressure in the range of $< 5 \times 10^{-11}$ mbar getter pumps and a radiation shield have been built, details of which will be discussed in the next section.

The heart of the system is the hemi-spherical electron energy analyser PHOIBOS 225 from SPECS GmbH. This hemi-spherical deflection analyser consists of two concentric hemispheres, with mean radius of 225 mm, that are kept at a potential difference ΔV , symmetric around the center line potential called pass energy E_{pass} (see figure 2.17). Electrons that reach the entrance slit of the analyzer with the energy E_{pass} and direction normal to the entrance slit plane will then move along the path

$$R_{pass} = \frac{R_{in} + R_{out}}{2}, \quad (2.56)$$

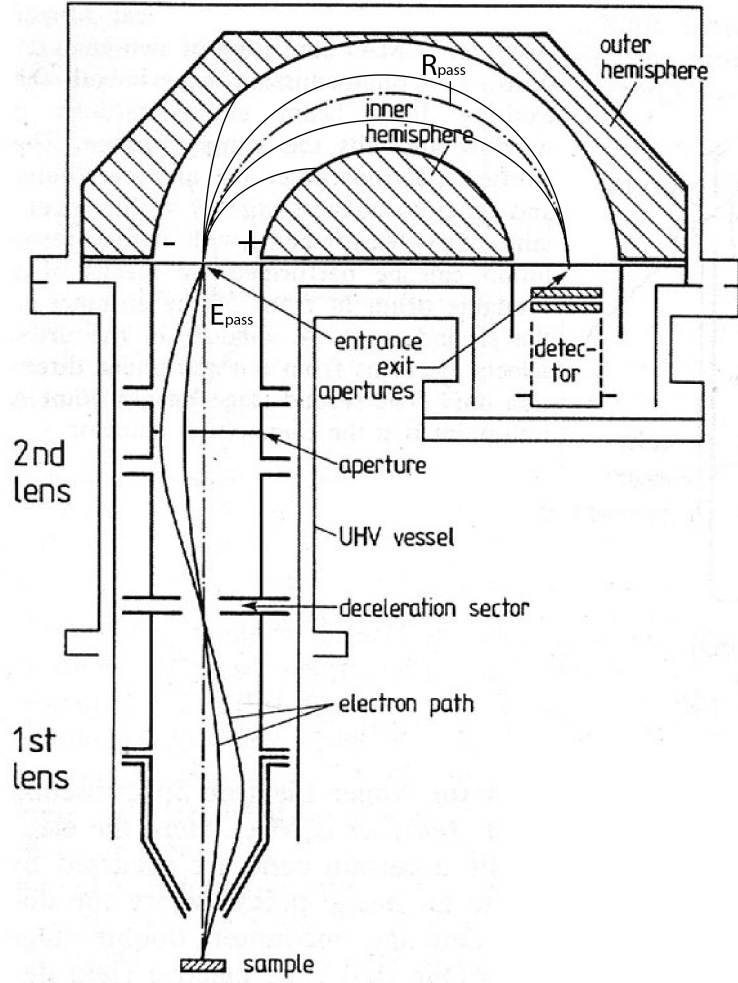


Figure 2.17: Cross-section through a hemi-spherical deflection analyser. Figure reproduced from [48].

where R_{in} and R_{out} are the radii of the inner and outer hemisphere respectively. Electrons whose energy differs from E_{pass} and emission angle differs from normal will be deflected by the electrostatic field. There is a narrow window of electron energies and emission angles centered at E_{pass} that can travel through the hemispheres to the exit slit without collision with the hemisphere walls. The size of this window depends on the pass energy and the size of the detector, and is typically $\sim 10\%$ of E_{pass} .

Once the electrons pass the hemispheres they are then counted by the detector. The analyser is equipped with a 2D-CCD detector that features a 12 bit digital camera with dynamic range of 1000. Two dimensional channel plates allow for the simultaneous measurement of photoelectrons with different kinetic energy and emission angle. Photoelectrons with different kinetic energy are spread along the Y -axis of the detector and with different emission angle along the X -axis.

The resolution of the hemispherical analyser is given by

$$\Delta E = E_{pass} \frac{w + d}{R_{pass} + \frac{\alpha^2}{4}}, \quad (2.57)$$

where w is the width of the entrance slit, d is detector spatial resolution, and α is acceptance angle. Because with the electrostatic field one can decelerate electrons without changing their absolute energy spread and the resolution is proportional to the pass energy, the analyzer is equipped with an electrostatic lens system that focuses and decelerates electrons before they enter the hemispheres. The analyzer contains a slit orbit mechanism allowing for the selection of one of 8 pairs of entrance slits and one of 3 exit slits. Each of the entrance positions provides a pair of slits that limits the maximum angle of acceptance, which enhances the resolution but reduces the intensity. The lens may be operated in different modes for angular or spatially resolved studies. The energy resolution is in the range of $\Delta\epsilon = 3 \div 10$ meV depending on the combination of pass energy, lens mode and slit size. Because magnetic fields can strongly affect the electron trajectories, the analysis chamber is entirely made out of μ -metal. Analyser and the electron lens have double magnetic shielding reducing the magnetic field even further.

The sample manipulator used in this work was designed by A. Tamai and F. Baumberger. It allows to translate the samples along three axes and to rotate it in three planes. Despite its mechanical complexity samples can be cool down to as low as 2.6 K using a continuous flow He cryostat.

Photons are produced by a duo-plasmatron discharge He lamp (UVS 300, SPEC Gmbh) that is connected to the UHV measuring chamber through a toroidal mirror-plane grating UV Monochromator (TMM 304, SPECS Gmbh). The UVS 300 generates a high density plasma by guiding the electrons from a hot cathode filament along the lines of a strongly inhomogeneous magnetic field towards the small discharge region. The strong ultraviolet radiation is extracted from the cathode side by the combination of a metal and a quartz capillary. In addition to the extremely high intensity of the atomic line He I α (21.2 eV), the high density plasma of the UVS 300 generates a very high intensity ion line He II α (40.8 eV). The monochromator contains two cassettes with mirrors and gratings optimised for maximal transmission at He I α and He II α , respectively. The whole system contains four differential pumping stages enabling it to work at pressures $< 2 \times 10^{-11}$ mbar in the analysis chamber.

2.4.1 Getter Pumps

The main problem in achieving UHV is outgassing of surfaces. When chambers are opened to air H₂O, O₂, N₂ and other gasses adsorb on the chamber walls. The desorption time for these gasses at room temperature can be as long as a few months. Because the desorption depends exponentially on the temperature the way to accelerate it is bakeout of the system at temperature of $\sim 150^\circ\text{C}$. This procedure allows to reach pressures of $\sim 1 \times 10^{-10}$ mbar. For our system the complete bakeout takes around two weeks. The main drawback of the commercial turbo-pump based pumping system is its low efficiency in removing hydrogen which constantly diffuses from the grain boundaries of the stainless steel chamber walls. To reduce the hydrogen partial pressure we built two additional pumps. A getter pump and a cryopump that is located around the sample manipulator which also serves to lower the temperature of the sample surface.

Getter pumping is achieved by binding the gas molecules in the form of stable chemical compounds. The pump consists of a droplet of getter material that is resistively heated what results in evaporation and coating of the chamber walls. The three dimensional

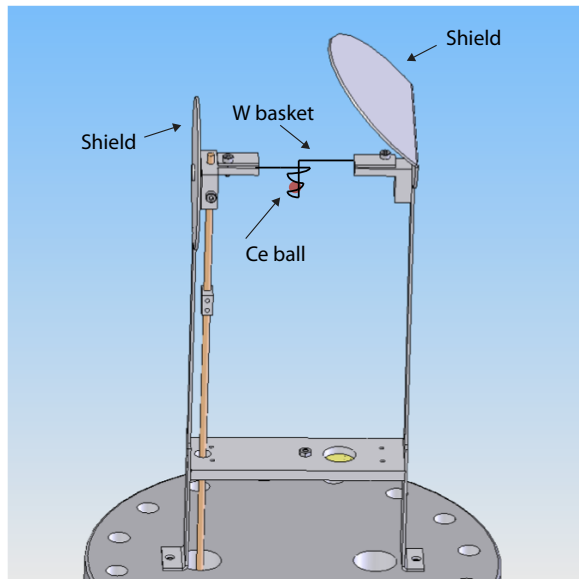


Figure 2.18: Ce evaporator. Ce ball is placed in the filament basket made of tungsten. Pump is placed in the pumping tube connecting a turbo-molecular pump with a chamber. Shields protect the turbo-molecular pump and the instrumentation in the chamber.

model of our design is presented on figure 2.18.

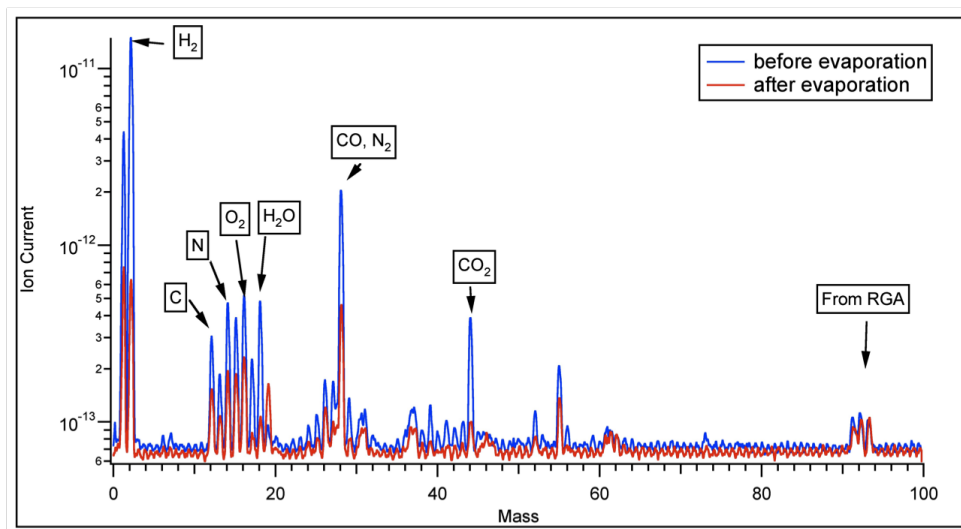


Figure 2.19: Residual Gas Analysis scans before and 12 hours after Ce evaporation.

For the getter material we have chosen Cerium which is highly reactive not only with oxygen, nitrogen, water and carbon monoxide but can also pumps hydrogen efficiently. Cerium is the only getter for which hydrogen diffuses in the bulk even if the surface is oxidized. Figure 2.19 shows Residual Gas Analysis (RGA) scans performed before and 12 hours after Ce evaporation. Within this time the pressure dropped from 2×10^{-10} mbar to 5×10^{-11} mbar. Ultimately pressures of $2 - 3 \times 10^{-11}$ can be reach depending on the amount of Ce that is evaporated. The RGA scans confirm the drop in all the residual

gases by at least factor of two. The evaporation needs to be repeated every few weeks after the Cerium is saturated.

2.4.2 Radiation Shield

Most of the "heavy" gases are pumped by turbomolecular and getter pumps. The hydrogen remains a problem even with the getter pumping because it continuously diffuses from the grain boundaries of the parts of the chamber walls that for technical reasons could not be coated with the getter. To lower the pressure in the sample region even further we have built a cryopump that surrounds the sample manipulator in the analysis chamber. Cryo pumping uses van der Waals forces, which, at low temperatures, are strong enough to bind the gas particles either together to form a condensate or on the solid surfaces (cryosorption).

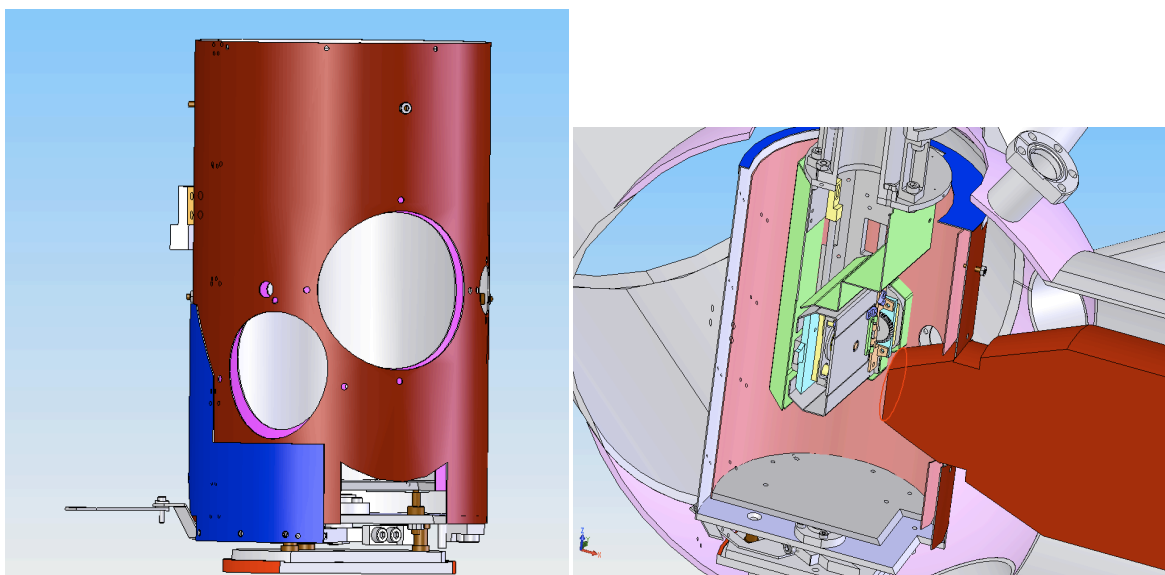


Figure 2.20: Left panel: standalone coldshield. Right panel: Coldshield in the analysis chamber.

The energies of cryosorption for most gases are larger than those of vaporisation by a factor of 2 to 3 for heavy gases but 10 for hydrogen and around 30 for helium. As a consequence hydrogen can be effectively cryosorbed at 20 K, helium at 4.2 K and rest of the gases at their boiling temperature which is not lower than the temperature of liquid nitrogen.

This means that a very effective cryopump can be already operated at liquid nitrogen temperature. In our case, however, the problem constitutes the hydrogen. The cryopump we built is cooled by a UHV closed cycle cryostat from Advanced Research Systems. The cryostat is directly mounted on the measurement chamber and connected to the cryopump with a pair of oxygen free high purity copper braids. The cryopump itself is made of two concentric cylinders (shields) made of ultra pure aluminum with openings for the UV lamp capillary, analyzer, laser beam and the camera. The camera viewport stays closed during the measurement and is only opened when the sample needs to be aligned. The shields

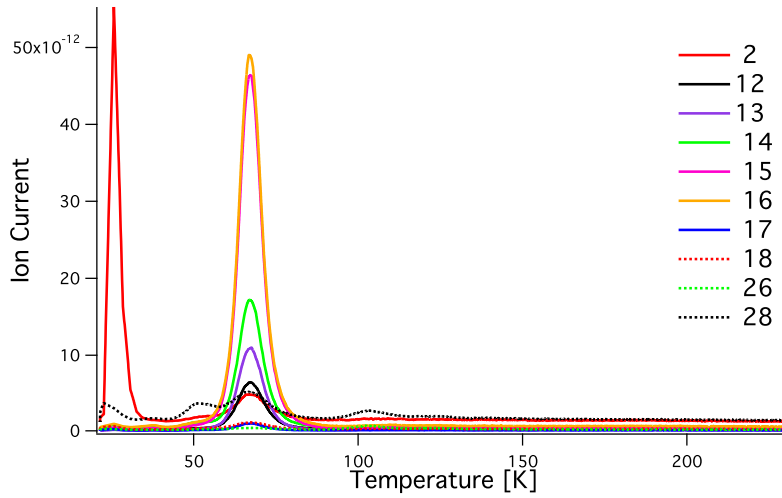


Figure 2.21: Thermal desorption spectrum. Note that the temperature ramp used in this experiment is strongly nonlinear.

are fixed to the chamber bottom with vespel legs which thermally isolate the pump from the chamber. The outer cylinder which serves as a cryoshield for the inner cylinder is connected to the 1st cooling stage (50–80 K) and achieves a temperature of 120 K. The inner shield is connected to the cold head (9 K) and reaches a temperature of ~ 16 K which is sufficient to cryosorb hydrogen. The outer shield is necessary to lower the heat load on the inner shield. The main source of the heatload is thermal radiation from the chamber walls which is proportional to T^4 . Hence, the additional shield reduces the heat load on the inner shield by a factor of 200 which is crucial to achieve temperatures below 20 K.

Figure 2.21 shows the thermal desorption during cryopump warm up. The cryopump was kept running for at least 48 hours at operating temperature (16 K). The chamber gas content was then recorded as a function of the inner shield temperature. The results clearly confirm pumping of hydrogen (large peak at 20 K) together with other heavy gases (secondary peak around 70K).

The second important purpose of the pump is to use it as a radiation shield for the sample. We found that operating the cold-shield reduces the base temperature of the manipulator from ~ 3.5 K to ~ 2.6 K.

Chapter 3

Band structure of Sr_2RuO_4

The electronic band structure determines most thermodynamic and transport properties of solids. Common methods for band structure calculations include the Tight Binding model (TB) and Density Functional Theory (DFT) in the Local Density Approximation (LDA). Both of these methods use a mean-field description of the many-body problem, i.e. they describe a single electron propagating in the averaged potential of all ions and other electrons. The TB model is particularly useful because of its flexibility and possible extensions to more sophisticated models describing many-body correlations (e.g. t-J model [49] or Random Phase Approximation (RPA) [50]). The local density approximation on the other hand is parameter free and its solution is an exact single-electron ground state of a given system which makes it useful in the analysis of spectral function measured by ARPES. This chapter will present the theoretical principles of both methods and some results obtained for Sr_2RuO_4 . We will also discuss the influence of spin-orbit coupling on the band structure and effects of magnetic fields.

3.1 Introduction

The Hamiltonian describing a many-particle system composed of N nuclei and n electrons is given by

$$\begin{aligned} \hat{H} = & -\frac{\hbar^2}{2} \left(\sum_{i=0}^N \frac{\nabla^2(\mathbf{R}_i)}{M_i} + \sum_{i=0}^n \frac{\nabla^2(\mathbf{r}_i)}{m_i} \right) - \frac{1}{4\pi\epsilon_0} \sum_{i=0}^N \sum_{j=0}^n \frac{e^2 Z_i}{|\mathbf{R}_i - \mathbf{r}_j|} \\ & + \frac{1}{8\pi\epsilon_0} \sum_{i=0}^n \left(\sum_{j \neq i}^n \frac{e^2}{|\mathbf{r}_i - \mathbf{r}_j|} + \sum_{j \neq i}^N \frac{e^2 Z_i Z_j}{|\mathbf{R}_i - \mathbf{R}_j|} \right), \end{aligned} \tag{3.1}$$

where \mathbf{R}_i , M_i and Z_i are the position, mass and charge of the i -th nucleus, \mathbf{r}_i and m_i is the position and mass of i -th electron. For charge neutral systems the number of electrons is given by $n = ZN$. The first and second terms describe the kinetic energy of nuclei and electrons respectively, the third term is the interaction between electrons and nuclei, while the fourth and fifth terms describe the interaction of the i -th electron with other

electrons and the i -th nucleus with other nuclei respectively. In principle the eigenstates and eigenfunctions could be found by solving the stationary Schrödinger equation

$$\hat{H}\Psi = E\Psi. \quad (3.2)$$

However, for a macroscopic system containing around 10^{23} particles this problem is not exactly solvable, even with the most powerful computing facilities. A straight forward simplification is the Born-Oppenheimer approximation. Because nuclei are much heavier, and hence much slower than the electrons, they can be thought of as being fixed in their equilibrium positions. This significantly reduces the problem as the kinetic energy of the nuclei is now zero and the last term of the Hamiltonian 3.1 becomes a constant. This simplifies the description of solids to the problem of interacting electrons moving in the static periodic potential created by the lattice. It breaks down the Hamiltonian to three terms

$$\hat{H} = \hat{T} + \hat{U} + \hat{U}_{lattice}, \quad (3.3)$$

where \hat{T} is the electron kinetic energy, \hat{U} is the interaction between electrons and $\hat{U}_{lattice}$ is the potential created by the lattice. Still, this problem cannot be solved exactly as the number of particles (and thus the number of coupled equations) is $\approx 10^{23}$.

The simplest way forward is to neglect the interaction between the electrons and between electrons and lattice. The whole problem is then reduced to the problem of a gas of noninteracting fermions and the electron energy is given by $E = \frac{\hbar^2 \mathbf{k}^2}{2m_e}$. This simple model can be used to describe some basic properties of metals, however, it completely fails to even account for the existence of semiconductors and insulators. In a more realistic description of solids one needs to include the interaction of electrons with the periodic potential of the ion cores. Because the core electrons strongly screen the charge of the nucleus, the lattice potential can often be treated as a small perturbation to the free-electron energy. The most general consequence of such a weak periodic potential is the opening of band gaps at the Brillouin zone boundaries.

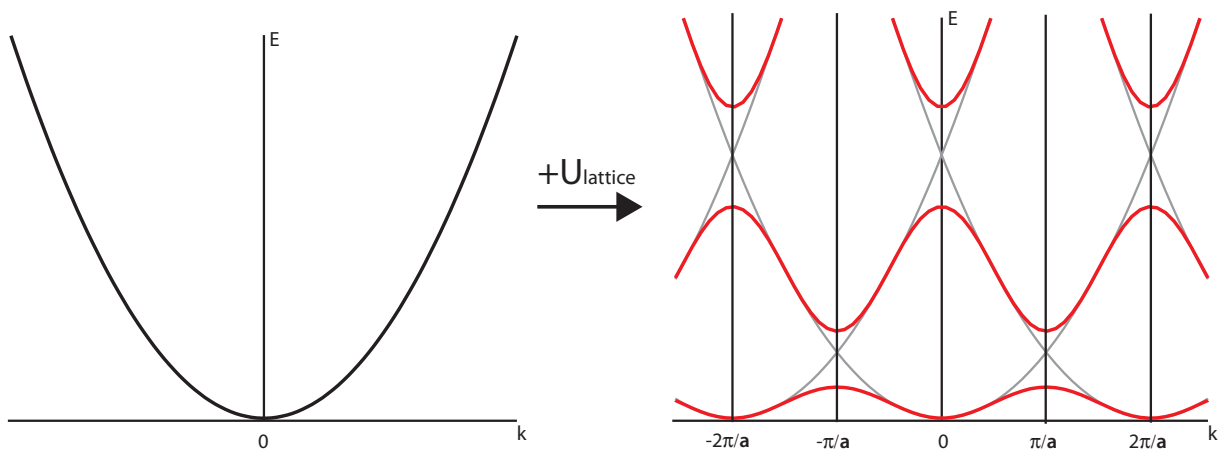


Figure 3.1: (a) Free-electron parabola, (b) periodic potential leads to formation of bands and the opening of gaps at Brillouin zone boundaries.

Away from the Brillouin zone boundaries the electron dispersion is still parabolic, which is equivalent to describing an electron as a plane wave propagating through the

crystal. This picture is appropriate only far away from the real space lattice sites. In the vicinity of ions the electron feels a strong positive potential and will at least partially retain its "atomic" behavior. The electronic wavefunction can then be described as a linear combination of atomic orbitals. This is the basis of the tight binding model, which is especially effective for partially localized d -electrons in transition metals and transition metal oxides.

Density functional theory is an alternative approach to finding the ground state of a many-body system. DFT is based on the Hohenberg-Kohn theorems stating that the ground state of a many-particle system is uniquely defined by the electron density. Hence, the method can in principle map the many-electron problem onto a single-electron one.

In the following two sections I will give more details of the tight binding model and briefly describe density functional theory within local density approximation.

3.2 The Tight Binding Model

The problem of solving the Schrödinger equation 3.2 for the crystal Hamiltonian

$$\hat{H} = \hat{T} + \hat{U}_{lattice}, \quad (3.4)$$

is essentially the problem of choosing an appropriate basis set of wave functions. Because the crystal possesses translational symmetry the electron wave function $|\Psi\rangle$ should meet the Bloch theorem:

$$T_{\mathbf{a}_i}|\Psi\rangle = e^{i\mathbf{k}\cdot\mathbf{a}_i}|\Psi\rangle, \quad (3.5)$$

where $T_{\mathbf{a}_i}$ is a translation by the lattice vector \mathbf{a}_i , and \mathbf{k} is the wave vector. There are many different $|\Psi\rangle$ fulfilling equation 3.5. A particularly useful basis set is given by the Wannier functions [51]

$$|\Phi_j\rangle = \frac{1}{\sqrt{N}} \sum_{\mathbf{R}_i}^N e^{i\mathbf{k}\cdot\mathbf{R}_i} |\varphi_j\rangle, \quad i = 1, 2, \dots, \quad j = 1, \dots, n, \quad (3.6)$$

where \mathbf{R}_i is the position of i -th atom in the unit cell, $|\varphi_j\rangle$ can be associated with the atomic wave function in a state j , n is the number of atomic wave functions in the unit cell, and N is the number of unit cells.

One can then express the eigenfunctions of the crystal, through linear combinations of the basis functions

$$|\Psi_j\rangle = \sum_{j'=1}^n C_{jj'} |\Phi_{j'}\rangle, \quad j = 1, \dots, n. \quad (3.7)$$

To find the final form of wave functions one has to determine the coefficients $C_{jj'}(\mathbf{k})$, through calculation of the j -th eigenvalue $E_j(\mathbf{k})$, for the crystal Hamiltonian H

$$E_j(\mathbf{k}) = \frac{\langle \Psi_j | H | \Psi_j \rangle}{\langle \Psi_j | \Psi_j \rangle} = \frac{\sum_{j,j'=1}^n H_{jj'}(\mathbf{k}) C_{ij}^* C_{ij'}}{\sum_{j,j'=1}^n S_{jj'}(\mathbf{k}) C_{ij}^* C_{ij'}}, \quad (3.8)$$

where $H_{jj'}(\mathbf{k}) = \langle \Phi_j | H | \Phi_{j'} \rangle$ and $S_{jj'}(\mathbf{k}) = \langle \Phi_j | \Phi_{j'} \rangle$, ($j, j' = 1, \dots, n$). H_{ij} and S_{ij} are called the transfer matrix and the overlap matrix respectively. Ritz' variation theorem

says that for each value of \mathbf{k} , the coefficients C_{ij}^* have to minimize the energy $E_i(\mathbf{k})$. After differentiating equation 3.8 with respect to C_{ij}^* one obtains

$$\sum_{j'=1}^n C_{ij'} H_{jj'}(\mathbf{k}) = E_i(\mathbf{k}) \sum_{j'=1}^n C_{ij'} S_{jj'}(\mathbf{k}). \quad (3.9)$$

The above equation can be transformed to

$$HC_i = E_i(\mathbf{k})SC_i. \quad (3.10)$$

Moving the right-hand side of equation (3.10) to the left gives

$$[H - E_i(\mathbf{k})S]C_i = 0. \quad (3.11)$$

A nontrivial solution of equation 3.11 exists only if the matrix $[H - E_i(\mathbf{k})S]$ has a reciprocal matrix, which is equivalent to the condition

$$\det [H - E_i(\mathbf{k})S] = 0. \quad (3.12)$$

The above equation is called the secular equation. Its solution gives n eigenvalues $E_i(\mathbf{k})$ ($i = 1, \dots, n$) for each \mathbf{k} . With $E_i(\mathbf{k})$ one can find the coefficients C_i , that are necessary to determine the final form of the eigenfunction of the crystal $|\Psi_j\rangle$.

In section 3.6 we will use the tight binding method to parametrize the band structure of Sr_2RuO_4 calculated within DFT. We will then include the spin-orbit coupling and use this model to study the band structure of Sr_2RuO_4 in a magnetic field.

3.3 Density Functional Theory

Density Functional Theory provides an alternative to the Schrödinger equation for evaluating properties of solids. The first Hohenberg–Kohn theorem states that there exists a one to one correspondence between the electron ground state density $\rho(\mathbf{r})$ and the potential acting on the electrons. The first two terms in the Hamiltonian 3.3 ($\hat{T} + \hat{U}$) are system independent. They describe the part of the electron energy that results from the interactions with other electrons. This term is always the same meaning that $\hat{T} + \hat{U}$ are universal. All system dependent interactions are contained in $\hat{U}_{lattice}$ which is unique for a given system. This in turn leads to unique ground state wave function. Because the electron density can be calculated from the wave function, $\hat{U}_{lattice}$ generates a unique electron ground state density.

According to the second Hohenberg-Kohn theorem the total energy can be obtained by minimization of the total energy as a functional of the electron density $\rho(\mathbf{r})$

$$E[\rho] = T[\rho] + U[\rho] + \int U_{lattice}[\rho]\rho(\mathbf{r})d\mathbf{r}. \quad (3.13)$$

The system independent part can be rewritten to

$$E[\rho] = T[\rho] + U[\rho] + U_{lattice}[\rho] = T_0[\rho] + U_H[\rho] + U_{xc}[\rho] + U_{lattice}[\rho], \quad (3.14)$$

where T_0 is the functional for the kinetic energy of the non-interacting electron gas, U_H is the Hartree term describing the Coulomb interactions and U_{xc} is the exchange-correlation energy that contains all many-body interactions. The correlation part describes the effects that arise from the fact that electrons do not move independently and includes the exchange-correlation hole in the density of electrons of the same spin. The above equation is essentially an expression for the total energy of the noninteracting electron gas affected by an external potential $U_{xc}[\rho] + U_{lattice}[\rho]$, which includes both lattice and many-body effects.

In 1965 Kohn and Sham [52] described how to use the above expression to find the ground state electron density. The fact that the total energy of the interacting system can be mapped to the one of a noninteracting system moving in the effective potential $\hat{U}_H + \hat{U}_{xc} + \hat{U}_{lattice}$ means that this noninteracting system generates exactly the same electron ground state density as the interacting one. Starting from the Hamiltonian

$$\begin{aligned}\hat{H}_{KS} &= \hat{T}_0 + \hat{U}_H + \hat{U}_{xc} + \hat{U}_{lattice} \\ &= \frac{\hbar^2 \nabla^2}{2m_e} + \frac{e^2}{4\pi\epsilon_0} \int \frac{\rho(\mathbf{r}')}{|\mathbf{r} - \mathbf{r}'|} d\mathbf{r}' + \hat{U}_{xc} + \hat{U}_{lattice},\end{aligned}\tag{3.15}$$

the wave functions of the noninteracting system are the n lowest-energy solutions of the Kohn-Sham equation

$$\hat{H}_{KS} |\phi_i\rangle = \epsilon_i |\phi_i\rangle\tag{3.16}$$

and the electron ground state density is simply given by

$$\rho_{KS}(\mathbf{r}) = \sum_i |\phi_i\rangle \langle \phi_i|.\tag{3.17}$$

the Kohn-Sham density $\rho_{KS}(\mathbf{r})$ is equal to the ground state electron density. However, ϕ_i and ϵ_i do not describe real electrons but are the eigenfunctions and eigenenergies of the Kohn-Sham particles that have no direct physical meaning.

Because U_H and U_{xc} depend on $\rho(\mathbf{r})$ and $\rho(\mathbf{r})$ itself is given by ϕ_i , which itself depends on U_H and U_{xc} , equation 3.16 has to be solved iteratively. One has to first postulate some $\rho(\mathbf{r})$ then calculate U_H and U_{xc} for that $\rho(\mathbf{r})$, and finally solve equation 3.16 to find ϕ_i . From ϕ_i a new $\rho(\mathbf{r})$ can be calculated and compared to the initial one. If they are the same the self-consistency is achieved. If not, one has to repeat the cycle using a new $\rho(\mathbf{r})$ until self-consistency is reached.

Besides the Bohr-Oppenheimer approximation, density functional theory is exact. However, the exchange-correlation functional is impossible to calculate in the general case of an interacting many-body system and thus U_{xc} has to be approximated. To this end, Kohn and Sham introduced the so called local density approximation in which the exchange-correlation energy is given by

$$U_{xc}^{LDA} = \int \rho(\mathbf{r}) \epsilon(\rho(\mathbf{r})) d\mathbf{r},\tag{3.18}$$

where $\epsilon(\rho)$ is the exchange-correlation energy of a homogeneous interacting electron gas with density $\rho(\mathbf{r})$. Hence, U_{xc} depends only on the local value of the electron density

which implies that the approximation is best suited for systems in which the electron density varies slowly in space. For systems in which ρ has a strong spacial dependence the LDA can be improved by calculating an exchange-correlation potential depending not on the local value but on the local gradient of the electron density which is usually called Generalized Gradient Approximation (GGA).

Both methods, however, approximate the many-particle system by a one-electron approach where the electron moves in the mean-field created by the ions and all other electrons.

In order to solve the Kohn-Sham equation 3.16 one needs to find the wavefunctions $\phi_i(\mathbf{r})$. The one-electron wavefunction can be expressed as a linear combination of the complete set $\phi_i(\mathbf{r})$ of basis functions:

$$|\psi_i\rangle = \sum_{n=0}^{\infty} c_n^i |\phi_n\rangle, \quad (3.19)$$

where c_n^i are the coefficients to be found. The Kohn-Sham equation is then a system of linear algebraic equations, which can be solved by diagonalizing the Hamiltonian matrix. The complete basis set contains an infinite number of wavefunctions which renders the Kohn-Sham equations computationally impossible to solve. Therefore in practice a finite set is used, which introduces an error because the wavefunction is no longer exact. This error can be minimized by a careful choice of the basis.

Two general approaches to the basis set problem are the pseudopotential method and the linearized augmented plane wave method (LAPW). The planewave method is based on the assumption that the all physical properties of solids are determined by the valence electrons. Thus the divergent part of the potential close to the atom core is replaced by a smooth pseudopotential. For the potential that is now smooth everywhere, planewaves are a good basis. It is clear, however, that the result will depend on the way the pseudopotential was chosen.

The LAPW method combines plane waves and atomic like orbitals to describe the wave function. The basis set is given by

$$|\phi_n\rangle = \begin{cases} \sum_{lm} a_{lm} R_l(|\mathbf{r}|, R) Y_{lm}(\mathbf{r}), & \text{if } |\mathbf{r}| < S, \\ C e^{\mathbf{G}\cdot\mathbf{r}}, & \text{if } |\mathbf{r}| > S, \end{cases} \quad (3.20)$$

where $R_l(|\mathbf{r}|, R) Y_{lm}(\mathbf{r})$ is a solution of the Kohn-Sham equation for a spherically symmetric potential and a_{lm} are parameters to be determined. S is the muffin tin sphere, inside which electrons are described by atomic like orbitals, and outside of which they are best described by plane waves.

There are a number of commercial packages available which solve the Kohn-Sham equation using one of above methods. The results presented in this work were obtained with the WIEN2k code [53] which uses LAPW basis functions.

3.4 Spin-Orbit Coupling in Solids

Spin-orbit interaction leads to a lifting of the degeneracy of one-electron levels in atoms, molecules and solids. However, in crystals it can only slightly change the energies of atomic orbitals and in general does not influence the band degeneracy. As we will show in section 3.5.1 and 3.6.1 the spin-orbit interaction can be thought of as an additional on site hybridisation parameter that leads to orbital mixing which otherwise would be prevented by the crystal symmetry. Here we will concentrate on the origin of the spin-orbit interaction and we will derive an exact term that can later be included into our tight binding model.

Spin-orbit coupling is a consequence of the electron motion in an electric field. The standard solution of the non relativistic Schrödinger equation gives doubly degenerate levels as the electronic spin is completely neglected. The degeneracy can be lifted by including the interaction between the spin of the valance electron and the electric field generated by the ions. To this end the Schrödinger equation must be extended to include relativistic corrections to the energy of the electron. The basic equation that includes the electron spin and its relativistic behavior is called the Dirac equation

$$\left(\frac{1}{2m} \left(\mathbf{p} - \frac{e}{c} \mathbf{A} \right)^2 + e\phi - \frac{e\hbar}{2mc} \boldsymbol{\sigma} \cdot \mathbf{B} + i \frac{e\hbar}{4m^2c^2} \mathbf{E} \cdot \mathbf{p} - \frac{e\hbar}{4m^2c^2} \boldsymbol{\sigma} \cdot (\mathbf{E} \times \mathbf{p}) \right) \psi = W\psi. \quad (3.21)$$

It is valid for electrons with kinetic and potential energies small compared to mc^2 . $W+mc^2$ is the total energy, \mathbf{p} is the momentum operator, ϕ and A are the electric and magnetic potentials. The first two terms in brackets are equivalent to those in the Schrödinger equation for external fields. The third term corresponds to the interaction energy $-\boldsymbol{\mu} \cdot \mathbf{B}$ of the magnetic dipole, whose moment is presented by the operator $\boldsymbol{\mu} = \frac{e\hbar}{2mc} \boldsymbol{\sigma} = \frac{e}{mc} \mathbf{s}$. The fourth term is a relativistic correction to the energy and does not have a classical analogy. The last term describes the spin-orbit coupling.

In the case of centrally symmetric electric fields such as the orbital motion of an electron in the electric field of an atomic nucleus:

$$\mathbf{E} = -\frac{1}{e} \frac{\mathbf{r} dV}{r dr}, \quad (3.22)$$

and the spin-orbit term can be written in the form ($\mathbf{s} = \frac{\hbar}{2} \boldsymbol{\sigma}$)

$$-\frac{e\hbar}{4m^2c^2} \boldsymbol{\sigma} \cdot (\mathbf{E} \times \mathbf{p}) = \frac{e}{2m^2c^2} \mathbf{s} \cdot \left(-\frac{1}{e} \frac{\mathbf{r} dV}{r dr} \times \mathbf{p} \right) = \frac{1}{2m^2c^2} \frac{1}{r} \frac{dV}{dr} (\mathbf{s} \cdot \mathbf{l}). \quad (3.23)$$

The above equation results from the interaction of the spin with the electric field that is experienced by a relativistic electron. The strength of the interaction is given by the spin-orbit coupling parameter ξ :

$$\xi = \frac{1}{2m^2c^2} \frac{1}{r} \frac{dV}{dr}. \quad (3.24)$$

In a free atom, the spin-orbit interaction can lift the degeneracy of states with the same orbital wave function but with opposite spins. In solids such a splitting can be forbidden due to the crystal symmetry. Symmetry always preserves the Kramer's degeneracy

between a function $\psi(r, s)$ and its complex conjugate $\psi^*(r, s)$. ψ^* differs from ψ through a simultaneous reversal of wave vector and electron spin. Therefore, at any point of the BZ, one can write

$$E(\mathbf{k}, \uparrow) = E(-\mathbf{k}, \downarrow). \quad (3.25)$$

The Kramer's degeneracy remains unaffected when including the spin-orbit coupling term in the Hamiltonian (\uparrow and \downarrow corresponds to the two quantum numbers denoting eigenstates for a given Bloch vector). If the crystal lattice has inversion symmetry, then

$$E(\mathbf{k}, \uparrow) = E(-\mathbf{k}, \uparrow), \quad E(\mathbf{k}, \downarrow) = E(-\mathbf{k}, \downarrow). \quad (3.26)$$

Combining equations (3.25) and eq. (3.26) we find that the band structure has to satisfy

$$E(\mathbf{k}, \uparrow) = E(\mathbf{k}, \downarrow). \quad (3.27)$$

Hence the energy does not depend on the electron spin. In crystals without inversion symmetry, like GaAs (that crystalizes in the zincblende structure) spin-orbit interaction splits the valance bands for all \mathbf{k} vectors and in metals it leads to a spin splitting of the surface states – the so called Rashba effect. However, for crystals with inversion symmetry a spin splitting is not allowed (beside singular points in the BZ, e.g. Γ), and those solids keep their spin degeneracy.

3.5 DFT Results

The DFT band structure calculations reported in this thesis were performed using the WIEN2k package [53] which is based on the LAPW method. The precision of LAPW calculations depends on two parameters; the cutoff RK_{max} (R is the smallest muffin-tin radius and K_{max} is the magnitude of the largest \mathbf{k} vector) and the number of k -points in the first Brillouin zone. The only input to the LDA calculations is the crystal structure. For all our studies we used the structural data from [54] with $a = 3.86 \text{ \AA}$ and $c = 12.72 \text{ \AA}$.

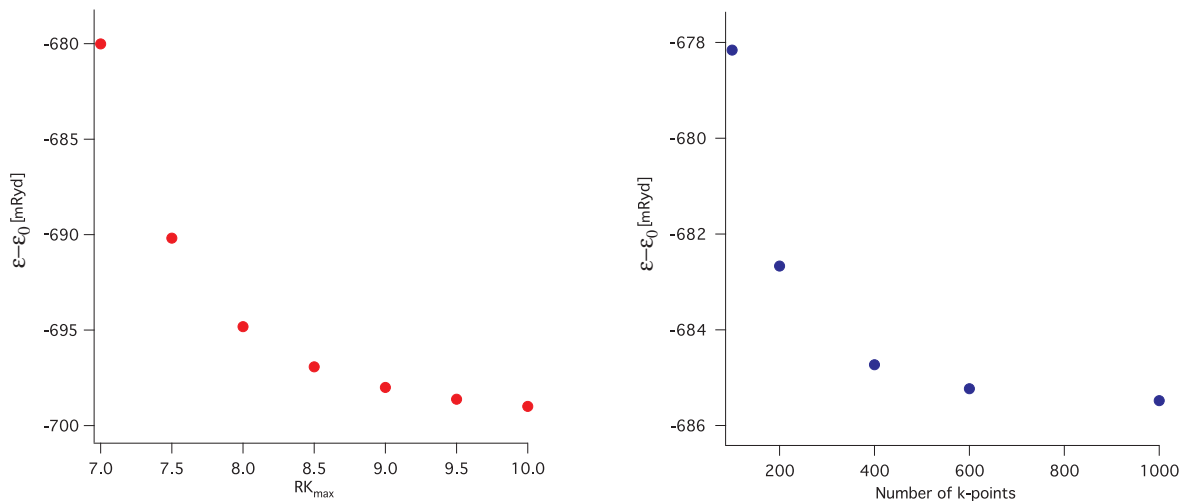


Figure 3.2: Total Energy optimization for (a) RK_{max} and (b) number of k -points. $\epsilon_0 = 22385 \text{ Ryd}$. $RK_{max} = 9.0$ and 500 k -points were chosen for the band structure calculations for Sr₂RuO₄.

In order to find the optimal parameters the total energy was calculated as a function of RK_{max} and number of k -points. The results are presented in figure 3.2. $RK_{max} = 9.0$ and 500 k -points were chosen for the band structure calculations. The muffin-tin radii were set to $2.4 a_0$ for Ru, $1.9 a_0$ for O and $2.1 a_0$ for Sr.

The calculations, using above parameters, reported in this thesis are in good agreement with less detailed previous studies [14, 55]. The Fermi surface consists of two electron-like (γ , β) and one hole-like pocket (α) as shown in figure 3.3. The dominant orbital character calculated from partial charges are color coded. The strongly anisotropic α and β pockets originate from hybridised out-of-plane orbitals d_{xz} and d_{yz} (blue), while the circular γ pocket is created by the in-plane d_{xy} orbitals (red). Because Sr_2RuO_4 is strongly layered, the three dimensional Fermi surface consists of slightly warped cylinders. Although the warping is small, it is sufficient to cause the crossing of the α and β sheets for $k_z \approx 0.25$. More details of the k_z dispersion will be given in Chapter 5.

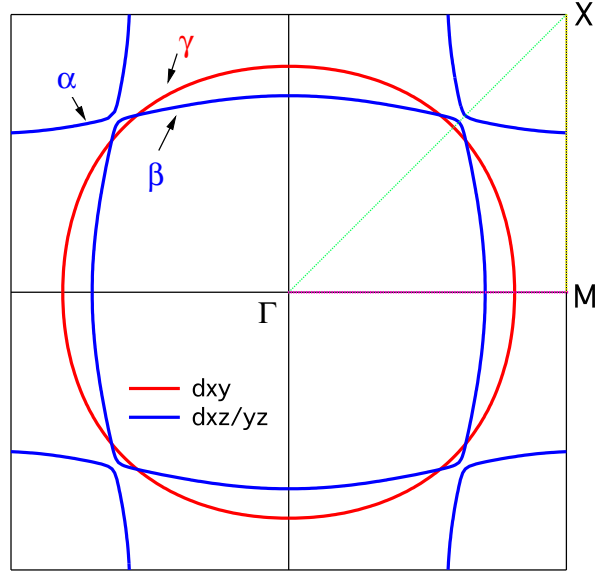


Figure 3.3: LDA Fermi surface of Sr_2RuO_4 for $k_z = 0$. The hole-like α and electron-like β sheet with $d_{xz/yz}$ orbital character is shown in blue, while the electron-like γ deriving from the d_{xy} orbital is shown in red.

Figure 3.4 shows the band structure calculated along the high symmetry directions denoted by colored lines in figure 3.3. Along the ΓX direction, the γ sheet crosses β and α . However, no gap is opened because the d_{xy} and $d_{xz/yz}$ orbitals are orthogonal in the tetragonal environment. The same effect is visible on the Fermi surface where β and γ sheets intersect.

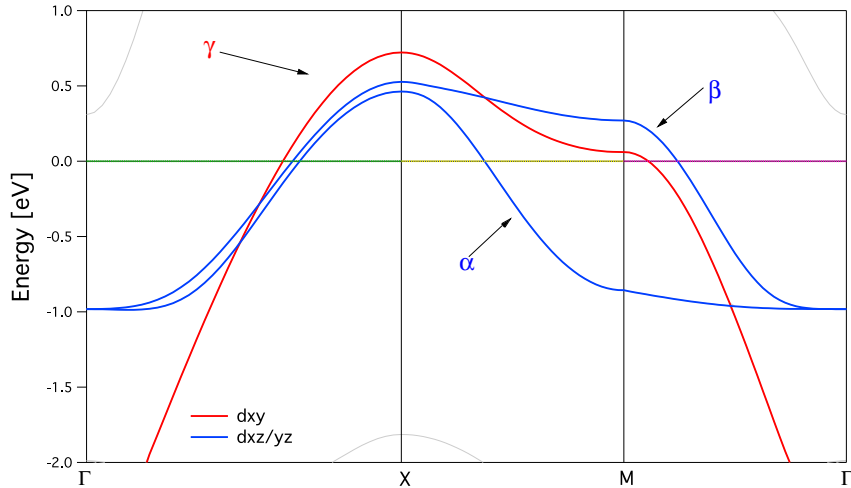


Figure 3.4: Band structure of Sr_2RuO_4 along high symmetry directions.

3.5.1 DFT + SOC

Spin-orbit coupling leads to a mixing of orbitals, which has strong consequences for the band structure. In the case of Sr_2RuO_4 , Haverkort *et al.* [55] showed that the inclusion of SOC improves the agreement between LDA and ARPES Fermi surfaces and strongly reduces the k_z dependence of the β and α bands. The WIEN2k package offers the possibility to include spin-orbit coupling in the calculation using the second variational method with scalar relativistic orbitals as a basis [56, 57]. The local density approximation is extended to the local spin density approximation (LSDA) and calculations are carried out for two species of spin. This removes the crossing between the β and γ pockets on the Fermi surface (figure 3.5 (a) and (b)) and opens a gap where any of three bands cross (see figure 3.6).

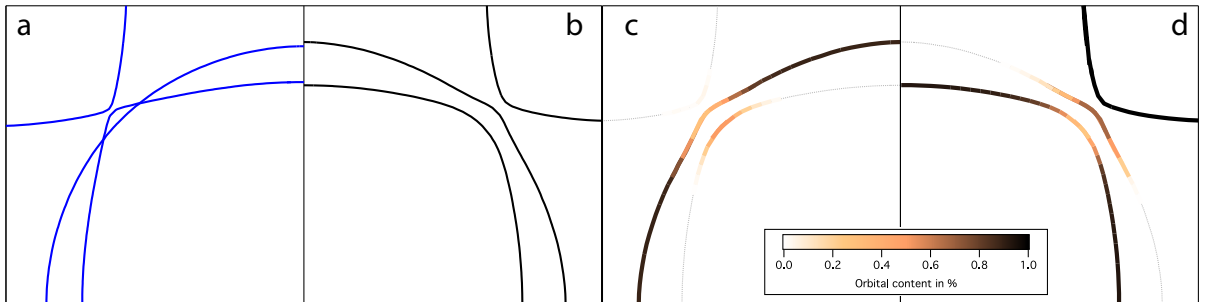


Figure 3.5: Fermi surface of Sr_2RuO_4 : (a) plain LDA calculation reproduced from figure 3.3, (b) LSDA + SOC Fermi surface showing the avoided crossing between the β and γ bands. (c) d_{xy} orbital content and (d) $d_{xz/yz}$ orbital content.

SOC opens a gap of 91 meV between the α and β bands at the Γ point and lifts all degeneracies along the ΓX and XM directions. Additionally, SOC leads to mixing of the orbital character at points where a crossing is removed. At the Fermi surface the mixing is particularly high for the β and γ bands (see figure 3.5 (c) and (d)). For the α pocket

on the other hand, which crosses the γ sheet 0.5 eV below the Fermi level, the mixing is negligible.

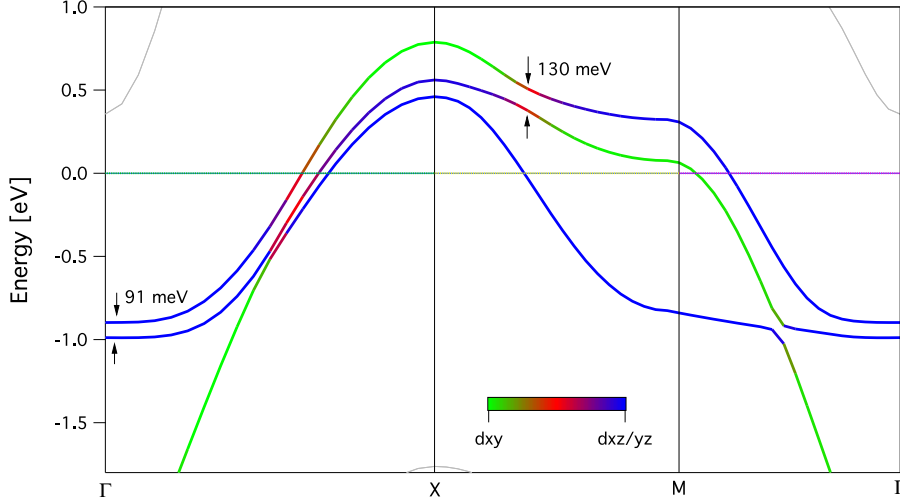


Figure 3.6: LDA+SOC band structure of Sr_2RuO_4 along high symmetry directions. Colors denotes band orbital character with the scale given in the inset.

This orbital mixing can have a strong influence on the many-body interactions and their momentum dependence. In particular in chapters 3.6.2 and 4.3 we will show how SOC can result in a momentum dependent Zeeman splitting and momentum dependent mass renormalization.

3.6 TB Results

Ruthenium has eight electrons in the valance shell and its ground state configuration is $4d^75s^1$. For Strontium and Oxygen in their usual valencies of +2 and -2, respectively, this leaves four electrons on the Ruthenium $4d$ -shell. In an octahedral environment the five $4d$ levels split into two subsets, a low energy t_{2g} representation with d_{xy} , d_{xz} and d_{yz} orbitals which can accommodate 6 electrons and a high energy e_g representation with the $d_{x^2-y^2}$ and $d_{z^2-3z^2}$ orbitals (see figure 3.7). Because in Sr_2RuO_4 the crystal field splitting is much higher than Hund's coupling the four valance electrons are distributed over three t_{2g} levels.

This means that the tight-binding wave function can be constructed from a linear combination of the wave functions $|\phi_{xy}\rangle$, $|\phi_{xz}\rangle$ and $|\phi_{yz}\rangle$ of the d_{xy} , d_{xz} , d_{yz} orbitals. We assume the overlap matrix to be $S_{ij} = 1$. The full Hamiltonian for Sr_2RuO_4 can then be written as

$$H = \begin{pmatrix} H_{xy} & H_{xy/yz} & H_{xy/xz} \\ H_{yz/xy} & H_{yz} & H_{yz/xz} \\ H_{xz/xy} & H_{xz/yz} & H_{xz} \end{pmatrix}. \quad (3.28)$$

Using the wave functions in the form 3.6, and including interactions only up to 2nd

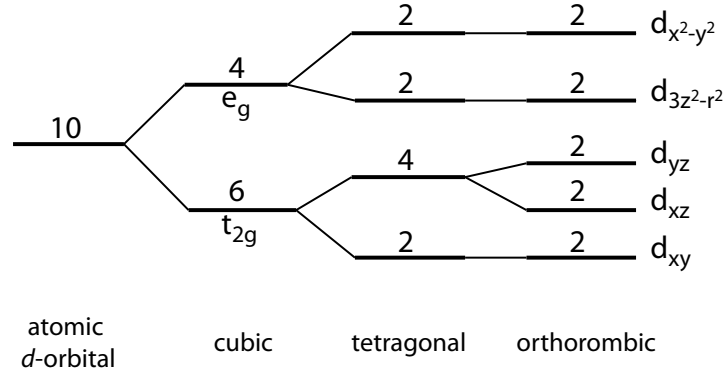


Figure 3.7: Energy level diagram of d -atomic orbitals in different crystal environments. In cubic crystals the 10 degenerate electron levels split into two subsets: low-energy t_{2g} and high-energy e_g states. The reduced symmetry of the tetragonal and orthorhombic environment splits them further into five spin degenerate levels – d_{xy} , d_{xz} , d_{yz} , $d_{3z^2-r^2}$ and $d_{x^2-y^2}$.

nearest neighbours the transfer matrix for the d_{xy} orbital is given by

$$\begin{aligned}
 H_{xy} &= \frac{1}{N} \sum_{\mathbf{R}, \mathbf{R}'} e^{i\mathbf{k}(\mathbf{R}-\mathbf{R}')} \langle \varphi_{xy}(\mathbf{r}-\mathbf{R}') | H | \varphi_{xy}(\mathbf{r}-\mathbf{R}) \rangle \\
 &= \epsilon_{xy} + 2t_{1xy} \left(\cos\left(\frac{k_x a}{2}\right) + \cos\left(\frac{k_y a}{2}\right) \right) + 4t_{2xy} \left(\cos\left(\frac{k_x a}{2}\right) \cos\left(\frac{k_y a}{2}\right) \right),
 \end{aligned} \tag{3.29}$$

where ϵ_{xy} is the energy of the atomic orbital d_{xy} . The hopping parameters are $t_{1xy} = \langle \varphi_{1xy} | H | \varphi_{1xy} \rangle$, $t_{2xy} = \langle \varphi_{2xy} | H | \varphi_{2xy} \rangle$ for the 1st and 2nd neighbours respectively. The d_{xy} orbitals overlap strongly for both in-plane nearest neighbours directions and along the lattice diagonal (see figure 3.8 (a)) which results in an almost circular d_{xy} pocket at the Fermi surface.

Because $d_{xz/yz}$ and d_{xy} are orthogonal they do not hybridise, and $H_{xy/yz} = H_{yz/xy} = H_{xy/xz} = H_{xz/xy} = 0$.

For the d_{xz} orbital extended in the x direction, one can expect a strong overlap only for neighbours along the x axis (see figure 3.8 (b)). Similarly, for the d_{yz} orbitals, which are elongated along the y direction, strong overlap can be expected only for neighbours along the y axis. The transfer matrices for these orbitals are given by

$$\begin{aligned}
 H_{xz} &= \frac{1}{N} \sum_{\mathbf{R}, \mathbf{R}'} e^{i\mathbf{k}(\mathbf{R}-\mathbf{R}')} \langle \varphi_{xz}(\mathbf{r}-\mathbf{R}') | H | \varphi_{xz}(\mathbf{r}-\mathbf{R}) \rangle \\
 &= \epsilon_{xz} + 2t_{1xz} \cos\left(\frac{k_x a}{2}\right) + 2t_{1'xz} \cos\left(\frac{k_y a}{2}\right) \\
 &\quad + 4t_{2xz} \left(\cos\left(\frac{k_x a}{2}\right) \cos\left(\frac{k_y a}{2}\right) \right) + 8t_{zxx} \left(\cos\left(\frac{k_x a}{2}\right) \cos\left(\frac{k_y a}{2}\right) \cos\left(\frac{k_z c}{2}\right) \right)
 \end{aligned} \tag{3.30}$$

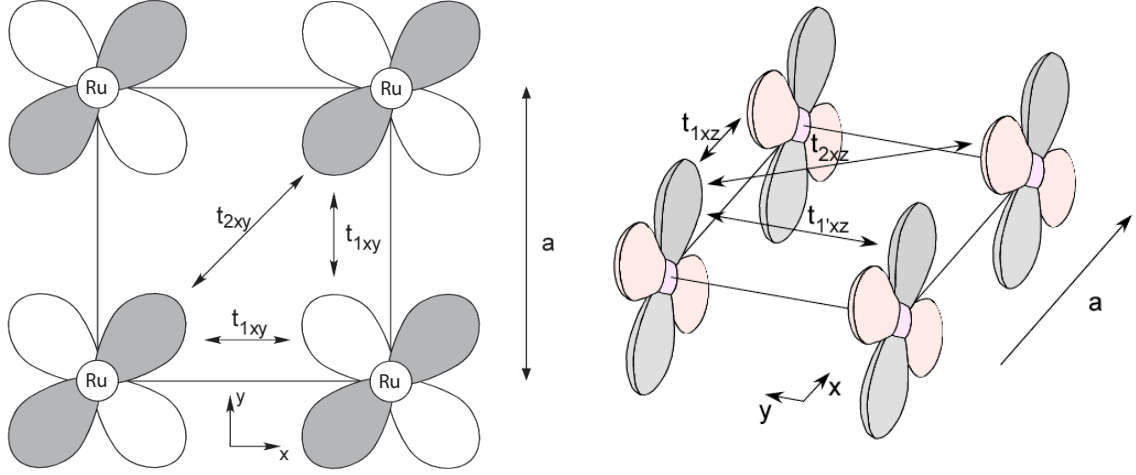


Figure 3.8: Hopping parameters for (a) d_{xy} orbitals and (b) $d_{xz/yz}$ orbitals.

and

$$\begin{aligned}
H_{yz} &= \frac{1}{N} \sum_{\vec{R}, \vec{R}'} e^{i\vec{k}(\vec{R}-\vec{R}')} \langle \varphi_{yz}(\vec{r}-\vec{R}') | H | \varphi_{yz}(\vec{r}-\vec{R}) \rangle \\
&= \epsilon_{yz} + 2t_{1yz} \cos\left(\frac{k_y a}{2}\right) + 2t_{1'yz} \cos\left(\frac{k_x a}{2}\right) \\
&\quad + 4t_{2yz} \left(\cos\left(\frac{k_x a}{2}\right) \cos\left(\frac{k_y a}{2}\right) \right) + 8t_{zyz} \left(\cos\left(\frac{k_x a}{2}\right) \cos\left(\frac{k_y a}{2}\right) \cos\left(\frac{k_z c}{2}\right) \right),
\end{aligned} \tag{3.31}$$

where $\epsilon_{xz/yz}$ is the energy of the atomic orbital $d_{xz/yz}$, $t_{1xz/yz}$ is the hopping parameter for nearest neighbours in the direction of strong overlap and $t_{1'xz/yz}$ is the hopping parameter for nearest neighbours in the direction perpendicular to the orbital in-plane axis ($t_{1xz/yz} \gg t_{1'xz/yz}$). $t_{2xz/yz}$ is the hopping parameter for the next nearest neighbours and $t_{zxz/yz}$ is the largest hopping parameter along z -axis. Because of strong one-dimensional character of $d_{xz/yz}$ orbitals one can expect quasi-one dimensional bands. Because d_{xz} and d_{yz} orbitals can hybridise for $k_x, k_y \neq 0$ they create two almost square pockets – the α and β sheets. The hybridisation is given by:

$$H_{xz/yz} = 4t_{xz/yz} \cos\left(\frac{k_x a}{2}\right) \cos\left(\frac{k_y a}{2}\right) + 8t'_{zxx/zyy} \sin\left(\frac{k_x a}{2}\right) \sin\left(\frac{k_y a}{2}\right) \cos\left(\frac{k_z c}{2}\right), \tag{3.32}$$

where $t_{xz/yz}$ is the hybridisation parameter between d_{xz} and d_{yz} orbitals in RuO_2 plane, $t'_{zxx/zyy}$ is the hybridisation between d_{xz} and d_{yz} in different RuO_2 planes and $H_{yz/zx} = H_{xz/yz}^*$.

The parameters were fitted to give the best match to the LDA Fermi surface presented in section 3.5. The results are shown in figure 3.9. Red lines denote the tight binding bands and the black dots give the position of Fermi level crossing in LDA.

The orbital energies and hopping parameters are summarised in table 3.1.

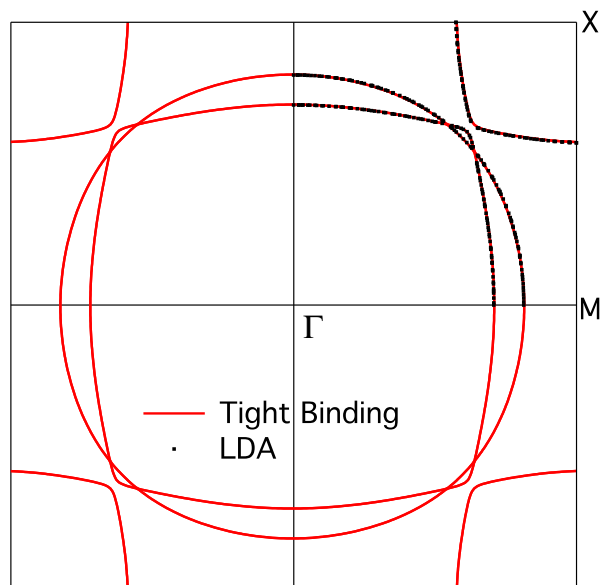


Figure 3.9: Tight binding Fermi surface of Sr_2RuO_4 fitted to the LDA calculation. Red line - tight binding bands, black dots - LDA Fermi surface.

	$t_i(0)$	$t_{ii}(a,0,0)$	$t_{ii}(0,a,0)$	$t_{ii}(a,a,0)$	$t_{ii}(\frac{a}{2}, \frac{a}{2}, c)$	$t_{i2}(a,a,0)$	$t_{i3}(a,a,0)$	$t_{i2}(\frac{a}{2}, \frac{a}{2}, c)$	$t_{i3}(\frac{a}{2}, \frac{a}{2}, c)$
d_{xy}	0.42	0.385	0.385	0.157	-	-	-	-	-
d_{xz}	0.275	0.315	0.062	0.014	0.01	-	0.01	-	0.001
d_{yz}	0.275	0.315	0.062	0.014	0.01	0.01	-	0.001	-

Table 3.1: Summary of tight binding parameters. Three orbital are denoted as $i = 1, 2, 3$ with $1 = d_{xy}$, $2 = d_{xz}$ and $3 = d_{yz}$.

3.6.1 Tight binding with SOC

The tight binding Hamiltonian including spin-orbit interaction has the form

$$H = H_0 + H_{SOC}, \quad (3.33)$$

where H_0 is a standard TB Hamiltonian (equation 3.28) and H_{SOC} describes the spin-orbit interaction and is given by

$$H_{SOC} = \xi (\mathbf{s} \cdot \mathbf{l}), \quad (3.34)$$

where ξ is the spin-orbit coupling parameter $\xi = \frac{1}{2m^2c^2} \frac{1}{r} \frac{dV}{dr}$ introduced in equation 3.23.

Using Pauli matrices for the spin operator the spin-orbit Hamiltonian can be expressed by

$$H_{SOC} = \frac{\xi}{2} (\sigma_x L_x + \sigma_y L_y + \sigma_z L_z), \quad (3.35)$$

where

$$\mathbf{s} = (\sigma_x, \sigma_y, \sigma_z) = \left(\left(\begin{array}{cc} 0 & 1 \\ 1 & 0 \end{array} \right), \left(\begin{array}{cc} 0 & -i \\ i & 0 \end{array} \right), \left(\begin{array}{cc} 1 & 0 \\ 0 & -1 \end{array} \right) \right). \quad (3.36)$$

In the spin representation the full Hamiltonian can then be written as:

$$H = \begin{pmatrix} H^{\uparrow\uparrow} & H^{\uparrow\downarrow} \\ H^{\downarrow\uparrow} & H^{\downarrow\downarrow} \end{pmatrix} = \begin{pmatrix} H_0 + \frac{\xi}{2} L_z & \frac{\xi}{2} (L_x - iL_y) \\ \frac{\xi}{2} (L_x + iL_y) & H_0 - \frac{\xi}{2} L_z \end{pmatrix}. \quad (3.37)$$

Introducing lowering and raising operators for the angular momentum:

$$L^{+/-} = L_x \pm iL_y, \quad (3.38)$$

the SO Hamiltonian is given by

$$H = \begin{pmatrix} H_0 + \frac{\xi}{2} L_z & \frac{\xi}{2} L^+ \\ \frac{\xi}{2} L^- & H_0 - \frac{\xi}{2} L_z \end{pmatrix}. \quad (3.39)$$

The size of the original Hamiltonian matrix doubled due to the separation for spin up and spin down bands. Using eigenvalues of the angular momentum operators the matrix elements for the six d -orbital atomic wave functions given by:

$$\begin{aligned} |d_{xy}^{\uparrow\downarrow}\rangle &= \sqrt{\frac{5}{16\pi}} xy \frac{1}{r^2} |\uparrow\downarrow\rangle, \\ |d_{yz}^{\uparrow\downarrow}\rangle &= 2\sqrt{\frac{15}{16\pi}} yz \frac{1}{r^2} |\uparrow\downarrow\rangle, \\ |d_{xz}^{\uparrow\downarrow}\rangle &= 2\sqrt{\frac{15}{16\pi}} xz \frac{1}{r^2} |\uparrow\downarrow\rangle, \end{aligned} \quad (3.40)$$

are

$$\langle d \uparrow | H_{SOC} | d \uparrow \rangle = \begin{pmatrix} 0 & 0 & 0 \\ 0 & 0 & i\frac{\xi}{2} \\ 0 & -i\frac{\xi}{2} & 0 \end{pmatrix}, \quad (3.41)$$

$$\langle d \uparrow | H_{SOC} | d \downarrow \rangle = \begin{pmatrix} 0 & \frac{\xi}{2} & -i\frac{\xi}{2} \\ -\frac{\xi}{2} & 0 & 0 \\ i\frac{\xi}{2} & 0 & 0 \end{pmatrix}, \quad (3.42)$$

and $\langle d \downarrow | H_{SOC} | d \downarrow \rangle = (\langle d \uparrow | H_{SOC} | d \uparrow \rangle)^*$, $\langle d \downarrow | H_{SOC} | d \uparrow \rangle = -(\langle d \uparrow | H_{SOC} | d \downarrow \rangle)^*$.

Hence, the full (6×6) TB Hamiltonian is given by:

$$H = \begin{pmatrix} H_{xy} & 0 & 0 & 0 & \frac{\xi}{2} & -i\frac{\xi}{2} \\ 0 & H_{yz} & H_{yz/xz} + i\frac{\xi}{2} & -\frac{\xi}{2} & 0 & 0 \\ 0 & H_{xz/yz} - i\frac{\xi}{2} & H_{xz} & i\frac{\xi}{2} & 0 & 0 \\ 0 & -\frac{\xi}{2} & -i\frac{\xi}{2} & H_{xy} & 0 & 0 \\ \frac{\xi}{2} & 0 & 0 & 0 & H_{yz} & H_{yz/xz} - i\frac{\xi}{2} \\ i\frac{\xi}{2} & 0 & 0 & 0 & H_{xz/yz} + i\frac{\xi}{2} & H_{xz} \end{pmatrix}. \quad (3.43)$$

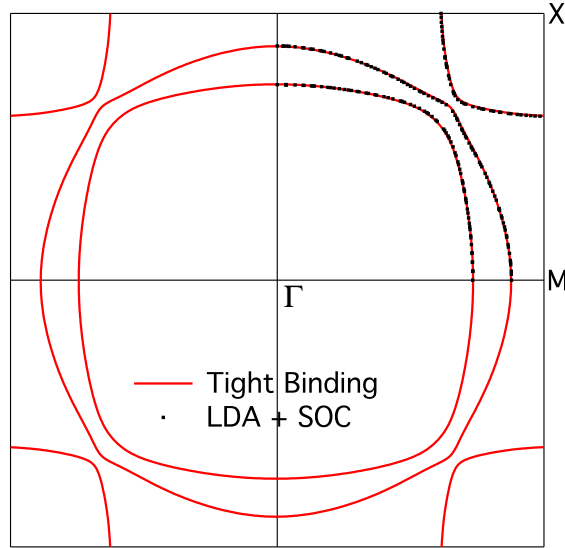


Figure 3.10: Tight binding + SOC Fermi surface of Sr_2RuO_4 fitted to LSDA+SOC results. Red line - tight binding bands, black dots - LSDA Fermi surface.

Figure 3.10 shows the result of fitting of the TB model to the LSDA+SOC Fermi surface. The strength $\xi = 75$ meV of the spin-orbit coupling was found by adjusting the size of the gap between β and γ sheets at the Fermi surface along the Brillouin zone diagonal to match the LSDA+SOC value.

3.6.2 Momentum dependent Zeeman splitting

Spin-orbit coupling in a multi-orbital system can lead to an anisotropic spin-splitting of the bands in a magnetic field. As reported by Bergemann *et al.* [58] such an effect is also

present in Sr_2RuO_4 . The behavior of the amplitude of the de Hass van Alphen signal [58] can only be explained assuming an anomalous spin-splitting for all three Fermi surface sheets (see figure 3.11). However, the exact value of the Zeeman splitting anisotropy could only be extracted for the α band and was found to be ~ 3 (in both $k_z = 0$ and $k_z = \frac{2\pi}{c}$, see figure 3.11).

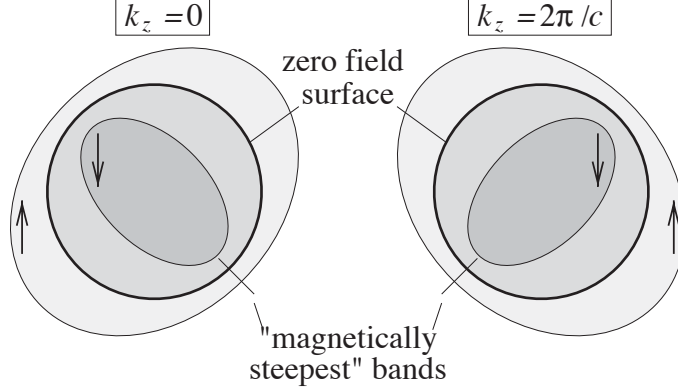


Figure 3.11: Sketch of the magnetic anisotropy of the α band. The inverse rate (magnetic v_F) at which the spin-up and spin-down pockets are driven apart by a magnetic field varies by a factor of three around the Fermi surface. Reproduced from [58].

In order to study this effect we use the tight binding model derived in section 3.6.1. To describe the band structure in a magnetic field we introduce a Zeeman term in the tight binding Hamiltonian:

$$H = H_0 + H_{SOC} + H_{Zeeman}. \quad (3.44)$$

For a magnetic field along the c -axis:

$$H_{Zeeman} = -\mu B, \quad (3.45)$$

where B is the magnetic field strength and μ is the magnetic moment. We define H_{Zeeman} as positive for spin down and negative for spin up.

One of the consequences of spin-orbit coupling on the Fermi surface of Sr_2RuO_4 is the mixed orbital character of the γ and β sheets. The mixing is closely related to the crossings of the β and γ pockets in the absence of spin-orbit coupling. As it was shown in section 3.6.1 spin-orbit coupling leads to nonzero matrix elements for d_{xy} and $d_{xz/yz}$ orbitals, which in turn opens a gap at points where these orbitals cross. Because the β and γ sheets cross right at the Fermi surface the opening of the spin-orbit gap leads to a slight modification of the shape of these two pockets and to a strong mixing of the orbital character. However, the spin-orbit interaction for d_{xy} and $d_{xz/yz}$ is nonzero only for opposite spins. This selective repulsion can lead to nodes in magnetically split γ and β bands (compare figures 3.12 (b) and (c)) generating a large \mathbf{k} -dependence of the Zeeman splitting. The exact value of the anisotropy depends on the SOC strength. In figure 3.12 we present the tight binding model in magnetic field for different values of SOC to show how the \mathbf{k} -dependence is created and how it depends on the strength of the SOC.

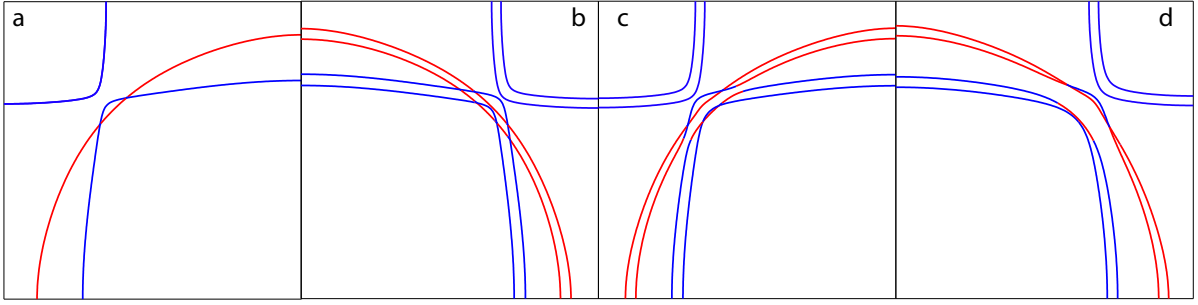


Figure 3.12: Momentum dependent Zeeman splitting. The Fermi surfaces are obtained for (a) $\xi = 0$ and $B = 0$, (b) $B = 26$ meV $\xi = 0$ (c) $B = 26$ meV and $\xi = 25$ meV, (d) $B = 26$ meV and $\xi = 75$ meV

Figure 3.12 (a) shows the Fermi surface without SOC and for $B = 0$. In panel (b) a magnetic field is introduced which results in a homogeneous splitting. Adding SOC (panel (c)) the avoided crossing between $\gamma \uparrow$ and $\beta \downarrow$ (and vice versa) generates a strongly \mathbf{k} -dependent Zeeman splitting with nodes on γ that persist even for high values of ξ (panel (d)). From this we can conclude that the effect is present whenever Fermi surface sheets “touch” or d_{xy} and $d_{xz/yz}$ bands cross at the Fermi level or its close vicinity. Note that the strong effect visible for the β and γ sheets is absent for α pocket for which we find a constant splitting over entire Brillouin zone. The crossing between α and β visible

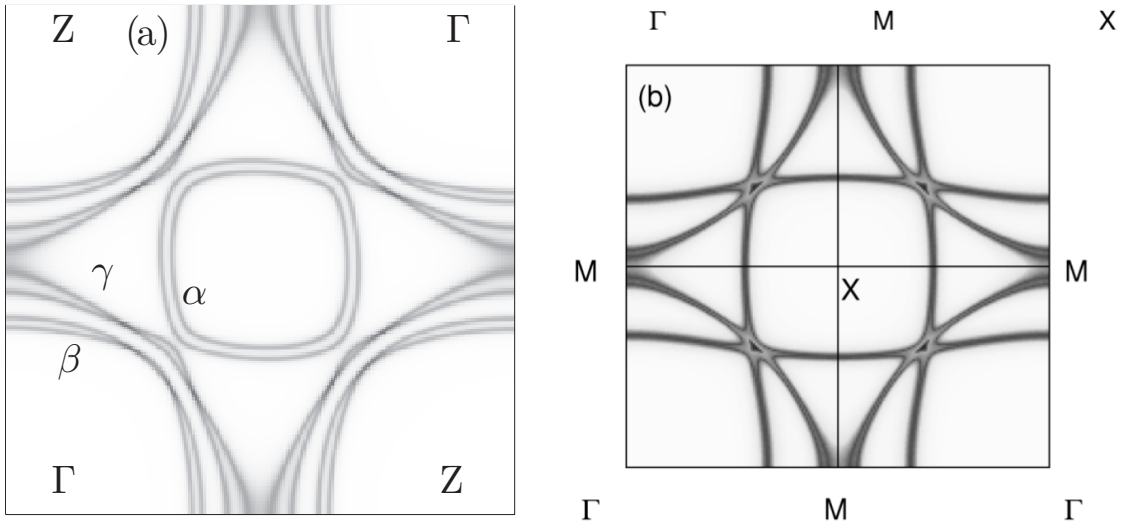


Figure 3.13: (a) LDA Bloch spectral function $A(\mathbf{k}, E_F)$ calculated using the fully relativistic Munich SPRKKR method [59]. (b) Fermi surface of Sr_2RuO_4 according to dynamical mean field theory by Liebsch and Lichtenstein [60]. Strong reduction in the width of $d_{xz/yz}$ bands generates the charge transfer to d_{xy} band generating crossing between α and γ bands.

in figure 3.12 (b) does not induce k -dependence because the mixing of d_{xz} and d_{yz} orbitals is allowed only for parallel spins. This result is consistent with Fermi surface calculations

with the fully relativistic KKR formalism that uses LDA result as an input. The results of such calculations from Ref. [59] are presented in figure 3.13 (a).

Neither the tight binding model nor the KKR formalism reproduce the experimental anisotropy of the Zeeman splitting for the α band. From the described mechanism of anisotropy for the β and γ sheets, we conclude that in order to match the experimental result for the α pocket, α and γ sheets have to cross or at least touch at some point along k_z . However, LDA calculations do not show such a crossing. This discrepancy might be explained by correlation induced charge transfer between the d_{xy} and $d_{xz/yz}$ bands as predicted by dynamical mean field theory (DMFT) calculations by Liebsch and Lichtenstein [60]. Strong correlations lead to a reduction of the width of $d_{xz/yz}$ bands, and, in order to satisfy the Luttinger theorem, spectral weight transfer to the d_{xy} band is required. This in turn can generate a crossing between the α and γ bands (see figure 3.13(b)).

To simulate the charge transfer required for a crossing between the α and β pocket, we increased the hopping parameters for the γ band, increasing its bandwidth and the pocket size at the FS, and decreased the hopping for $d_{xz/yz}$ orbitals increasing the size of the hole-like α sheet and decreasing the size of electron-like β band. Depending on the relative change of the parameters we can generate a touching or a crossing between the α and γ pockets. The results are presented in figure 3.14. The Zeeman splitting anisotropy

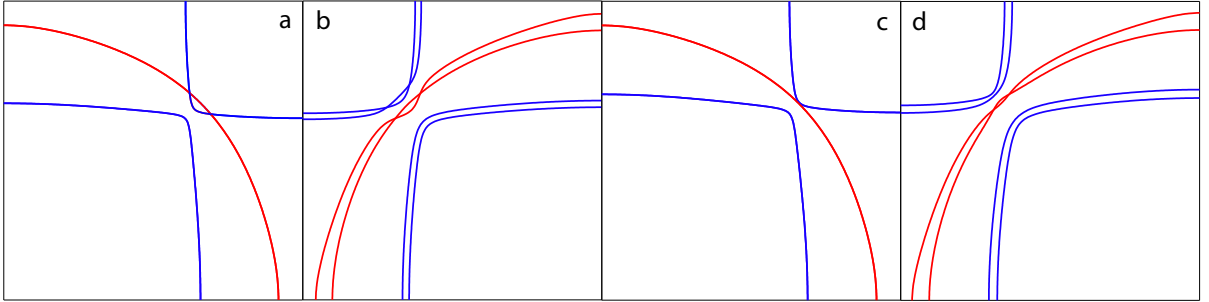


Figure 3.14: Momentum dependence of the Zeeman splitting for the α band for $\xi = 100$ meV and $B = 25$ meV in the case of: (a), (b) crossing between α and γ and (c), (d) “touching” of α and γ sheets.

for $\xi = 100$ meV and a such adjusted Fermi surface is a factor of 2, which is still smaller the experimental value of 3. We point out, however, that there is significant uncertainty in ξ and position of all three bands, which both influence the Zeeman splitting anisotropy. To resolve this issue further DMFT or ARPES measurements for different k_z are needed. And finally the dHvA values of the spin anisotropy for β and γ would certainly help in order to estimate the spin-orbit interaction strength more accurately.

Chapter 4

Results and Discussion

4.1 Surface layer band structure

We will start this chapter with a description of the Fermi surface and the band structure of the surface layer of Sr_2RuO_4 . In order to distinguish between bulk and surface contributions to the ARPES spectra we have revisited the high temperature cleaving procedure used by Damascelli *et al.* [17] to diminish the intensity of the surface bands. The results we are going to present are fully consistent with data published so far [17–19, 61–70] but show additional features in the spectra, which we ascribe to diffraction replica (DR) of the bulk bands.

The surface of Sr_2RuO_4 reconstructs in a $\sqrt{2} \times \sqrt{2}R45^\circ$ structure due to a rotation of the RuO_6 octahedra in the top layer by $6 - 9^\circ$ around the c -axis [71]. The structural differences between surface and bulk lead to two weakly coupled electronic subsystems, located in the topmost and in deeper RuO_2 planes, respectively. The most comprehensive study of the Fermi surface to date comes from Shen *et al.* [64]. By the comparison of the results of LDA calculations and ARPES spectra authors confirmed the existence of the surface and bulk subsystems.

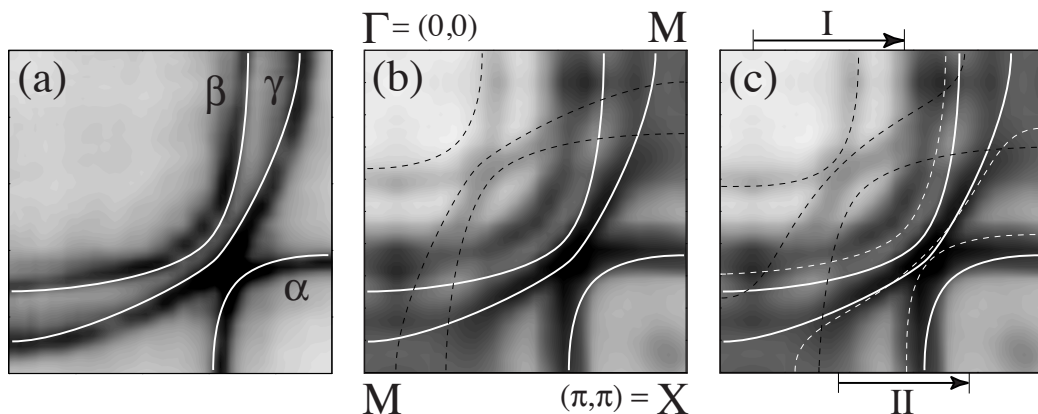


Figure 4.1: Fermi surface of Sr_2RuO_4 : (a) cleave at 180 K white lines LDA bands, (b) cleave at 10 K white lines LDA bulk bands, dashed lines - backfolded bulk bands, (c) solid white lines - LDA bulk bands, dashed white and black lines - surface and backfolded surface bands respectively. Figure reproduced from [64].

Moreover they described that by cleaving the sample at 180 K one can suppress the intensity of the surface bands (SB) enough to see only the bulk bands (BB) (figure 4.1 (a)).

We have revisited the high temperature cleaving procedure, by cleaving the samples at 5 K, 180 K and 300 K and pressures better then 4×10^{-11} mbar. However, none of these cleaves resulted in a significant suppression of the intensity of the surface bands. Only after exposing the cleaved samples for ~ 60 s to pressures in the range of 10^{-9} mbar in an un-baked load-lock we were able to diminish the intensity from the SB. The Fermi surface measured at $T = 5$ K and $p < 4 \times 10^{-11}$ mbar from a surface treated in this way is presented in figure 4.2 (a). Besides the bulk bands we observe three additional pockets translated by a reciprocal lattice vector of the reconstructed surface. They can be attributed to diffraction replica of the bulk bands. The existence of diffraction replica is consistent with LEED data [17] showing the persistence of a $\sqrt{2} \times \sqrt{2}$ reconstruction after cleaving at elevated temperature. The excellent agreement of the bulk band structure seen in ARPES with dHvA and band structure calculations indicates that DR are final state umklapps and not arise from a significant perturbation of the potential in deeper RuO_2 layers with the periodicity of the surface.

The complete Fermi surface of Sr_2RuO_4 , showed in figure 4.2 (b, c), is composed of: the bulk bands (blue contours, α , β and γ pockets fully consistent with dHvA and LDA), the surface bands (red contours) and the back-folded bulk bands (green contours).

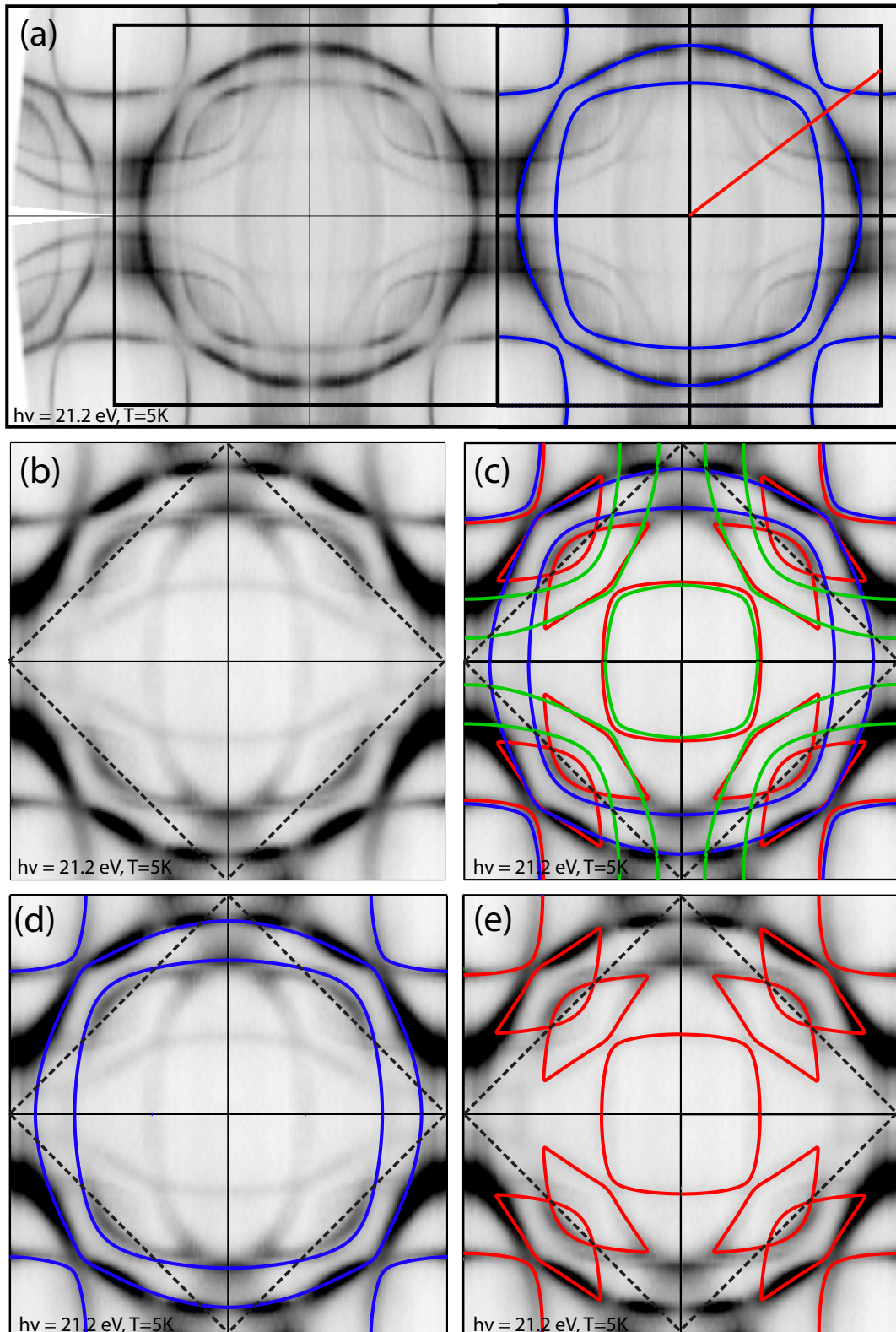


Figure 4.2: Fermi Surface of Sr₂RuO₄: (a) FS measured after room temperature cleave and $p < 1 \times 10^{-9}$ mbar, the blue contours indicate the TB FS, (b) FS measured after low temperature cleave and $p < 4 \times 10^{-11}$, (c) ARPES FS with TB surface layer bands (red), TB bulk bands (blue) and TB bulk DR bands (green), (d) FS with TB bulk bands only, (e) FS with TB surface bands only. Dashed line indicates SB Brillouin zone.

From an analysis of LEED IV curves, Matzdorf *et al.* [71] estimated a rotation angle of the surface octahedra of $\theta_{\Delta} \sim 6 - 9^{\circ}$. This is consistent with the value of $\theta_{\Delta} = 6^{\circ}$ for which Shen *et al.* reported the best match between LDA calculations for an artificially distorted bulk structure and their ARPES data [64]. Here we extended these calculations by studying a slab of Sr_2RuO_4 consisting of a single RuO_2 plane in-between two SrO_2 planes as illustrated in figure 4.3. The vacuum layer between two slabs was set to 6 Å and the calculations include spin-orbit interaction.

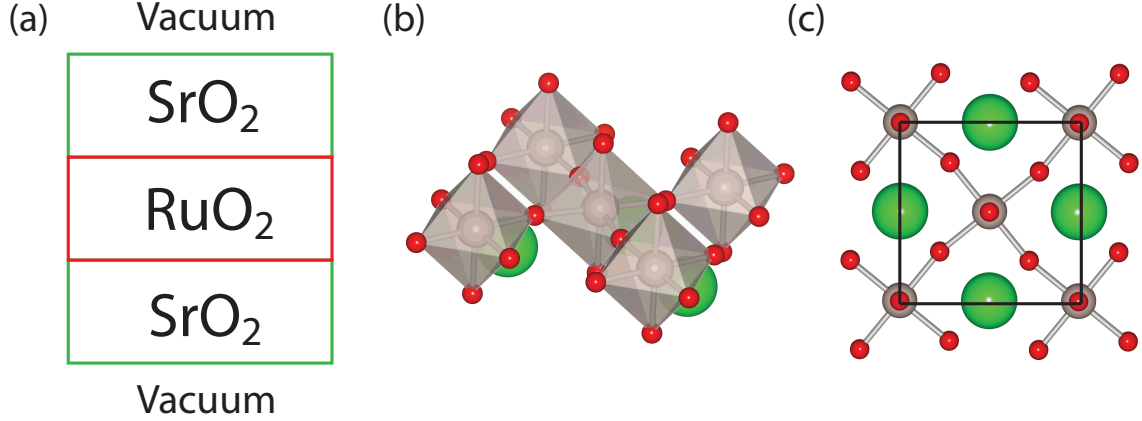


Figure 4.3: Slab used for the band structure calculations of the surface layer of Sr_2RuO_4 . (a) crystal plane stacking along the c direction in the slab, (b) single layer of RuO_6 octahedra with the Sr atoms removed for clarity, (c) the ab plane unit cell of the surface layer.

The results for different rotation angles $\theta_{\Delta} = 0 - 12^{\circ}$ are presented in figure 4.4. Due to the reduced hopping via apical O $p_{x/y}$ orbitals the bandwidth of the $d_{xz/yz}$ bands decreases from 1.8 eV in the bulk to 1.3 eV in the slab, whereas the d_{xy} bandwidth does not change from the bulk value of 3.6 eV. Due to rotation of the octahedra the d_{xy} and $d_{x^2-y^2}$ orbitals are no longer orthogonal and thus hybridise creating a new band with minima at the Γ and M points. The minimum at the M point acquires a strong $d_{x^2-y^2}$ character (green line in figure 4.4) whereas the minimum at the Γ point retains the d_{xy} character (red line in figure 4.4).

The rotation of the octahedra changes the bandwidth and the crystal field splitting of the d_{xy} and $d_{x^2-y^2}$ bands. This is clearly visible by comparison of the position of $d_{x^2-y^2}$ and d_{xy} minima relative to each other. For $\theta_{\Delta} = 0$, the $d_{x^2-y^2}$ minimum is 0.25 eV above the d_{xy} minimum, whereas for $\theta_{\Delta} = 12^{\circ}$ the situation changes by pushing the $d_{x^2-y^2}$ minimum 0.1 eV below the d_{xy} one. The octahedra rotation has a negligible influence on the $d_{xz/yz}$ bands because the dominant hoppings are via the rotationally symmetric O p_z orbitals. By comparing calculated band structure along ΓM for different θ_{Δ} with ARPES data shown in figure 4.6 we find that 6° gives the best match confirming the value obtained by Shen *et al.* [64].

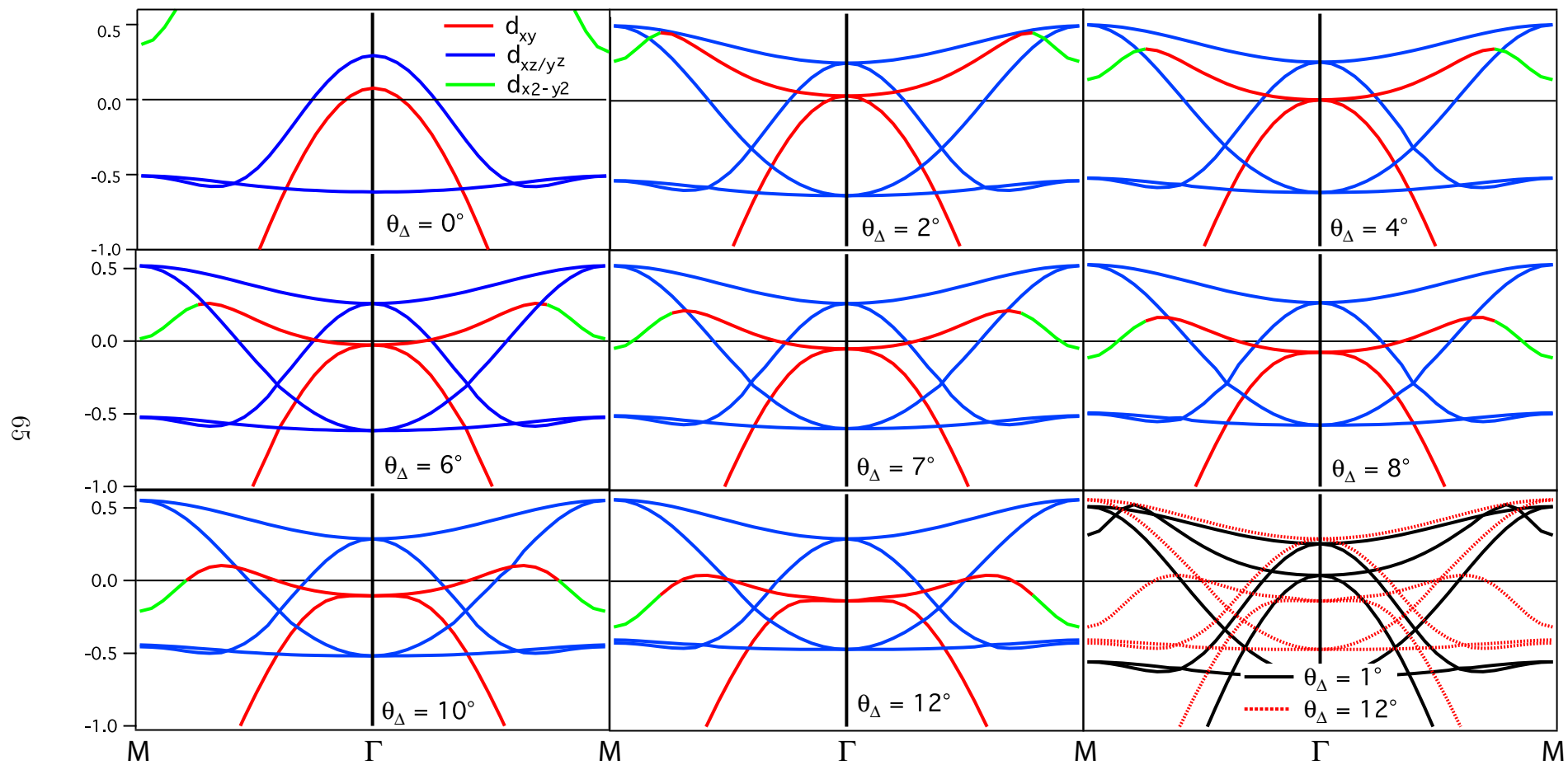


Figure 4.4: Surface layer band structure for different rotation angle of the slab octahedra θ_{Δ} . Green denotes $d_{x^2-y^2}$ orbital character, red d_{xy} orbital character and blue $d_{xz/yz}$ orbital character.

The Fermi surface and band structure of the surface layer were measured after cleaving the samples at 10 K and pressures better than 4.5×10^{-11} mbar. Figure 4.5 shows the expected band structure along ΓM and MX direction including surface and bulk bands calculated within LDA. Both directions are equivalent for the surface band structure but strong overlap with the bulk bands along ΓM direction could potentially make the analysis unreliable for this cut.

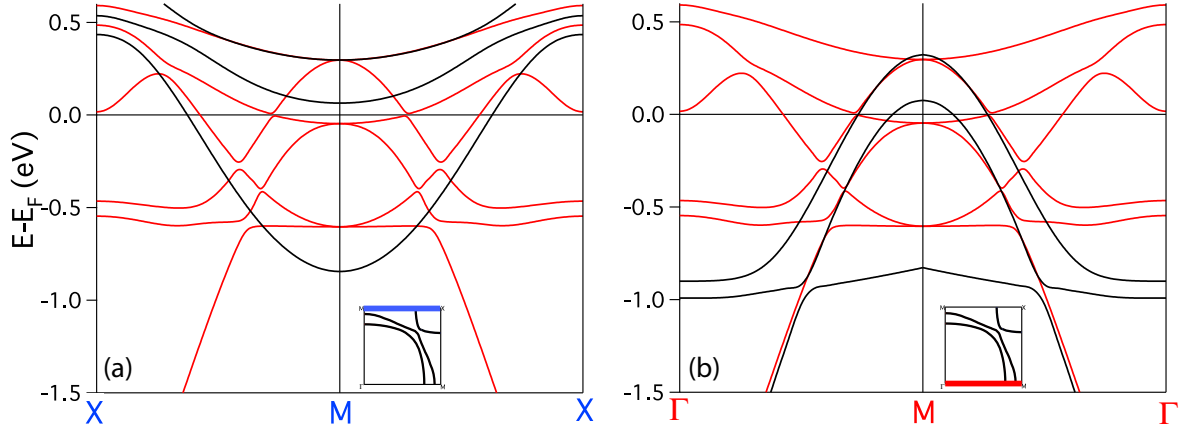


Figure 4.5: LSDA+SOC surface layer band structure for $\theta_{\Delta} = 6^{\circ}$ (the SOC gaps were artificially closed for clarity): (a) along MX direction, (b) along ΓM direction. The red lines denote surface bands and the black lines denote the bulk bands.

On figure 4.6 we present the band structure measured along MX direction. The

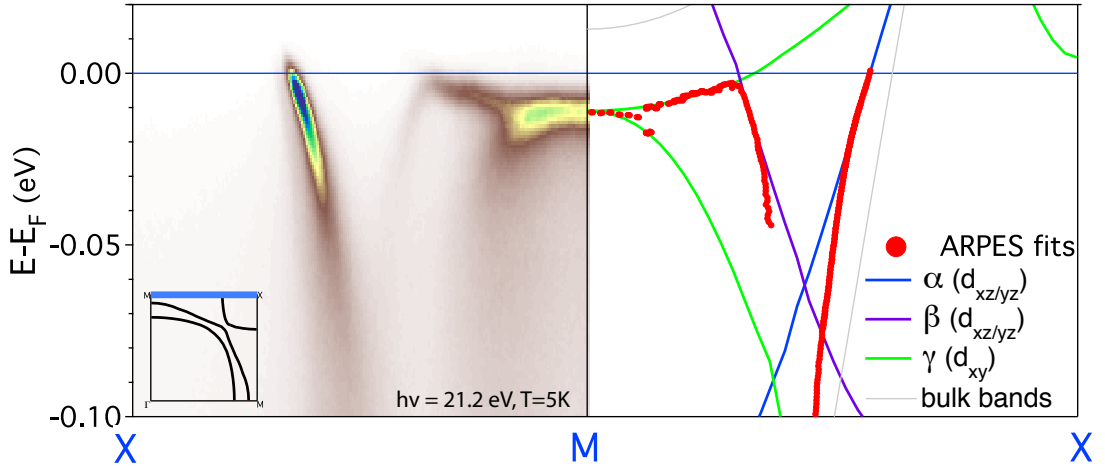


Figure 4.6: ARPES vs LSDA+SOC surface band structure along MX direction. LSDA+SOC band structure was renormalized as described in the text.

rotation angle can be estimated accurately by the positions of two minima discussed before relative to the Fermi level. We do not observe any spectral weight at Γ (X) point meaning that the $d_{x^2-y^2}$ minimum must be located above the Fermi level. However, at the M point we clearly see the band bottom of the d_{xy} band. The same position of both features relative to the Fermi level is found in the calculated band structure only for

$\theta_{\Delta} = 6^{\circ}$. For $\theta_{\Delta} = 7^{\circ}$, the $d_{x^2-y^2}$ part of the band is already below the E_F and for $\theta_{\Delta} = 5^{\circ}$ the d_{xy} part is still above it, which is not consistent with the observed spectra.

Figure 4.7 presents the band structure measured along ΓM direction. The change

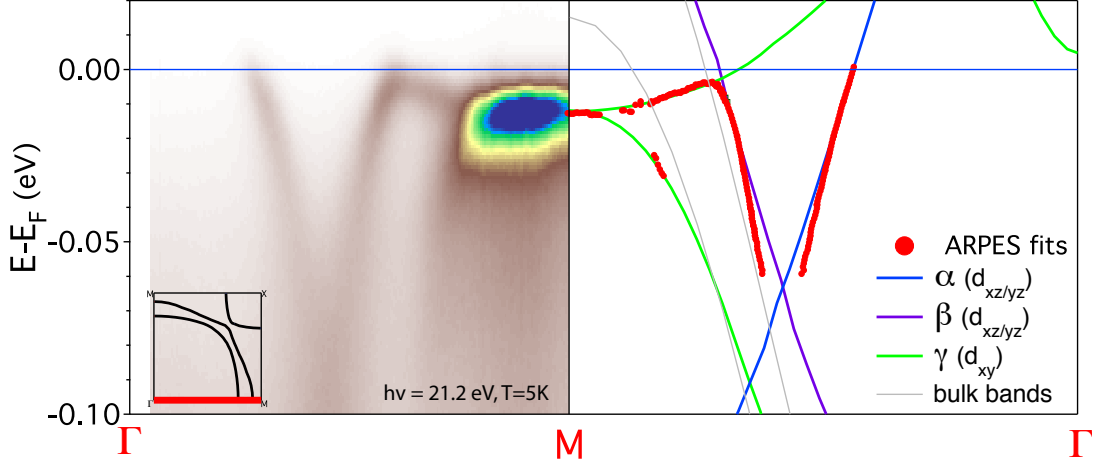


Figure 4.7: ARPES vs LSDA+SOC surface band structure along ΓM direction. LSDA+SOC band structure was renormalized as described in the text.

of the relative band intensity compared to MX direction is due to matrix element effects discussed in Chapter 2. The measured Fermi velocities of the bands show exactly the same values as for the MX direction meaning that spectral weight of the bulk bands compared to the surface bands is negligible.

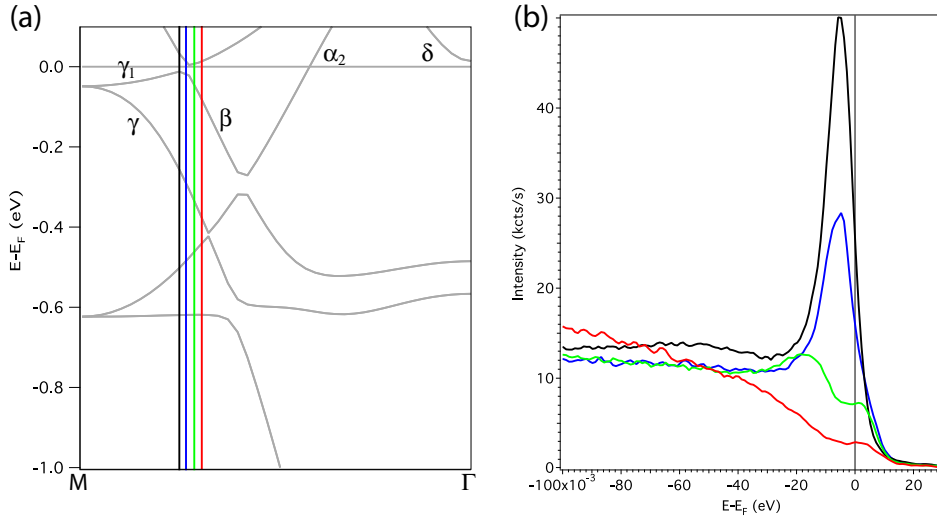


Figure 4.8: Panel (a) band structure of the surface along ΓM direction from LSDA+SOC calculations. Color lines denote the EDC positions showed in panel (b). EDCs show a peak dispersing below Fermi level and a large shoulder above it indicating another peak just above E_F . Clear two peak structure indicates opening of the gap, in this case driven by the SOC.

A feature that distinguishes our measurement from previous studies is the observation

of a gap induced by spin-orbit coupling between β and γ_1 bands, as presented in figure 4.8. All EDC's along the colored lines show spectral weight above the Fermi level. Right at the crossing between β and γ_1 bands, at the position of the blue line, the EDC shows a peak below the Fermi level and a large shoulder above it, indicating another peak just above E_F . This means that the spin-orbit gap opens right at the Fermi level. Thus the topology of the Fermi surface differs from that reported by Shen *et al.* [64], which is reproduced in figure 4.1.

The LDA+SOC calculation of the surface layer Fermi surface for $\theta_\Delta = 6^\circ$ is presented in figure 4.9. Due to spin-orbit coupling the d_{xy} band hybridises with d_{xz} band opening a gap at the Fermi level. This leads to changes in the Fermi surface. The three fundamental surface bands, which are split off the corresponding bulk bands recombine into a square pocket around the Γ point (α_1) and two lens shaped pockets (β and γ_1) created with hybridised d_{xy} and $d_{xz/yz}$ character. These sheets are intriguingly similar to Fermi surface sheets observed by Tamai *et al.* in $\text{Sr}_3\text{Ru}_2\text{O}_7$ [72]. We therefore follow the notation introduced in this paper.

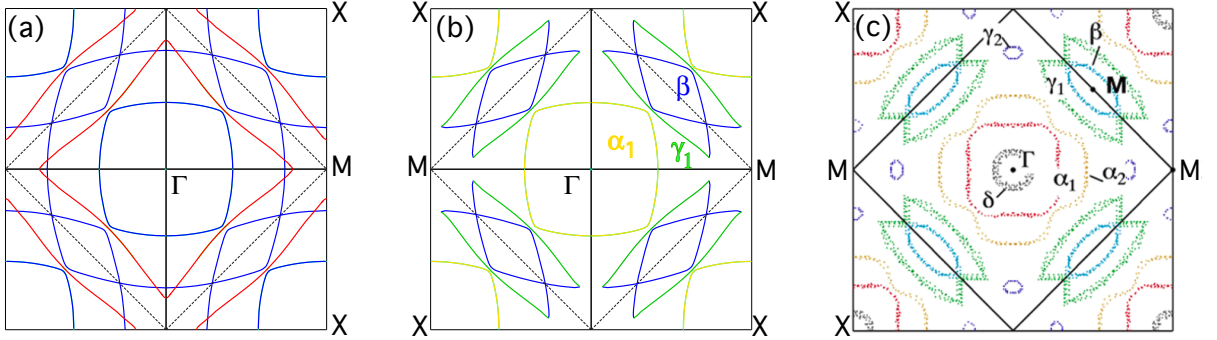


Figure 4.9: Fermi surface of the top-layer of Sr_2RuO_4 : panel (a) from plain LDA calculations - blue contours denote $d_{xz/yz}$ and red d_{xy} orbital character. Panel (b) Fermi surface from LSDA+SOC calculations. SOC causes hybridization between the d_{xy} and $d_{xz/yz}$ orbitals resulting in an opening of the gap at the Fermi level along the ΓM direction. This changes the Fermi surface topology from that proposed by Shen *et al.* in Ref. [64]. Panel (c) shows the Fermi surface of $\text{Sr}_3\text{Ru}_2\text{O}_7$ reproduced from [72]) for comparison.

The α_1 pocket is a simple equivalent of the α pocket of the bulk of Sr_2RuO_4 and is hole-like and purely $d_{xz/yz}$ in orbital character. Backfolding into the surface changes the shape of the β sheet from almost square-like to lens-shaped but does not change orbital character or polarity compared to the bulk. γ_1 is reminiscent of the bulk γ band but hybridises with β to create an electron pocket with complex shape.

The main difference of the Fermi surface of the Sr_2RuO_4 surface layer and bulk $\text{Sr}_3\text{Ru}_2\text{O}_7$ is thus the doubling of the number of bands at the Fermi level due to the bilayer structure of $\text{Sr}_3\text{Ru}_2\text{O}_7$. Furthermore, due to the higher rotation angle of $\theta_\Delta = 7^\circ$ in $\text{Sr}_3\text{Ru}_2\text{O}_7$, its $d_{x^2-y^2}$ band crosses the Fermi level creating two circular pockets (δ) at the Γ point.

Intriguingly the mass renormalization factors in $\text{Sr}_3\text{Ru}_2\text{O}_7$ are much higher than those of Sr_2RuO_4 [72]. The mechanism responsible for this effect is not understood yet. However, the similarity between the band structure of the top-layer of Sr_2RuO_4 and the bulk

of $\text{Sr}_3\text{Ru}_2\text{O}_7$ allows us to isolate the effect of the octahedra rotation on the mass enhancement. For α_1 the renormalization factor was calculated as a ratio of $v_{F,LDA}$ to $v_{F,ARPES}$. Because neither γ_1 or β crosses the Fermi level along the ΓM direction, a different approach was applied. For γ_1 we compared the curvatures of the LDA and ARPES bands at the band bottom. For β , the slope of the band between -0.012 eV and -0.015 eV was compared to that of LDA in the corresponding energy window. Table 4.1 summarizes the renormalization factors for the bulk and the surface of Sr_2RuO_4 and the bulk of $\text{Sr}_3\text{Ru}_2\text{O}_7$.

	bulk Sr_2RuO_4	surface Sr_2RuO_4 (ΓM)	$\text{Sr}_3\text{Ru}_2\text{O}_7$ (ΓM)
α_1	3.0	3.9	9
β	3.5	4.5	7
γ_1	5.5	6.7	8.5

Table 4.1: Summary of mass renormalization factors for the bulk and the surface of Sr_2RuO_4 and the bulk of $\text{Sr}_3\text{Ru}_2\text{O}_7$. Values for the bulk of Sr_2RuO_4 are from [73] and for $\text{Sr}_3\text{Ru}_2\text{O}_7$ from [72].

With this approach we find renormalization factors of the surface layer of Sr_2RuO_4 that are $\approx 20\%$ higher than those of the bulk but 30 – 50% lower than those of $\text{Sr}_3\text{Ru}_2\text{O}_7$. We caution, however, that these values may change if a single electron band structure for a semi-infinite crystal, which would likely show a larger bandwidth of the $d_{xz/yz}$ sheet, would be used. However, even using $v_{F,LDA}$ of the bulk α band for the surface α_1 pocket does not reproduce the large renormalization found in $\text{Sr}_3\text{Ru}_2\text{O}_7$. Hence, we conclude that the rotation of the octahedra plays some role in the ruthenate family but cannot explain the marked difference in the mass renormalization factors and thermodynamic properties between single and double layered compounds.

Instead, the unusually high mass enhancement in $\text{Sr}_3\text{Ru}_2\text{O}_7$ might be related to the redistribution of charge within RuO_2 bilayer and/or the energy of the van Hove singularity. Intriguingly, its position relative to the Fermi level in these three systems scales with the strength of the interactions. In bulk Sr_2RuO_4 it was found 14 meV [74] above the Fermi level, in the surface layer of Sr_2RuO_4 it lies 10 meV below the Fermi level and in $\text{Sr}_3\text{Ru}_2\text{O}_7$ 4 meV [72] below the Fermi level.

4.2 Momentum dependent mass renormalization

The fact that Sr_2RuO_4 is a strongly correlated metal is reflected in the large enhancement of the effective masses. Experimental values show a factor of two higher mass renormalization for the γ band (≈ 6) than for the α and β bands (≈ 3). This pronounced mass anisotropy is rather surprising as all the bands belong to the same t_{2g} manifold and the on-site correlations are equal for all of them at least within standard Hubbard models [75, 76]. The band structure calculations revealed van Hove singularity in the d_{xy} band 14 meV above Fermi level localized at M point [74]. Figure 4.10 shows the density of states from an LSDA+SOC calculation projected on d_{xy} and $d_{xz/yz}$ orbitals. Because the

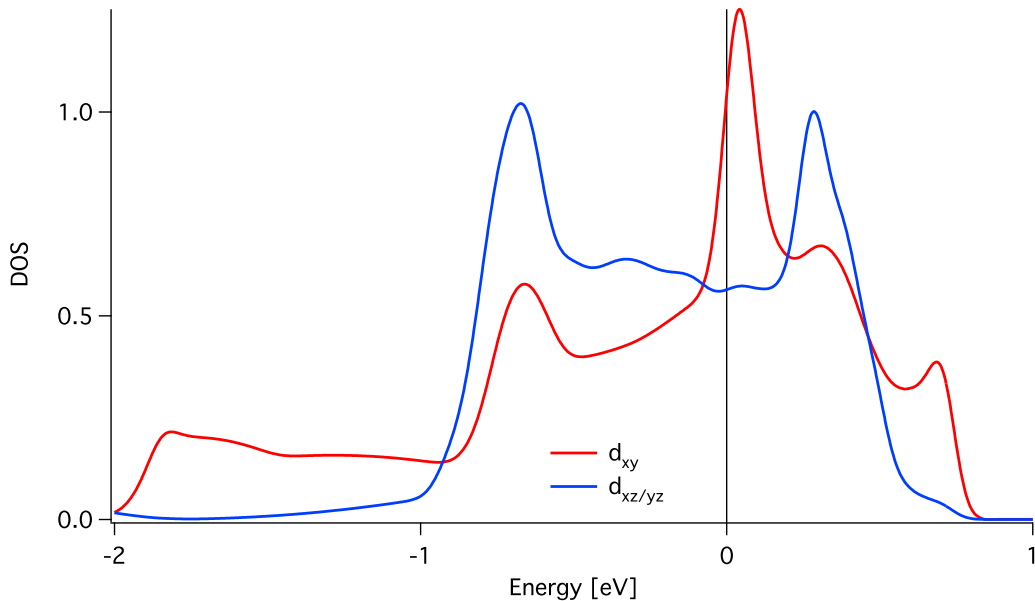


Figure 4.10: Single-electron density of states for d_{xy} and $d_{xz/yz}$ orbitals. The peak in the density of states related to van Hove singularity which was found to be 14 meV above the Fermi level in ARPES [74] experiments lies at 40 meV in the calculations.

enhanced DOS in the vicinity of the Fermi level may increase the renormalization, the orbital anisotropy in Sr_2RuO_4 was primarily ascribed to the proximity of the van Hove singularity [60, 76]. However, recent DMFT calculations [77] showed that the effective mass anisotropy between the in-plane and out-of-plane orbitals can at least partially be explained by the Hund's rule coupling J . Higher values of J do not only increase overall the values of the mass renormalization factors but also the anisotropy.

In table 4.2 we have summarized the mass renormalization factors from de Hass van Alphen, ARPES measurements and DMFT calculation reported in the literature. The

Fermi Surface Sheet	α	β	γ
dHvA [73]	3.0	3.5	5.5
ARPES [67, 74]	2.4		6
DMFT[77]	2.4/3.3	2.4/3.3	3.2/4.5

Table 4.2: Summary of mass renormalization factors. Values of DMFT factors were obtained for constant $U = 2.3$ eV and $J = 0.3/04$ eV.

DMFT results are in reasonable agreement with the experimental values for the α and β bands but underestimate the mass renormalization for the γ band. The authors of [77] concluded that the higher experimental value for the in-plane orbital is likely due to proximity of the van Hove singularity.

It is an open question whether the van Hove singularity can result in a momentum dependent mass renormalization, enhancing the mass only in its vicinity, or if it leads

to an isotropic self-energy. The dominant interaction responsible for the mass renormalization in Sr_2RuO_4 is electron-electron scattering, which is exponentially screened in a three-dimensional Fermi liquid and thus has no momentum dependence in simple metals. However, the large number of states with similar \mathbf{k} near a van Hove singularity might alter the general result and lead to a non-local electron-electron interaction, which in turn would result in a momentum dependent self-energy.

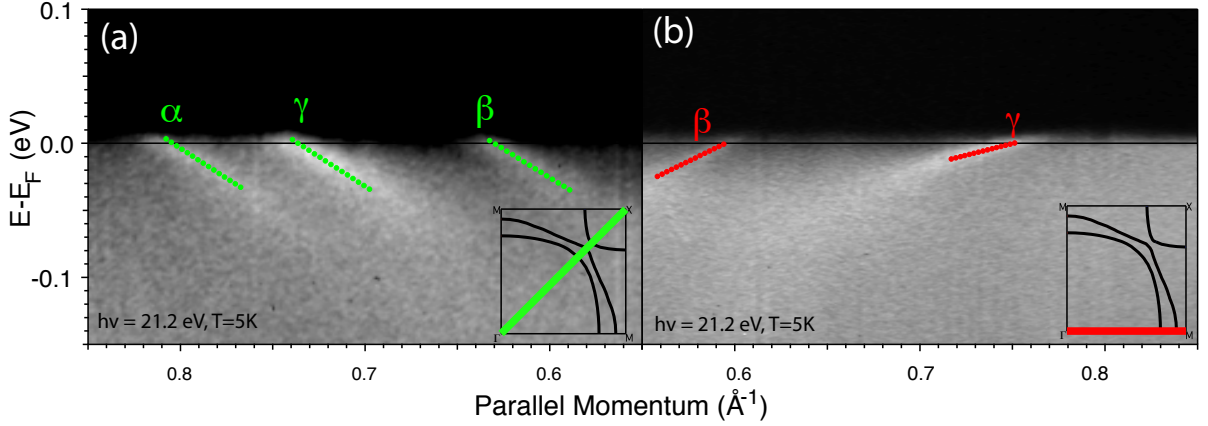


Figure 4.11: Bands structure of Sr_2RuO_4 : panel (a) along ΓX direction, panel (b) along ΓM direction. For ΓM the γ band has a factor of two lower Fermi velocity than the β band, while for the ΓX direction all three bands disperse almost parallel.

In order to address this question we first investigate the band structure of Sr_2RuO_4 along the high symmetry directions ΓM and ΓX . Figure 4.11 shows ARPES data taken at 8K after cleaving the samples at room temperature and pressures of $\sim 10^{-9}$ mbar in order to diminish the intensity of the surface bands. This data immediately reveals a striking difference in Fermi velocities. Along the ΓM direction the γ band has roughly a factor of two lower Fermi velocity than the β band whereas all three bands disperse almost parallel along the ΓX direction. Comparing this data to single-electron Fermi velocities obtained from LDA+SOC calculations we determined the mass renormalization factors, shown in table 4.3. Intriguingly, the measured effective masses for both, γ and β sheets, show a marked anisotropy between the ΓX and ΓM directions. The high anisotropy

	ΓM	ΓX	MX
α	-	2.5	2.4
β	3.4	4.1	-
γ	5.8	3.2	-

Table 4.3: Mass renormalization factors measured by ARPES along high symmetry directions.

of the γ band renormalization points towards an enhanced self-energy near the van Hove singularity at the M-point. However, the anisotropy observed for the β band is unexpected and does not fit this scenario. The presence of a k -dependent renormalization in both

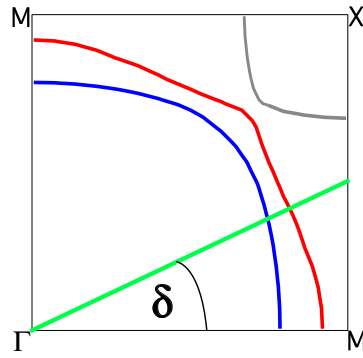


Figure 4.12: The geometry for the radial measurement of the band structure. δ denotes the azimuthal angle.

bands rather indicates a common origin of the effect. In order to test this hypothesis we measured the quasiparticle band structure along radial cuts as indicated in figure 4.12.

The raw data for six example band structure cuts is presented in figure 4.13, and reproduced in figure 4.14 together with peak positions and single-electron LDA+SOC bands.

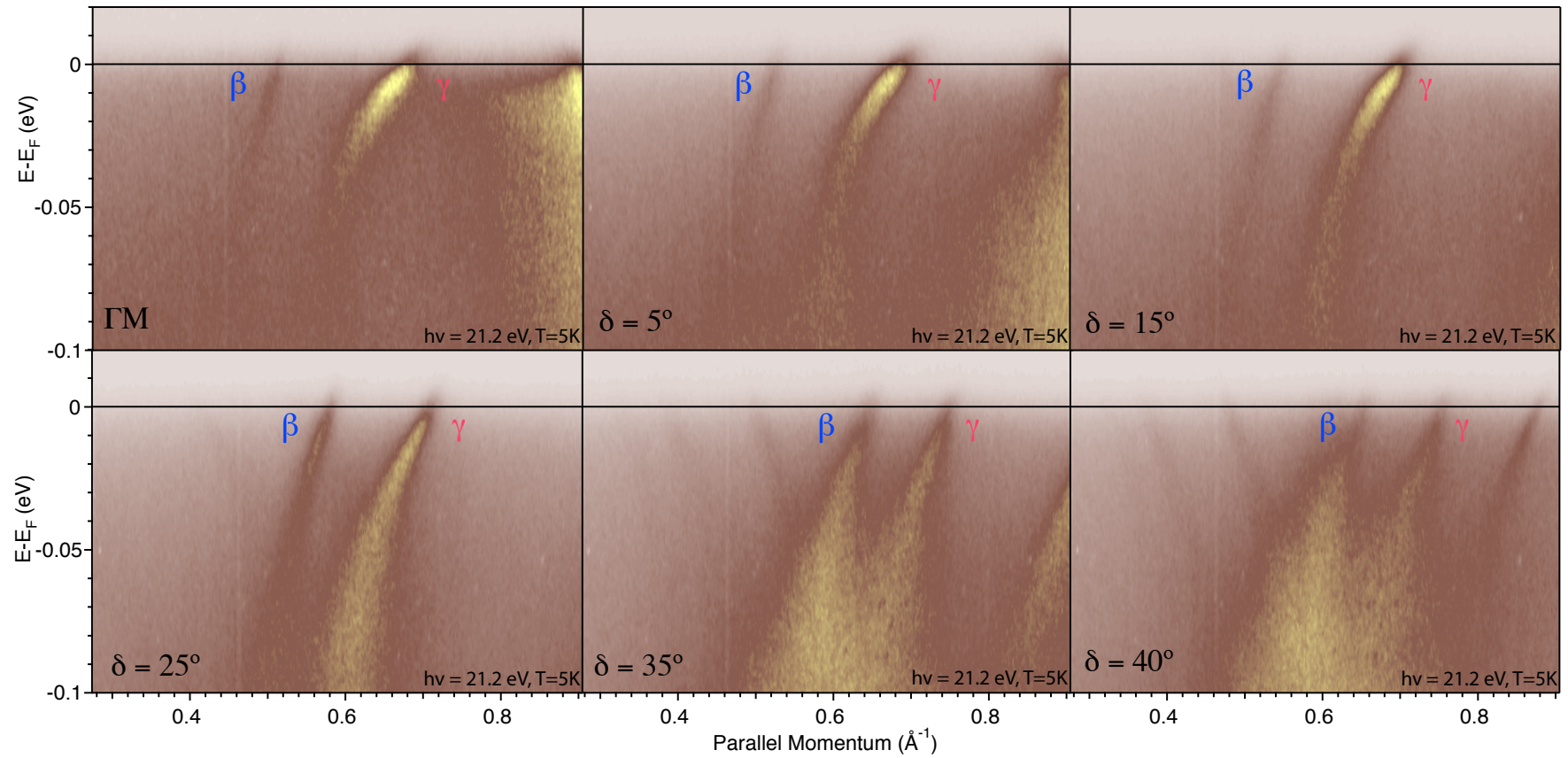


Figure 4.13: Band structure measured along the radial cuts, defined in figure 4.12.

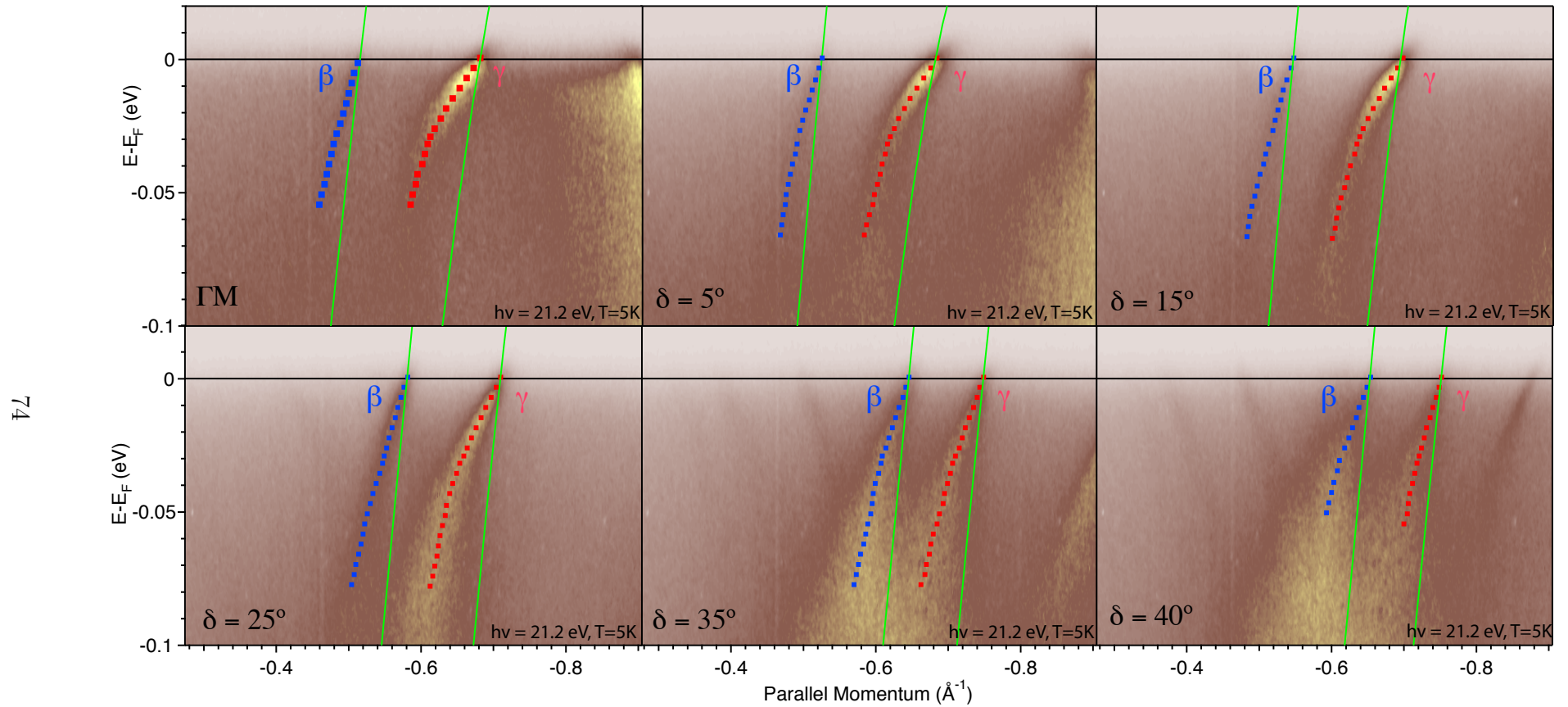


Figure 4.14: Same data as in figure 4.13 together with extracted dispersion curves. The green lines denote single-electron bands calculated by LSDA+SOC, red dots denote the peak positions of the γ band and blue dots denote the peak positions of the β band.

The Fermi velocities of the β and γ bands change as the function of azimuthal angle δ . In order to exclude the possibility that the observed angle dependance is entirely due to band structure effects, we have calculated the single-electron Fermi velocities for the β and γ bands for the same cuts in momentum space using LDA+SOC and compared them to the measured ones. The results are presented in figure 4.15. The LDA calculations

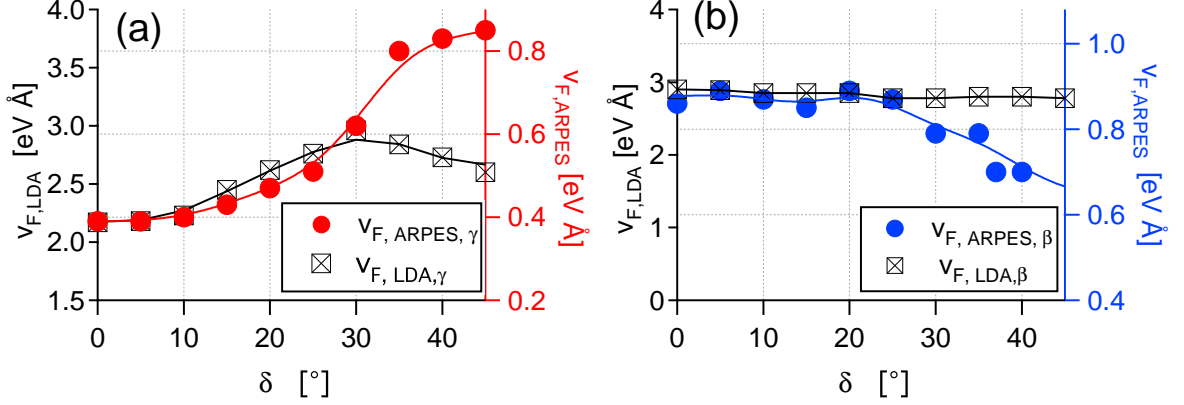


Figure 4.15: Fermi velocities measured in ARPES and calculated by LSDA+SOC as a function of azimuthal angle δ for: (a) the γ band and (b) the β band. Dots are the measured/calculated values and the lines provide guides to the eye.

show an almost constant Fermi velocity as a function of azimuthal angle for the β band. The ARPES data show the same trend up to $\delta \approx 30^\circ$ where they start to drop. The single-electron values for the γ band, on the other hand, show a non-monotonic behavior. They increase up to 30° before they start to decrease slightly.

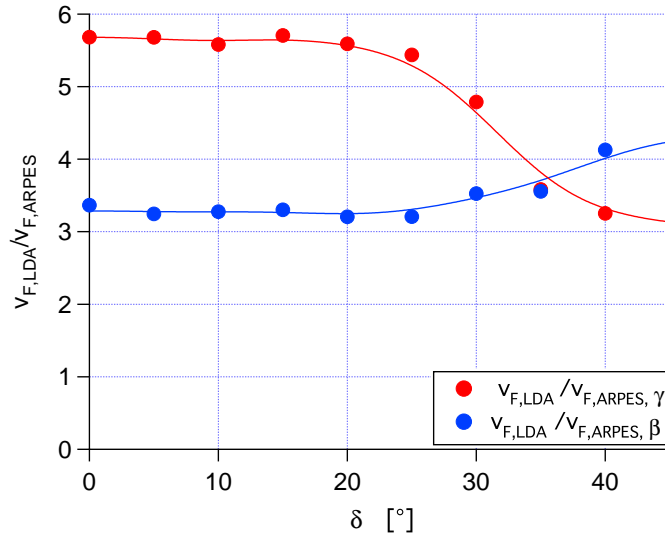


Figure 4.16: Renormalization factors as a function of the azimuthal angle δ calculated using Fermi velocities shown in figure 4.15. The red line is for the γ band and the blue line for the β band. Dots are the measured/calculated values and lines are guides to the eye.

Values measured in ARPES show initially a very similar trend but at $\delta = 30^\circ$ they do not turn over but instead continue to increase. This change confirms the mass anisotropy found before and reveals that the mass renormalization factor has a strong momentum dependence for both bands. Figure 4.16 presents the mass renormalization factors as a function of azimuthal angle δ , calculated using the Fermi velocities presented in figure 4.15. The fact that the mass renormalizations of the β and γ bands are constant below 30° and start to change simultaneously in both bands above 30° strongly suggest a common origin of the momentum dependence. In the following we show that hybridization due to strong spin-orbit splitting is the primary reason for the momentum dependence of the renormalization and can account for the effects observed in both bands.

Due to the crystal symmetry hybridization between d_{xy} and $d_{xz/yz}$ orbitals is only possible through spin-orbit coupling. In Chapter 3 we showed how SOC leads to changes the Fermi surface by opening gaps between the γ and β bands. This effect also affects the orbital content of these sheets. In figure 4.17 we show the orbital character of the β and γ bands as a function of azimuthal angle for $k_z = 0$. Evidently, its evolution with angle shows

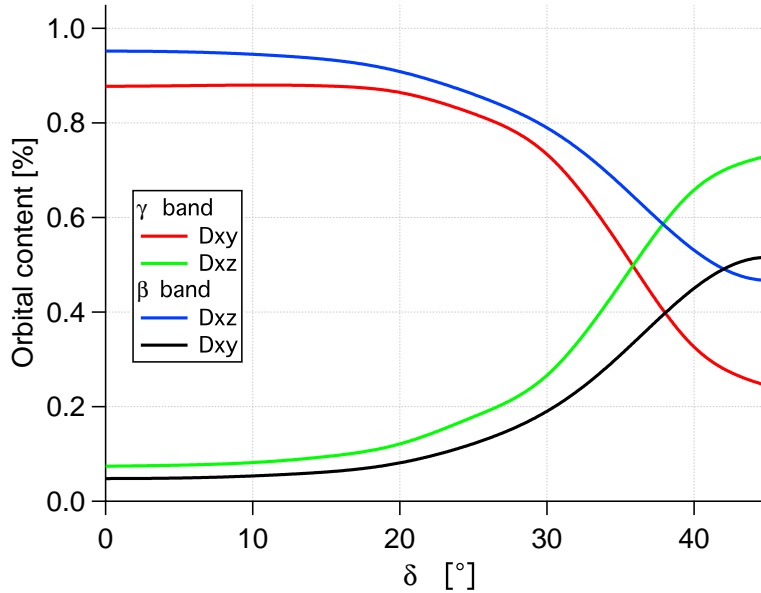


Figure 4.17: The orbital content for the β and γ band for $k_z = 0$.

a striking similarity to the observed momentum dependence of the mass renormalization. The dominant orbital content (d_{xy} for the γ band and $d_{xz/yz}$ for the β band) starts to decrease around 25° and the final orbital character along ΓX is an admixture of both orbitals. Based on the orbital mixing we can model the mass renormalization factor for a given band by a linear combination of the orbital renormalization constants

$$Z_{\text{FL}}^{-1} = \left(1 - \frac{\partial \Re \Sigma}{\partial \epsilon} \right) \Big|_{\epsilon = \epsilon_F} = \frac{v_{F, \text{ARPES}}}{v_{F, \text{LDA}}} \quad (4.1)$$

(see section 2.3.1 for details) and the orbital content:

$$Z_{\text{FL},\gamma}^{-1}(\delta) = Z_{xy}^{-1} \times D_{xy,\gamma}(\delta) + Z_{xz}^{-1} \times D_{xz,\gamma}(\delta), \quad (4.2)$$

$$Z_{\text{FL},\beta}^{-1}(\delta) = Z_{xy}^{-1} \times D_{xy,\beta}(\delta) + Z_{xz}^{-1} \times D_{xz,\beta}(\delta),$$

where $D_{i,j}$ denotes the orbital content of orbital i in a band j . Before we go into details of the model we will first discuss the k_z dispersion of the Sr_2RuO_4 bands. As shown in figure 4.18 the γ band almost does not change along k_z as it is derived from the in-plane d_{xy} orbitals. However, the k_z - dispersion of the α and β bands generated by the out-of-plane $d_{xz/yz}$ orbitals is sufficiently large to cause crossings between the β and γ sheets for $k_z = 0$ to $k_z = 0.5$ which disappears for $k_z = 0.75$ to $k_z = 1$. Here, k_z is given in units of $\frac{\pi}{c^*}$ with $c^* = \frac{c}{2}$, so that a value of 1 corresponds to the Brillouin zone boundary. In figure 4.19 we illustrate the effect of this slight k_z - dispersion on the orbital mixing by

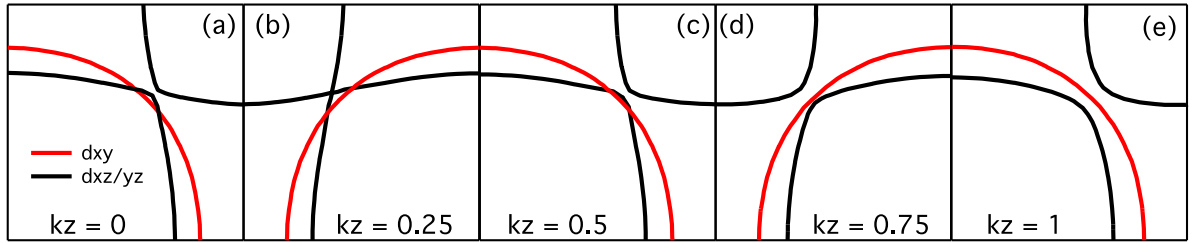


Figure 4.18: Fermi surface of Sr_2RuO_4 for different values of k_z . Calculations were performed without spin-orbit coupling for easier identification of the changes along k_z axis.

comparing LDA with LDA+SOC calculations for two extreme cases: $k_z = 0.25$ for which the overlap is largest and $k_z = 1$ where the separation between the β and γ sheets has the highest value.

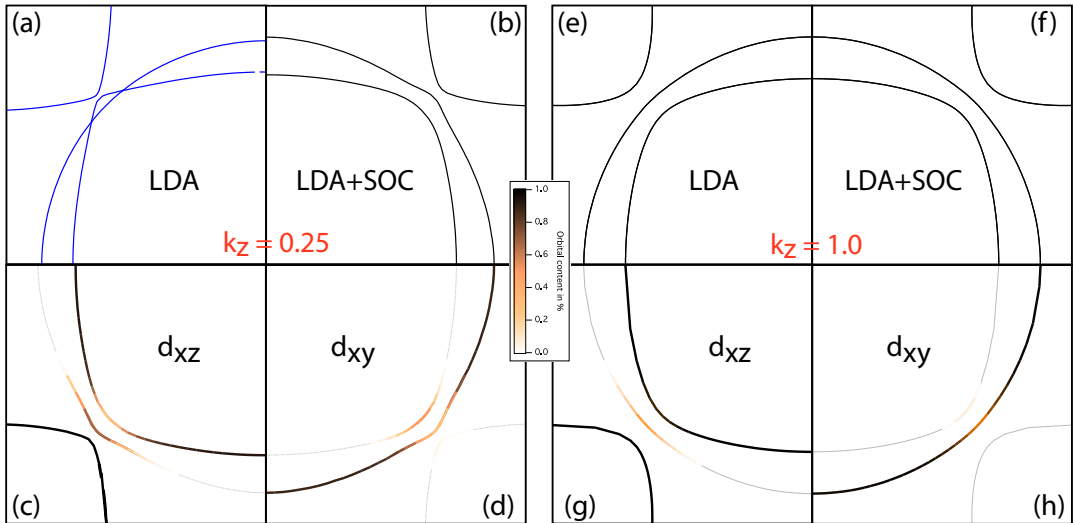


Figure 4.19: Comparison of the topology and the orbital mixing for the FS of Sr_2RuO_4 at $k_z = 0.25$ panels (a-d) and at $k_z = 1$ panels (e-h). Clearly the orbital mixing is much stronger for $k_z = 0.25$, for which the overlap between the β and γ bands is present.

Clearly, the orbital mixing is much stronger for $k_z = 0.25$ where the overlap between the β and γ sheets is large and increases towards Γ .

In order to follow the change in the strength of the orbital mixing with k_z we have calculated the band structure and the orbital character for both high-symmetry directions along the k_z axis. The results of the calculations with and without spin-orbit coupling are presented in figure 4.20. Along the Γ M direction γ and β show almost no k_z dependence of the Fermi wave vector and orbital character: γ remains almost purely d_{xy} - and β $d_{xz/yz}$ -like. The situation changes drastically for the Γ X direction where β shows a strong variation of the Fermi wave vector along the k_z axis within LDA. It initially increases and after “meeting” the α band at $k_z = 0.3$ it starts to decrease, crossing γ at $k_z = 0.6$ from where it continues to decrease. Introducing spin-orbit coupling almost entirely removes the k_z dependence of the Fermi wave vector. However, it induces orbital mixing with a pronounced k_z dependence. Within LDA+SOC the γ sheet is more $d_{xz/yz}$ -like below

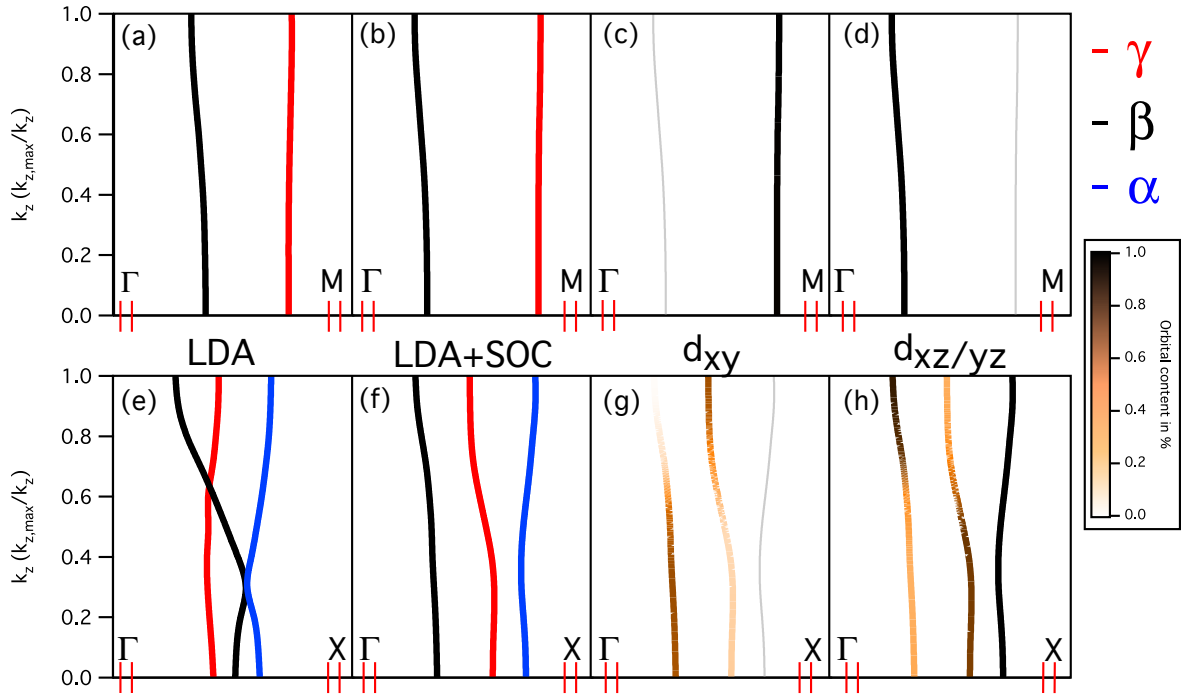


Figure 4.20: Band structure of Sr_2RuO_4 as a function of k_z for two high symmetry directions. Panels (a) and (e) show the results of LDA calculations without SOC and the rest of the panels including SOC. Colour code in panels (a), (b), (e) and (f) denotes the FS sheet while in panels (c), (d), (g) and (h) the orbital content.

$k_z = 0.6$ whereas above that value it retains its “original” d_{xy} character and vice versa for the β beta band. The strong k_z dependence of the orbital mixing means that knowledge of experimental value of k_z is crucial. From recent studies of the band structure of Sr_2RuO_4 as a function of phonon energy $h\nu$ [78], the normal component of the Fermi wave vector for $h\nu = 21.2$ eV can be estimated as $k_z \approx 0.6$ at $k_{\parallel} \approx$ FS - crossing.

Because the experimental value of k_z has some uncertainty we will estimate the orbital masses using the fact that the orbital content is constant along the k_z axis for the

Γ M direction. From equation 4.2 we can fit m_{xy} and $m_{xz/yz}$ to give the best match to $m_{ARPES,j}^*(\Gamma M, k_z = 0)$ for $D_{i,j}(\Gamma M, k_z = 0)$. Obtained orbital masses can be then used to calculate $m_j^*(\delta, k_z)$ for $D_{i,j}(\delta, k_z)$. Furthermore we have fixed the orbital mass ratio to $m_{xy} = 1.6 \times m_{xz/yz}$ as given by the DMFT calculations [79]. The experimental anisotropy for the Γ M direction is found to be 1.8, meaning that the theoretical value will either underestimate m_γ^* or overestimate m_β^* . Because the latter case is unphysical we find the orbital masses by fitting equation 4.2 to $m_{ARPES,\beta}^*$ which gives $m_{xz/yz}^* = 3.2$ and $m_{xy}^* = 5.1$. Using these values and orbital content $D_{i,j}(\delta, k_z)$, presented on figure 4.21, we have calculated $m_j^*(\delta, k_z)$ for $k_z = [0, 1; 0.1]$. The results are shown in figure 4.22.

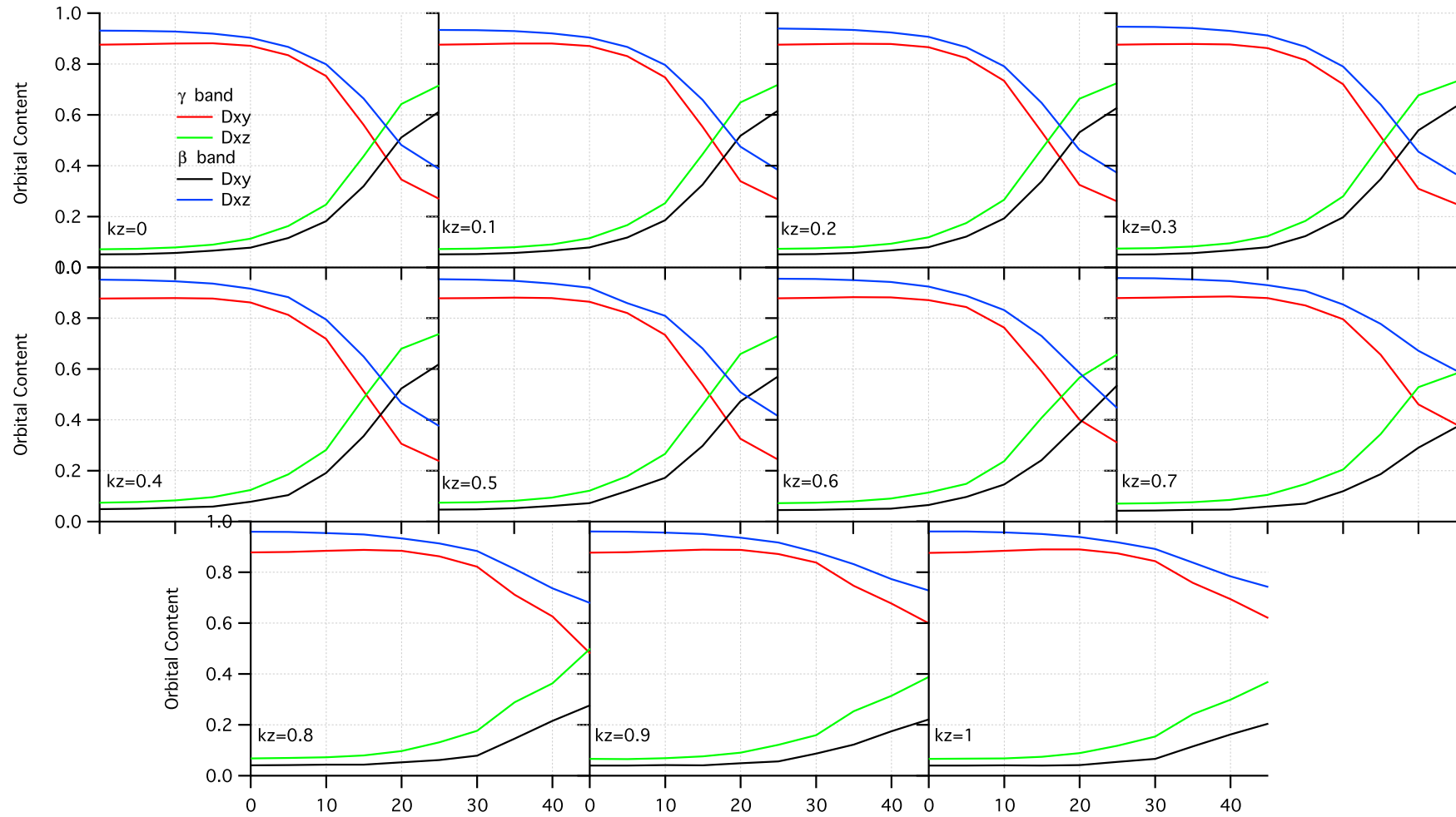


Figure 4.21: Orbital content of the γ and β bands as a function of azimuthal angle for different values of k_z .

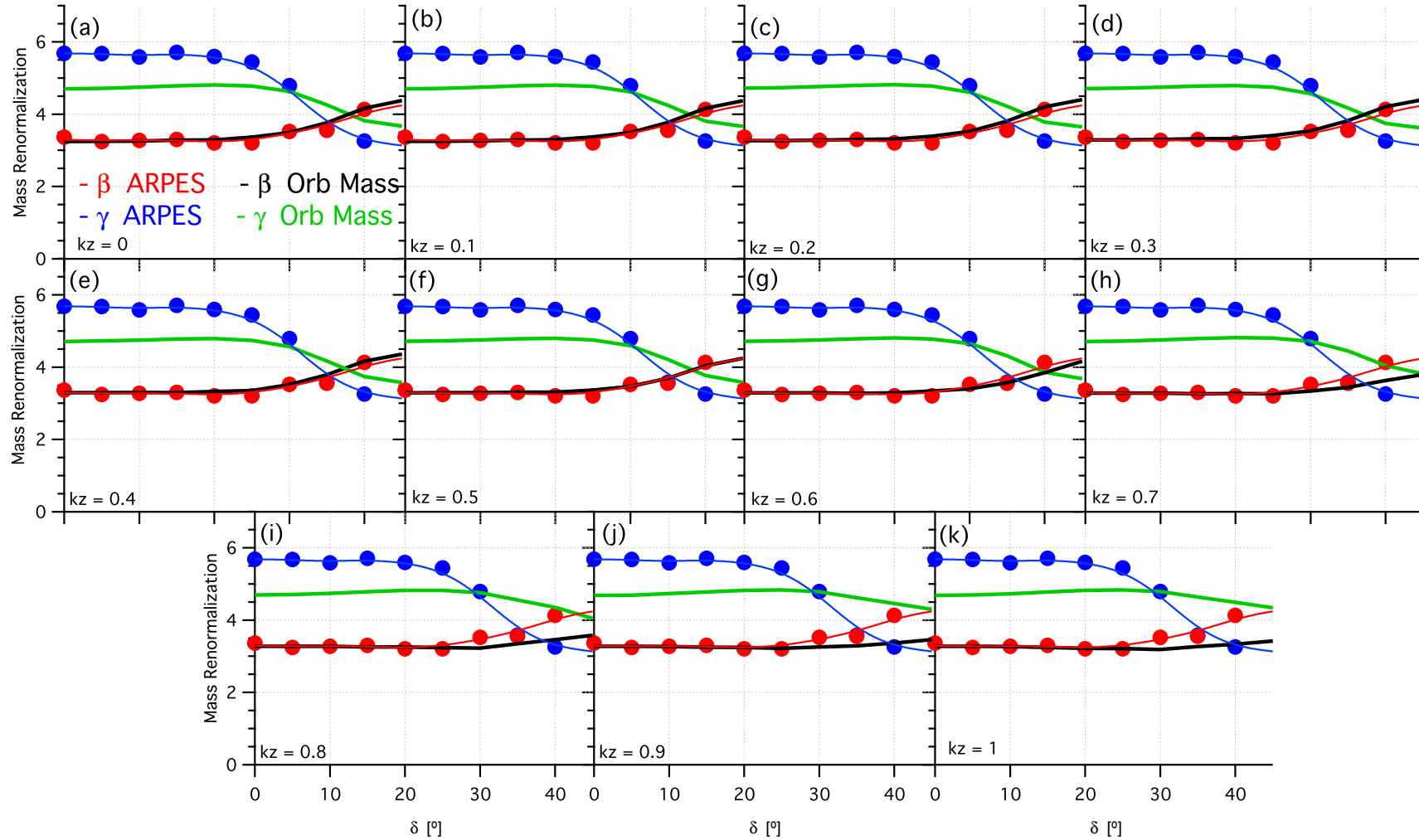


Figure 4.22: Mass renormalization factors as a function of azimuthal angle δ obtained from ARPES compared to mass renormalization factors calculated from orbital mixing for different k_z assuming constant orbital renormalization constants given by $Z_{FL,xz}^{-1} = 3.2$ and $Z_{FL,xy}^{-1} = 5.1$.

From the results obtained within our model we conclude that for the experimental value of $k_z \approx 0.6$ the renormalization factor of the β band $Z_{\text{FL},\beta}^{-1}(\delta, k_z = 0.6)$ almost perfectly agrees with the experimental, which means that the renormalization factor of $d_{xz/yz}$ orbital is momentum independent. The effect on the γ band on the other hand is reproduced qualitatively only. In particular the model underestimates the renormalization along ΓM . This could indicate additional many-body effects, possibly caused by the vicinity of the van Hove singularity. However, a full understanding of such effects would require more theoretical work, which is beyond the scope of this thesis.

Another factor supporting the orbital mixing scenario is the completely isotropic velocity of the α band. The mass renormalization factor for the ΓX direction is $Z_{\alpha}^{-1} = 2.5$ (see table 4.3). This value is very close to the one given by Ingle *et al.* [67] for a cut along the Brillouin zone boundary (MX). We have repeated the measurement along MX to confirm the isotropy of the mass renormalization for the α band. Given that the orbital mixing is absent for this pocket (see figure 4.21) this strongly supports the above scenario. Fermi velocities and renormalization factors for all bands are summarized in table 4.4

Finally we note that the enhanced renormalization of the γ band is intimately related to a kink in this band around 40 meV below the Fermi level that can readily be observed in the dispersion plots in figures 4.13 and 4.14 . We will discuss the kink and its possible origin in the next section.

	ΓM			ΓX			MX		
	$v_{F,LDA}$	$v_{F,ARPES}$	Z^{-1}	$v_{F,LDA}$	$v_{F,ARPES}$	Z^{-1}	$v_{F,LDA}$	$v_{F,ARPES}$	Z^{-1}
α	-	-	-	2.7	0.92	2.5	2.55	1.07	2.4
β	2.9	0.87	3.4	2.78	0.68	4.1	-	-	-
γ	2.25	0.39	5.8	2.6	0.82	3.2	-	-	-

Table 4.4: Mass renormalization factors measured by ARPES along high symmetry directions.

4.3 Orbital selective kink in the bulk bands

The origin of the orbital selective kink, which was first observed by Iwasawa *et al.* [68], is still an open question. The authors of Ref. [68] ascribed it to electron-phonon coupling enhanced by ferromagnetic fluctuations. Here we will show that an alternative explanation may also come from electron-electron interaction. In contrary to the work of Iwasawa *et al.* [68] our data clearly show that the coupling strength, has a strong momentum dependence. In figure 4.23 we present four example band structure cuts for $\delta = 0^\circ, 25^\circ, 35^\circ$ and 40° with fitted peak positions (red markers) and bare LDA dispersions (green lines). Clearly, the

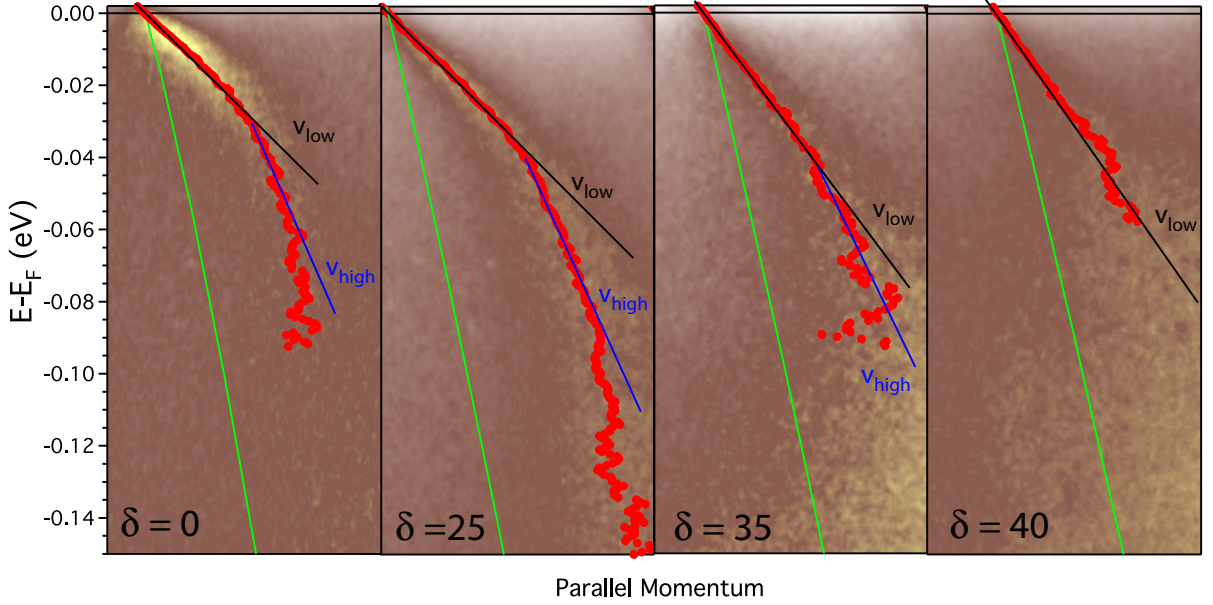


Figure 4.23: Momentum dependent kink in the γ band for selected azimuthal angles. Red markers: fitted peak positions from ARPES data, green lines: bare LDA bands, black and blue lines: linear fits to the dispersion above and below the kink respectively.

kink strength weakens with increasing δ , which suggest that its momentum dependence may be driven by the orbital mixing. In order to quantify this trend we have evaluated its strength as a ratio of the band slope v_{high} below (high binding energies) and v_{low} above the kink (low binding energies) indicated by blue and black lines in figure 4.23:

$$\lambda_R = \frac{v_{\text{high}} - v_{\text{low}}}{v_{\text{low}}} \quad (4.3)$$

In figure 4.24 we compare the evolution of λ_R with azimuthal angle δ and the mass renormalization factors of the β and γ bands. Clearly, the kink strength shows a very similar momentum dependence as the renormalization of the γ band. In particular, it rapidly drops to zero at an azimuthal angle of $\delta \approx 30^\circ$, where the orbital mixing starts. This is consistent with the fact that no kink is observed in the β bands and strongly suggest that λ_R is highly orbital dependent.

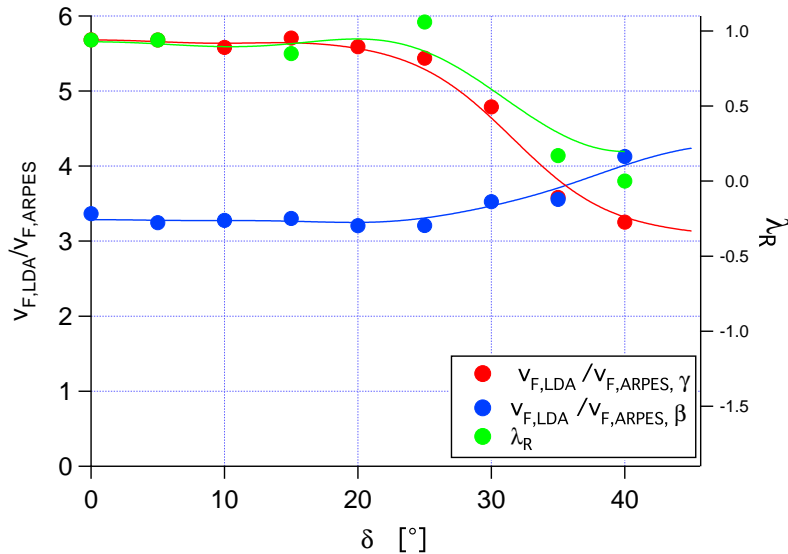


Figure 4.24: Momentum dependence of $Z = \frac{v_{LDA}}{v_{ARPES}}$ and λ_R . Blue and red markers: Z^{-1} for β and γ bands, respectively. The kink strength λ_R is shown in green. Lines are guides to the eye.

In the next two sections we will try to address possible mechanisms responsible for the kink. We start by modeling the data using electron-phonon interaction only, as proposed by Iwasawa *et al.* [78]

For the analysis we have chosen the band structure cut for $\delta = 15^\circ$, for which the γ band could be traced down to $E_B = 150$ meV. In figure 4.25 we compare the experimental dispersion with simulations assuming either Debye spectrum of phonons or multiple Einstein modes with different coupling constants. Excellent agreement with the experiment can be achieved using five boson modes located at ≈ 20 meV, ≈ 40 meV, ≈ 60 meV, ≈ 90 meV and ≈ 150 meV with coupling strengths $\lambda = 0.8, 0.8, 0.8, 1.0$ and 0.8 respectively. This, however, does not imply that the model is physically meaningful which appears questionable, given that electron-electron interaction was neglected in those fits. This will lead to an overestimation of the coupling constants. However, the mode frequencies should remain valid even after expanding the model to include electron-electron correlations. Though, a mode energy of 150 meV, which is significantly higher than all optical phonons, is not physical.

We next discuss to what extent electron-electron interaction can reproduce the highly structured self-energy shown in figure 4.25 (e). As showed in Chapter 2, for low frequencies the self-energy of a three-dimensional Fermi liquid is given by

$$\Sigma(\epsilon) = \alpha\epsilon + i\beta\epsilon^2 \quad (4.4)$$

i.e. the real part of the self energy is linear. The parameter α is in general is unknown due to many contributions to the mass renormalization factor that are not easy to separate. In the following we use $Z_{el-el} = 0.47$ found in a detailed ARPES study for the α band by Ingle *et al.*, which we further decrease to $Z_{el-el} = 0.3$ to account for the orbital anisotropy discussed in the previous section. In figure 4.26 (b) and (c) we show the spectral function calculated assuming electron-electron interaction only with $Z_{el-el} = 0.47$

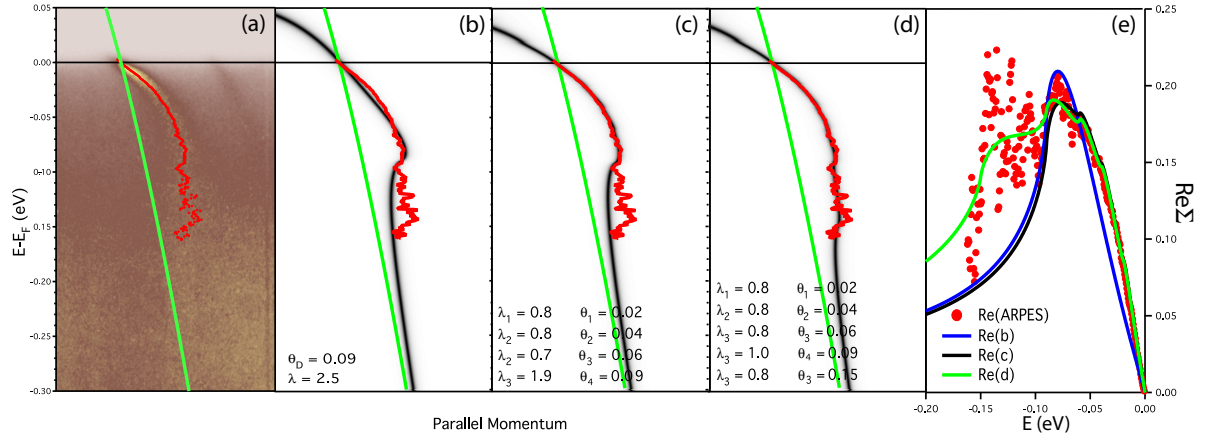


Figure 4.25: Modelling of the kink in the γ band by electron-phonon coupling. Red markers: fitted peak positions, green lines: single-electron dispersion, black line: simulated spectral function with $\Im m\Sigma = const.$ and different real parts for the electron-phonon self-energy. (b) Debye spectrum of phonons with $\theta_D = 40$ meV [80] and $\lambda = 2.5$. (c) and (d) simulations assuming several Einstein modes with frequency and coupling strength given in the figure. (e) comparison of the experimental and simulated real parts of the self-energy.

and $Z_{el-el} = 0.3$. Clearly, the simple Fermi liquid scenario can not account for the observed spectral function, as the model electron-electron self-energy quickly exceeds the experimental values.

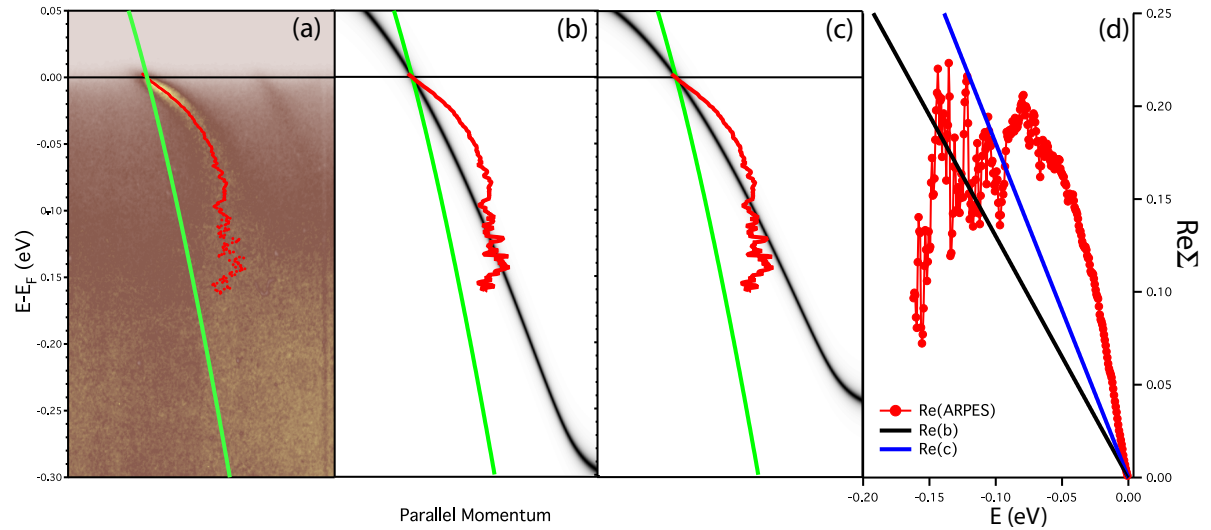


Figure 4.26: Modelling of the kink in the γ band by Fermi liquid scenario. Red markers: fitted peak positions, green lines: single-electron dispersion, black line: simulated spectral function with $\Im m\Sigma = const.$ and different real parts of the 3D Fermi liquid self-energy. (b) $Z_{el-el}^{-1} = 0.47$, (c) $Z_{el-el}^{-1} = 0.3$ and (d) comparison of the experimental and simulated real parts of the self-energy.

The most striking feature is that the observed $\Re\Sigma(\epsilon)$ rapidly decreases at energies above ~ 100 meV, while within the simple Fermi liquid scenario it should monotonically increase (see figure 4.26 (d)).

However, this type of behavior of the self-energy could be explained by a more realistic treatment of electron correlations incorporating the crossover from the coherent to the incoherent regime of the Fermi liquid, which we will further discuss in the following.

As described in Chapter 1, the Fermi liquid concept of quasiparticles holds only if the quasiparticle decay rate is much smaller than its energy. This means that for some $\epsilon > \epsilon^*$ quasiparticles become short lived and the Fermi liquid description is no longer valid.

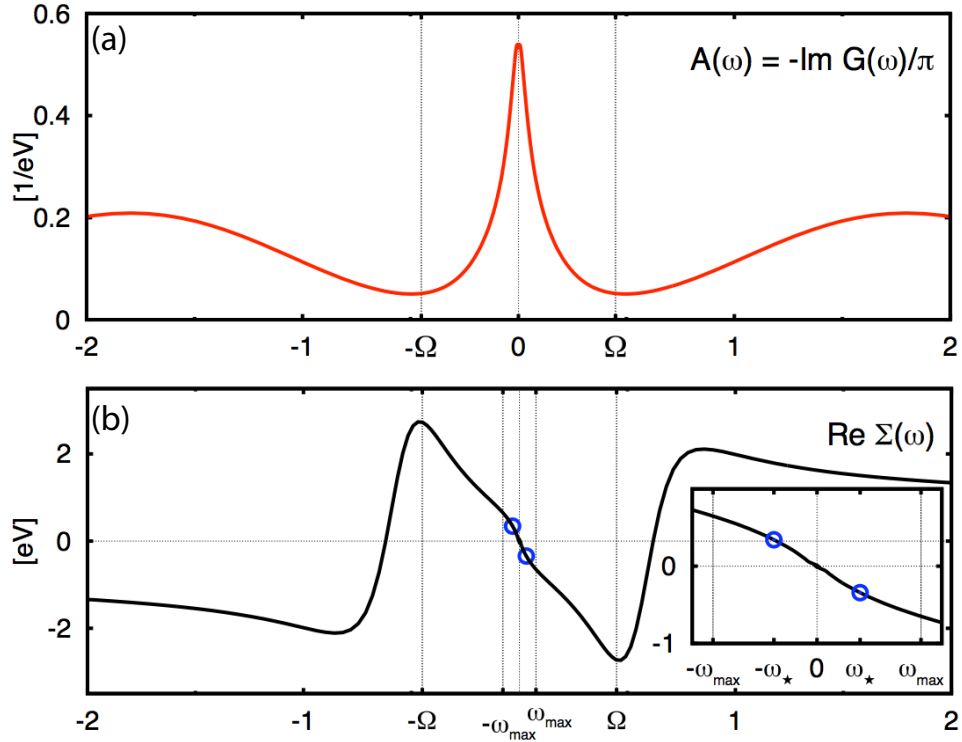


Figure 4.27: (a) Spectral function with three peak structure induced by correlations, (b) the real part of the self energy with kinks located at $\pm\omega_*$. Figure reproduced from [81].

Crossing from this so called incoherent regime to the coherent Fermi liquid coincides with a change of the slope of the real part of the self energy causing a kink in the band structure at $\epsilon = \epsilon^*$. Such electronic kinks are now understood to be a generic feature of DMFT calculations and were first reported for SrVO_2 by Byczuk *et al.* [81]. On figure 4.27 we reprint the spectral function and real part of the self energy from [81].

The strong correlations cause the spectral function to decompose into three peaks. The main peak at the Fermi level with the coherent part for $\epsilon < |\epsilon^*|$ and two incoherent peaks at higher binding energies that evolve into Hubbard bands for sufficiently large U . This three-peak structure of the spectral function has strong consequences for the shape of the self-energy. First, at $\epsilon = \epsilon^*$ the slope of $\Re\Sigma(\epsilon)$ changes, generating a kink in the band dispersion and then at $\epsilon = \pm\Omega$, at the dip in the spectral function, $\Re\Sigma(\epsilon)$ turns over and decreases until it saturates at some negative value.

In a recent DMFT study [77] Mravlje *et al.* suggested that the kink observed at 40 meV in the γ band of Sr_2RuO_4 could be caused by the crossover into the incoherent regime. To explore this idea we compare in figure 4.28 simulated spectral functions with ARPES data. Because authors of [77] do not show the full spectral function or self-energy we use the real part of the self-energy from Liebsch and Lichtenstein [60] as a starting point. Because the mass renormalization factor given by Liebsch and Lichtenstein is three times smaller than measured value we expect to see a large difference between the simulated and measured dispersion.

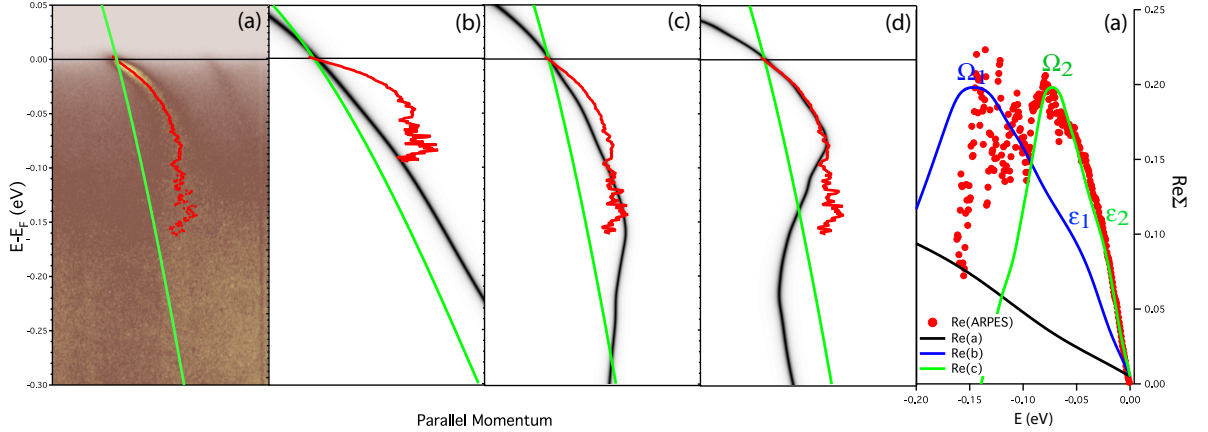


Figure 4.28: Modelling of the kink in the γ band by Fermi liquid cross-over scenario. Red markers: fitted peak positions, green lines: single-electron dispersion, black line: simulated spectral function with $\Im m\Sigma = const.$ and different real parts of the self-energy for the electron-electron interaction given by: (b) DMFT result from Liebsch and Lichtenstein (Σ_{LL}), (c) and (d) Σ_{LL} with an energy axis compressed by a factor of 4 and 8 respectively, (e) comparison of the experimental and simulated real parts of the self-energy.

In the DMFT self-energy published by Liebsch and Lichtenstein, ϵ^* and Ω are located at 200 meV and 600 meV, respectively. To improve the agreement with the experiment we have rescaled the energy axis of $\Re e\Sigma(\epsilon)$ to better reproduced the observed features. In our data we can identify two sets of ϵ^* and Ω that can be well reproduced by simple rescaling of the energy axis without changing the values of $\Re e\Sigma(\epsilon)$. For a scaling factor of 4 we get $\Omega_1 \approx 160$ meV and $\epsilon_1^* \approx 60$ meV and for a scaling factor of 8 $\Omega_2 \approx 90$ meV and $\epsilon_2^* \approx 35$ meV. Results are presented on figures 4.28 (c) and (d). Neither of the two can fully explain observed $\Re e\Sigma(\epsilon)$, comparison is displayed on figure 4.28 (d). From here we can conclude two possible scenarios to explain full spectral function of Sr_2RuO_4 measured by ARPES:

1. Femi liquid crossover. For $\Omega \approx 90$ meV and $\epsilon^* \approx 35$ meV we get almost perfect agreement with the experimental spectral function at low binding energies. However, the high binding energy part shows strong deviations because for $\epsilon > |\Omega|$ the slope of $\Re e\Sigma(\epsilon)$ is too steep. The agreement can thus be improved further by allowing for a more shallow decrease of the self-energy at high energy. Excellent agreement with the experiment can be achieved by rescaling the energy of Σ_{LL} by a factor of 8 for $\epsilon < |\Omega|$ and by a factor of 4 for $\epsilon > |\Omega|$ as shown by the green line in figure 4.29a (b). We stress, however, that this approach is purely empirical and should be tested against improved DMFT calculations.

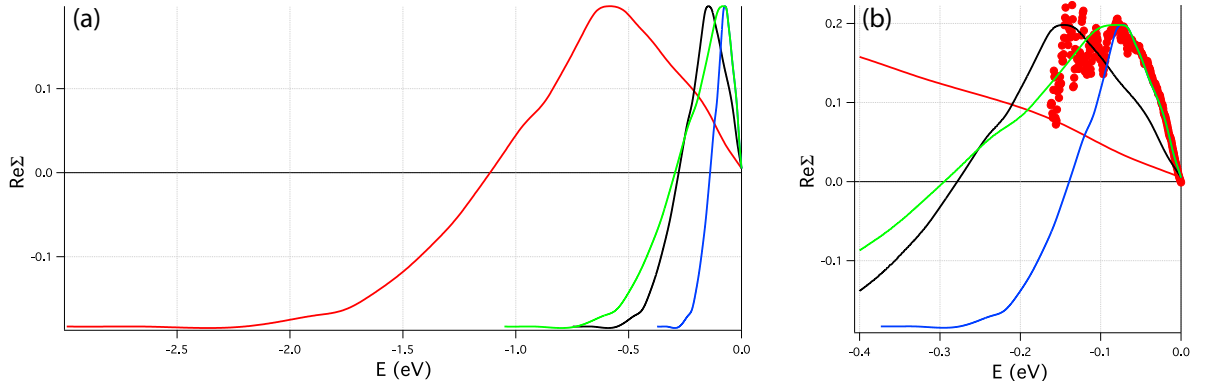


Figure 4.29: Comparison of the real part of the self energies for: original L-L (red line), L-L with energy axis scaled by a factor of 4 (black line), L-L with energy axis scaled by a factor of 8 (blue line). The green line represents modeled $\Re e\Sigma$ as described in the text, the red markers in panel (b) represent the experimental $\Re e\Sigma$.

2. Fermi liquid crossover with strong electron-phonon coupling.

For $\Omega \approx 160$ meV and $\epsilon^* \approx 60$ meV the simulated spectral function is in good agreement with the experimental spectral function at high binding energies. This suggests that the low energy kinks could arise from electron-phonon coupling. We therefore extend $\Re e\Sigma(\epsilon)$ from Liebsch and Lichtenstein by adding two Einstein modes at ≈ 40 meV and ≈ 80 meV. This gives excellent agreement with the experiment, as shown in figure 4.30 (b).

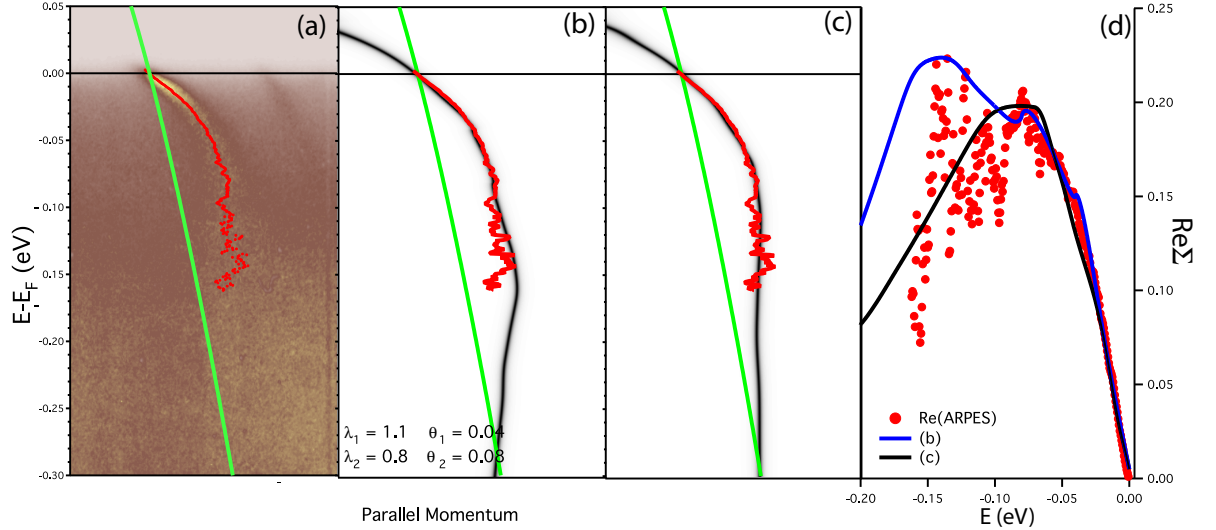


Figure 4.30: Momentum dependent kink in the γ band. Red markers: fitted peak positions, green lines: single-electron dispersion, black line (in panel (b) and (c)): simulated spectral function with $\Im m\Sigma = const.$ and the real part of the self-energy given by: (a) the electron-electron interaction from L-L scaled by a factor of 4 and two Einstein modes at energies $\hbar\omega_1 = 40$ meV $\hbar\omega_2 = 80$ meV, (b) purely electron-electron interaction scaled and adjusted from the original L-L dispersion.

Hence, two different, largely empirical, scenarios give a good agreement with the data. At the present stage we cannot comment on how realistic those models are. This will

require more detailed theoretical work. Particularly important is a numerical simulation of the correct shape of the self-energy for the electron-electron interaction. Despite some ambiguity, our results suggest that this part of the many-body correlations in Sr_2RuO_4 can not be simply regarded as a Fermi liquid and that for binding energies as low as $\approx 40 - 60$ meV excitations in Sr_2RuO_4 cross-over to the incoherent regime.

Summary

In this work we have studied the effects of spin-orbit coupling and many body-interactions on the band structure of Sr_2RuO_4 .

Using results of LSDA+SOC calculations we have constructed a tight binding model that includes the spin-orbit coupling and used it to study the effect of a magnetic field on the band structure of Sr_2RuO_4 . From the results we could conclude that the experimentally observed spin anisotropy can not be explained without strong many-particle correlations leading to a charge transfer between $d_{xz/yz}$ and d_{xy} orbitals.

Our ARPES study revealed a strong momentum dependence of the mass renormalization factors of the bulk β and γ bands, which has not been reported previously. We showed that this effect can be explained semi-quantitatively by the orbital anisotropy of the self-energy found in DMFT calculations and spin-orbit induced orbital mixing along the β and γ Fermi surface sheets. Furthermore, our data demonstrated that the large and momentum dependent renormalization of the γ sheet can be attributed to a kink in the dispersion around $E_B \approx 40$ meV.

To find the origin of the kink we have studied different many-body models. From the results we could conclude, that a simple Fermi liquid model cannot account for the observed self-energy. However, it might be explained by a more realistic treatment of electron-electron interactions including a cross-over to an incoherent regime for the binding energies as low as 40 – 60 meV.

Bibliography

- [1] J. H. de Boer and E. J. W. Verwey. Semi-conductors with partially and with completely filled $3d$ -lattice bands. *Proceedings of the Physical Society*, 49:59, 1937.
- [2] N. F. Mott. The basis of the electron theory of metals, with special reference to the transition metals. *Proceedings of the Physical Society*, 62:7, 1949.
- [3] H. J. Schulz. Fermi liquids and non-Fermi liquids. *arXiv:cond-mat/9503150v2*, 1995.
- [4] Andrew J Schofield. Non-Fermi liquids. *Contemporary Physics*, 40(2):95–115, March 1999.
- [5] S. A. Grigera, P. Gegenwart, R. A. Borzi, F. Weickert, A. J. Schofield, R. S. Perry, T. Tayama, T. Sakakibara, Y. Maeno, A. G. Green, and A. P. Mackenzie. Disorder-sensitive phase formation linked to metamagnetic quantum criticality. *Science*, 306(5699):1154–1157, 2004.
- [6] R. A. Borzi, S. A. Grigera, J. Farrell, R. S. Perry, S. J. S. Lister, S. L. Lee, D. A. Tennant, Y. Maeno, and A. P. Mackenzie. Formation of a nematic fluid at high fields in $\text{Sr}_3\text{Ru}_2\text{O}_7$. *Science*, 315(5809):214–217, 2007.
- [7] F. Lichtenberg, A. Catana, J Mannhart, and D. G. Schlom. Sr_2RuO_4 : A metallic substrate for the epitaxial growth of $\text{YBa}_2\text{Cu}_3\text{O}_7 - \delta$. *Applied Physics Letters*, 60:1138, 1992.
- [8] Y. Maeno. Electronic states of the superconductor Sr_2RuO_4 . *Physica C*, 282:206, 1997.
- [9] N. E. Hussey, A. P. MacKenzie, J. R. Cooper, Y. Maeno, S. Nishizaki, and T. Fujita. The normal state magnetoresistance of Sr_2RuO_4 . *Phys. Rev. B*, 57:5505, 1998.
- [10] A. P. Mackenzie, S. Ikeda, Y. Maeno, T. Fujita, S. R. Julian, and G. G. Lonzarich. The Fermi surface topography of Sr_2RuO_4 . *J. Phys. Soc. Jpn.*, 67:385, 1998.
- [11] Y. Maeno, H. Hashimoto, K. Yoshida, S. Nishizaki, T. Fujita, J. G. Bednorz, and F. Lichtenberg. Superconductivity in a layered perovskite without copper. *Nature (London)*, 372:532, 1994.
- [12] O. Chmaissem, J. D. Jorgensen, H. Shaked, S. Ikeda, and Y. Maeno. Thermal expansion and compressibility of Sr_2RuO_4 . *Phys. Rev. B*, 57:5067, 1998.
- [13] A. P. Mackenzie, R. K. W. Haselwimmer, A. W. Tyler, G. G. Lonzarich, Y. Mori, S. Nishizaki, and Y. Maeno. Extremely strong dependence of superconductivity on disorder in Sr_2RuO_4 . *Phys. Rev. Lett.*, 80(1):161–164, Jan 1998.
- [14] Tamio Oguchi. Electronic band structure of the superconductor Sr_2RuO_4 . *Phys. Rev. B*, 51(2):1385–1388, Jan 1995.

- [15] A. P. Mackenzie, S. R. Julian, A. J. Diver, G. J. McMullan, M. P. Ray, G. G. Lonzarich, Y. Maeno, S. Nishizaki, and T. Fujita. Quantum oscillations in the layered perovskite superconductor Sr_2RuO_4 . *Phys. Rev. Lett.*, 76:3786, 1996.
- [16] S. R.; Lonzarich G. G.; Maeno Y.; Mackenzie, A. P.; Julian and T. Fujita. Comment on "extended van Hove singularity in a noncuprate layered superconductor Sr_2RuO_4 ". *Phys. Rev. Lett.*, 78:2271, 1997.
- [17] A. Damascelli, D. H. Lu, K. M. Shen, N. P. Armitage, F. Ronning, D. L. Feng, C. Kim, Z.-X. Shen, T. Kimura, Y. Tokura, Z. Q. Mao, and Y. Maeno. Fermi surface, surface states, and surface reconstruction in Sr_2RuO_4 . *Phys. Rev. Lett.*, 85(24):5194–5197, Dec 2000.
- [18] D. H. Lu, M. Schmidt, T. R. Cummins, S. Schuppler, F. Lichtenberg, and J. G. Bednorz. Fermi surface and extended van Hove singularity in the noncuprate superconductor Sr_2RuO_4 . *Phys. Rev. Lett.*, 76(25):4845–4848, Jun 1996.
- [19] T. Yokoya, A. Chainani, T. Takahashi, H. Katayama-Yoshida, M. Kasai, and Y. Tokura. Angle-resolved and resonant photoemission study of Sr_2RuO_4 . *Journal of Physics and Chemistry of Solids*, 56(12):1885 – 1886, 1995. Proceedings of the Conference on Spectroscopies in Novel Superconductors.
- [20] A. P. Mackenzie and Y. Maeno. The superconductivity of Sr_2RuO_4 and the physics of spin-triplet pairing. *Rev. of Mod. Phys.*, 75:658, 2003.
- [21] R. Matzdorf, Z. Fang, Ismail, Jiandi Zhang, T. Kimura, Y. Tokura, K. Terakura, and E. W. Plummer. Ferromagnetism stabilized by lattice distortion at the surface of the p -wave superconductor Sr_2RuO_4 . *Science*, 289:746, 2000.
- [22] R. Matzdorf, Ismail, T. Kimura, Y. Tokura, and E. W. Plummer. Surface structural analysis of the layered perovskite Sr_2RuO_4 by LEED $I(V)$. *Physical Review B*, 65:085404, 2002.
- [23] H. Hertz. über einen Einfluss des ultravioletten Lichtes auf die elektrische Entladung. *Annalen der Physik und Chemie*, 267(8):983–1000, 1887.
- [24] W. Hallwachs. über den Einfluss des Lichtes auf electrostatisch geladene Körper. *Wiedemann'sche Annalen*, 33:301–312, 1888.
- [25] J.J. Thomson. On the charge of electricity carried by the ions produced by Röntgen rays. *Phil. Mag.*, 46:528, 1898.
- [26] P. Lenard. über die lichtelektrische Wirkung. *Ann. Phys.*, 8:147, 1902.
- [27] A. Einstein. über einen die Erzeugung und Verwandlung des Lichtes betreffenden heuristischen Gesichtspunkt. *Ann. Phys.*, 17:132, 1905.
- [28] R.A. Millikan. A direct photoelectric determination of Planck's h . *Phys. Rev.*, 7:355, 1916.
- [29] H.P. Bonzel and Ch. Kleint. On the history of photoemission. *Progress in Surface Science*, 49:107–153, 1996.
- [30] G. Beck. Zur Theorie des Photoeffekts. *Z. Phys.*, 41:443, 1927.
- [31] G. Wentzel. über die Richtungsverteilung der Photoelektronen. *Z. Phys.*, 41:828, 1927.

- [32] J. R. Oppenheimer. Zur Quantentheorie kontinuierlicher Spektren. *Z. Phys.*, 41:268, 1927.
- [33] P. D. Innes. On the velocity of the cathode particles emitted by various metals under the influence of röntgen rays, and its bearing on the theory of atomic disintegration. *Proc. Royal Soc.*, 79:442, 1907.
- [34] M. de Broglie. La physique des rayons X. *J. Phys et Rad.*, 2:265, 1921.
- [35] K. Siegbahn. Conf. of the Swedish nat. committee for physics, Stockholm. *Ark. Fys.*, 7:86, 1954.
- [36] C. Nordling, E. Sokolowski, and K. K. Siegbahn. Precision method for obtaining absolute values of atomic binding energies. *Phys. Rev.*, 105:1676, 1957.
- [37] K. Siegbahn, C. Nordling, A. Fahnnann, R. Nordberg, K. Hamrin, J. Hedman, G. Johansson, T. Bergmark, S.E. Karlsson, I. Lindgren, and B. Lindberg. *Atomic, Molecular and Solid State Structure Studied by Means of Electron Spectroscopy*. Almqvist and Wiksells, 1967.
- [38] K. Siegbahn, C. Nordling, G. Johansson, J. Hedman, P.F. Heden, K. Hamrin, N. Gelius, T. Bergmark, L.O. Werme, R. Manne, and Y. Baer. *ESCA Applied to Free-Molecules*. North-Holland, 1969.
- [39] M. I. Al-Joboury, D. P. May, and D.W. Turner. Molecular photoelectron spectroscopy. part iii. the ionization potentials of oxygen, carbon monoxide, nitric oxide, and acetylene. *J. Chem. Soc.*, 616:4434, 1965.
- [40] D.W. Turner, C. Bakek, D. M. A.D. Baker, and C.R. Brundle. *Molecular Photoelectron-Spectroscopy*. Wiley Interscience, 1970.
- [41] D.W. Turner and M.I. Al-Joboury. Determination of ionization potentials by photoelectron energy measurements. *J. Chem. Phys.*, 37:3007, 1962.
- [42] http://en.wikipedia.org/wiki/photoemission_spectroscopy.
- [43] S. Huefner. *Very High Resolution Photoemission Spectroscopy*. Springer, 2007.
- [44] Andrea Damascelli. Probing the electronic structure of complex systems by ARPES. *Physica Scripta*, 2004(T109):61, 2004.
- [45] C. N. Berglund and W. E. Spicer. Photoemission studies of copper and silver: Theory. *Phys. Rev.*, 136:A1030, 1964.
- [46] S. Huefner. *Photoemission Spectroscopy, Principles and Applications*. Springer, 2003.
- [47] W. L. McMillan and J.M. Rowell. Lead phonon spectrum calculated from superconducting density of states. *Phys. Rev. Lett.*, 14:108–112, 1965.
- [48] <http://www.specs-scientific.net/products/xps/energy-analyzer.htm>.
- [49] A. M. Oles K. A. Chao and J. Spalek. Canonical perturbation expansion of the Hubbard mode. *Phys. Rev. B*, 18:3453, 1978.

- [50] David Bohm and David Pines. A collective description of electron interactions: III. Coulomb interactions in a degenerate electron gas. *Phys. Rev.*, 92(3):609–625, Nov 1953.
- [51] Neil W. Ashcroft and N. David Mermin. *Solid State Physics*. Brooks Cole, 1 edition, January 1976.
- [52] W. Kohn and L. J. Sham. Self-consistent equations including exchange and correlation effects. *Phys. Rev.*, 140(4A):A1133–A1138, Nov 1965.
- [53] P. Blaha, K. Schwarz, G. K. H. Madsen, D. Kvasnicka, and J. Luitz. *WIEN2K, An Augmented Plane Wave + Local Orbitals Program for Calculating Crystal Properties*. Karlheinz Schwarz, Techn. Universitat Wien, Austria, 2001.
- [54] M. Itoh. Structure of two-dimensional conductor of Sr_2RuO_4 . *J. of Solid State Chemistry*, 118:206, 1995.
- [55] M. W. Haverkort, I. S. Elfimov, L. H. Tjeng, G. A. Sawatzky, and A. Damascelli. Strong spin-orbit coupling effects on the Fermi surface of Sr_2RuO_4 and Sr_2RhO_4 . *Phys. Rev. Lett.*, 101(2):026406, Jul 2008.
- [56] A H MacDonald, W E Pickett, and D D Koelling. A linearised relativistic augmented-plane-wave method utilising approximate pure spin basis functions. *Journal of Physics C: Solid State Physics*, 13(14):2675, 1980.
- [57] P. Novak. Lecture notes on spin-orbit coupling. to be published.
- [58] S. R.; Forsythe D.; Ohmichi E.; Mackenzie, A. P.; Julian. Quasi-two-dimensional Fermi liquid properties of the unconventional superconductor Sr_2RuO_4 . *Advances in Physics*, 52(7):639–725, 2003.
- [59] Emil J Rozbicki, James F Annett, Jean-Rene Souquet, and Andrew P Mackenzie. Spin-orbit coupling and k -dependent Zeeman splitting in strontium ruthenate. *Journal of Physics: Condensed Matter*, 23(9):094201, 2011.
- [60] A. Liebsch and A. Lichtenstein. Photoemission quasiparticle spectra of Sr_2RuO_4 . *Phys. Rev. Lett.*, 84(7):1591–1594, Feb 2000.
- [61] M. Schmidt, T. R. Cummins, M. Bürk, D. H. Lu, N. Nücker, S. Schuppler, and F. Lichtenberg. Nature of the electronic states in the layered perovskite noncuprate superconductor Sr_2RuO_4 . *Phys. Rev. B*, 53(22):R14761–R14764, Jun 1996.
- [62] T. Takahashi, T. Yokoya, A. Chainani, H. Ding, J. C. Campuzano, M. Kasai, and Y. Tokura. Angle-resolved photoemission study of Sr_2RuO_4 ; an extended van-Hove singularity in noncuprate superconductors. *Physica C: Superconductivity*, 282-287(Part 1):218 – 221, 1997. Materials and Mechanisms of Superconductivity High Temperature Superconductors V.
- [63] A. V. Puchkov, Z.-X. Shen, T. Kimura, and Y. Tokura. ARPES results on Sr_2RuO_4 : Fermi surface revisited. *Phys. Rev. B*, 58(20):R13322–R13325, Nov 1998.
- [64] K. M. Shen, A. Damascelli, D. H. Lu, N. P. Armitage, F. Ronning, D. L. Feng, C. Kim, Z.-X. Shen, D. J. Singh, I. I. Mazin, S. Nakatsuji, Z. Q. Mao, Y. Maeno, T. Kimura, and Y. Tokura. Surface electronic structure of Sr_2RuO_4 . *Phys. Rev. B*, 64(18):180502, Oct 2001.

- [65] Y. Aiura, Y. Yoshida, I. Hase, S. I. Ikeda, M. Higashiguchi, X. Y. Cui, K. Shimada, H. Namatame, M. Taniguchi, and H. Bando. Kink in the dispersion of layered Strontium Ruthenates. *Phys. Rev. Lett.*, 93(11):117005, Sep 2004.
- [66] S.-C. Wang, H.-B. Yang, A. K. P. Sekharan, H. Ding, J. R. Engelbrecht, X. Dai, Z. Wang, A. Kaminski, T. Valla, T. Kidd, A. V. Fedorov, and P. D. Johnson. Quasiparticle line shape of Sr_2RuO_4 and its relation to anisotropic transport. *Phys. Rev. Lett.*, 92(13):137002, Apr 2004.
- [67] N. J. C. Ingle, K. M. Shen, F. Baumberger, W. Meevasana, D. H. Lu, Z.-X. Shen, A. Damascelli, S. Nakatsuji, Z. Q. Mao, Y. Maeno, T. Kimura, and Y. Tokura. Quantitative analysis of Sr_2RuO_4 angle-resolved photoemission spectra: Many-body interactions in a model Fermi liquid. *Phys. Rev. B*, 72(20):205114, Nov 2005.
- [68] H. Iwasawa, Y. Aiura, T. Saitoh, I. Hase, S. I. Ikeda, Y. Yoshida, H. Bando, M. Higashiguchi, Y. Miura, X. Y. Cui, K. Shimada, H. Namatame, and M. Taniguchi. Orbital selectivity of the kink in the dispersion of Sr_2RuO_4 . *Phys. Rev. B*, 72(10):104514, Sep 2005.
- [69] T. E. Kidd, T. Valla, A. V. Fedorov, P. D. Johnson, R. J. Cava, and M. K. Haas. Orbital dependence of the Fermi liquid state in Sr_2RuO_4 . *Phys. Rev. Lett.*, 94(10):107003, Mar 2005.
- [70] B. J. Kim, Jaejun Yu, H. Koh, I. Nagai, S. I. Ikeda, S.-J. Oh, and C. Kim. Missing xy -band fermi surface in $4d$ transition-metal oxide Sr_2RhO_4 : Effect of the octahedra rotation on the electronic structure. *Phys. Rev. Lett.*, 97(10):106401, Sep 2006.
- [71] R. Matzdorf, Ismail, T. Kimura, Y. Tokura, and E. W. Plummer. Surface structural analysis of the layered perovskite Sr_2RuO_4 by LEED $I(V)$. *Phys. Rev. B*, 65(8):085404, Jan 2002.
- [72] A. Tamai, M. P. Allan, J. F. Mercure, W. Meevasana, R. Dunkel, D. H. Lu, R. S. Perry, A. P. Mackenzie, D. J. Singh, Z.-X. Shen, and F. Baumberger. Fermi surface and van Hove singularities in the itinerant metamagnet $\text{Sr}_3\text{Ru}_2\text{O}_7$. *Phys. Rev. Lett.*, 101(2):026407, Jul 2008.
- [73] Mackenzie A. P.; Julian S. R.; Forsythe D.; Ohmichi E.; Bergemann C. Quasi-two-dimensional Fermi liquid properties of the unconventional superconductor Sr_2RuO_4 . *Advances in Physics*, 52:7, 2003.
- [74] K. M. Shen, N. Kikugawa, C. Bergemann, L. Balicas, F. Baumberger, W. Meevasana, N. J. C. Ingle, Y. Maeno, Z.-X. Shen, and A. P. Mackenzie. Evolution of the Fermi surface and quasiparticle renormalization through a van Hove singularity in $\text{Sr}_{2-y}\text{La}_y\text{RuO}_4$. *Phys. Rev. Lett.*, 99(18):187001, Oct 2007.
- [75] I. Eremin, D. Manske, and K. H. Bennemann. Electronic theory for the normal-state spin dynamics in Sr_2RuO_4 : Anisotropy due to spin-orbit coupling. *Phys. Rev. B*, 65(22):220502, May 2002.
- [76] R. M. Konik and T. M. Rice. Orbital dependence of quasiparticle lifetimes in Sr_2RuO_4 . *Phys. Rev. B*, 76(10):104501, Sep 2007.
- [77] Jernej Mravlje, Markus Aichhorn, Takashi Miyake, Kristjan Haule, Gabriel Kotliar, and Antoine Georges. Coherence-incoherence crossover and the mass-renormalization puzzles in Sr_2RuO_4 . *Phys. Rev. Lett.*, 106(9):096401, Mar 2011.

- [78] H. Iwasawa, Y. Yoshida, I. Hase, S. Koikegami, H. Hayashi, J. Jiang, K. Shimada, H. Namatame, M. Taniguchi, and Y. Aiura. Interplay among Coulomb interaction, spin-orbit interaction, and multiple electron-boson interactions in Sr_2RuO_4 . *Phys. Rev. Lett.*, 105(22):226406, Nov 2010.
- [79] E. Gorelov and E. Pavarini. Unpublished.
- [80] Johnpierre Paglione, C. Lupien, W. A. MacFarlane, J. M. Perz, Louis Taillefer, Z. Q. Mao, and Y. Maeno. Elastic tensor of Sr_2RuO_4 . *Phys. Rev. B*, 65(22):220506, May 2002.
- [81] K. Held Y.-F. Yang I. A. Nekrasov Th. Pruschke & D. Vollhardt K. Byczuk, M. Kollar. Kinks in the dispersion of strongly correlated electrons. *Nature Physics*, 3:168–171, 2007.